Study on Enhancements of Signal Profile Fitting Algorithms of CT-TDLAS for Temperature and Concentration Fields Measurements

September 2016

Graduate School of Advanced Technology and Science,

Tokushima University

Doowon Choi

Abstract

CT (Computed Tomographic) – TDLAS (Tunable Diode Laser Absorption Spectroscopy) is a non-intrusive diagnostic technique that allows for spatially resolved measurements of temperature and species concentration combustion fields such as burner, engine, gas turbine and furnace and so on. Also, the temperature and concentration distributions on the cross-section of a combustion flame enable to analyze elaborately on the combustion phenomena. A purpose of this thesis is to optimize a reconstruction of temperature and H_2O number density distributions.

First, MART (Multiplicative Algebraic Reconstruction Technique) algorithm was chosen as data reconstruction calculation and the result was compared with that by using ART (Algebraic Reconstruction Technique) method.

Second, MLOS (Multiple Mine of Sight) method was proposed to decide an initial value of algorithm.

Third, three new signal fitting algorithms, Two-Ratios of Three-Wavelength Fitting algorithm, Full-Profile Cross-Correlation algorithm and 6-Line-Profiles Fitting algorithm, were suggested as a reconstruction of temperature and H_2O number density. These algorithms were theoretically investigated by using virtual data and experimentally demonstrated by utilizing the obtained data in burner and engine experiments in case of necessity.

Consequently, the performance of 6-Line-Profiles Fitting algorithm was best of all. Therefore, this method enables to apply the real-time 2D temperature and species concentration measurement in various combustion fields.

Table of Contents

1. Introduction

1.1 Necessity of 2D temperature and concentration measurements

According to the MARPOL (International Marine Pollution) regulation, all existing ships should carry the SEEMP (Ship Energy Efficiency and Management Plan) certification due to heavy air pollution by ships. This is due to the fact that the air pollution influence by ships is more serious than by automobile vehicles. Harmful gases from ships are NOx, SOx and CO2.

Fig. 1.1 Importance of concentration measurements for harmful gases

To control and monitor the harmful gases from the ships, it is necessary to measure the amount of gases emitted from ships. To predict the amount of those gases from ships, it is necessary to measure the concentration field across the funnel of the ships. The conventional measurement techniques, such as the SAW (Surface Acoustic Wave) type by Lim et al [1], the semiconductor type by Fine et al [2], thermal conductivity type by Chen [3] and the electrochemical type by Dossi et al [4], are mainly based on the pointwise measurement. Especially, these approaches couldn't be used to measure concentrations of the wide area.

In order to predict the amount of exhausted gas from a ship funnel, there have been several attempts to improve the concentration measurements. Yuki and Murata [5] used a tunable diode laser for gas analyses. They adopted a laser spectroscopy to measure gas concentration in real

time to control the combustion inside of furnace. Besides, TDLAS and computed tomography method have been developed at variable fields [6-33].

Deguchi et al [6] have developed a new CT-TDLAS (Computed Tomography-Tunable Diode Laser Absorption Spectroscopy) which can measure 2-dimensional temperature and concentration fields simultaneously for gas flows. This measurement technique is regarded as one of the strong candidates that can carry out the concentration measurements.

To attain better measurements by using CT-TDLAS techniques, it is necessary to enhance the performances of data reconstruction algorithms, such as ART (Algebraic Reconstruction Technique) [6] and Simplex algorithm [7]. Further, a curve fitting of the spectral absorbance should be matched more exactly to enhance measurement performances of CT-TDLAS. The conventional curve fitting methods have been based on the ratio of two-peaks at two wave lengths [6].

In this thesis, it was suggested two major approaches for the enhancements of CT-TDLAS.

1) MART (Multiplicative Algebraic Reconstruction Technique) method was chosen as an iterative reconstruction algorithm for CT-TDLAS.
2) Three types of curve fitting algorithms were newly proposed for CT-TDLAS.

1.2 Objectives of the study

A thermocouple has been widely used for the temperature measurement, however it is a point measurement device and does not have a quick response. But TDLAS has the characteristics of fast response, high sensitivity and non-intrusive measurement method of gas concentrations as well as temperature and it enables the real-time monitoring of these factors for optimization of the combustion efficiency. We need to develop the optimized CT-TDLAS system in order to investigate 2 D temperature and concentration distributions of engine exhaust gas.

This paper focuses on a measurement development of 2 dimensional temperature and concentration based on CT-TDLAS using absorption spectra of water vapor at 1388 nm ~ 1388.6 nm

The first purpose of this study is to report an optimized MART algorithm concerning the reconstruction calculation and a performance evaluation comparing with the conventional reconstruction algorithms. The second purpose is to introduce three new algorithms for a curve fitting of absorption spectra and to investigate their performances comparing with the conventional fitting algorithms.

2. Theory

2.1 Beer-Lambert law

A fundamental equation for a tunable diode absorption spectroscopy is the Beer-Lambert law, which is the relationship between absorbance and concentration of an absorbing species as shown Fig. 2.1. The intensity ratio of incident light and transmitted light depends on the mole fraction. TDLAS is based on Lambert Beer's law and is used by this basic law to measure temperature and species concentration. The number density of the measured species *n* is related to the amount of light absorbed as following formula [33].

$$I_\lambda / I_{\lambda 0} = \exp\{-A_\lambda\}$$

$$= \exp\left\{-\sum_i (n_i L \alpha_i)\right\}$$

$$= \exp\left\{-\sum_i \left(n_i L \sum_j S_{i,j}(T) G_{V i,j} \right)\right\} \qquad (2.1)$$

Here I_λ and $I_{\lambda 0}$ describe the transmitted and incident laser intensities and A_λ is the spectral absorbance. n_i is the number density of species i, L is the optical path length, α_i is absorption coefficient, $S_{i,j}$ is the temperature dependent absorption line strength at the absorption line j, and $G_{vi,j}$ the line broadening function. The Eq. (2.1) shows the absorbance is proportional to number density, path length and absorption coefficient and the transition line strength. $S_{i,j}(T)$, which is a function of temperature, is related to gas species, transition wavelength and gas temperature. $G_{vi,j}$, the line broadening function, is usually approximated using a Voigt profile. Afterwards, this paper will describe about a broadening function in detail.

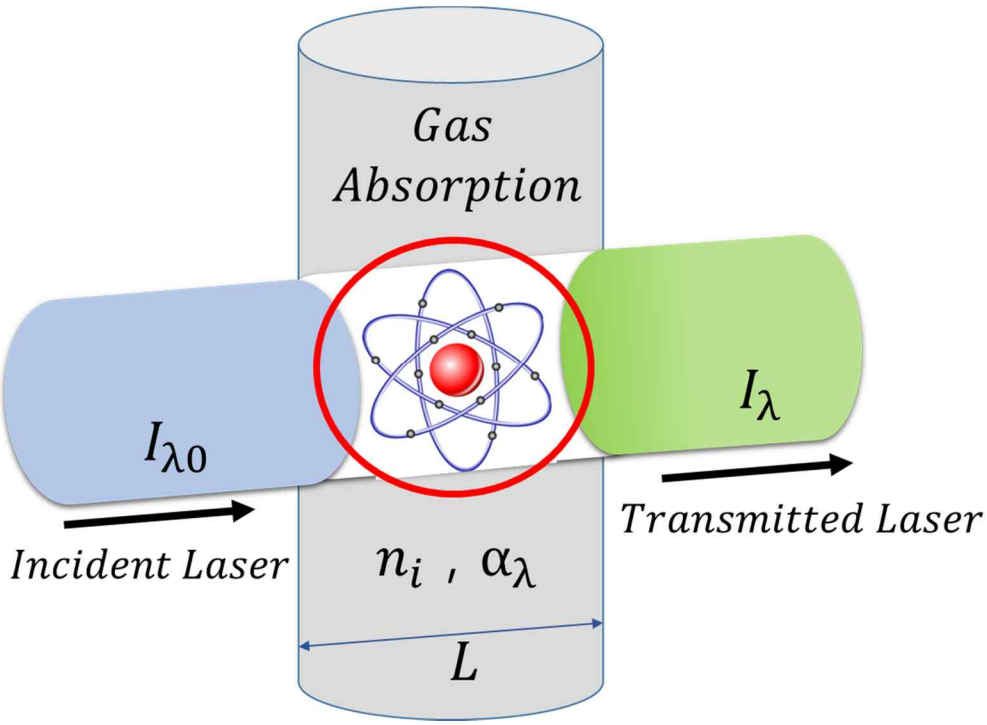

Fig. 2.1 Schematic diagram of Beer-Lambert law

2.2 Absorption Spectroscopy

$S_{i,j}(T)$ is governed as a function of temperature because it depends on Boltzmann distribution when molecules absorb energy. Also, it has been provided from HITRAN (High Resolution Transmission) database [34] at the Harvard-Smithsonian Center for Astrophysics, Cambridge MA, USA. The absorption line strength as a function of temperature for a species *i* can be calculated by the following equation [33].

$$S_{i,j}(\mathrm{T}) \approx S_{i,j}(T_0)\frac{Q(T_0)}{Q(T)}\,exp\,\left[-\frac{hcE_i^{"}}{k}\left(\frac{1}{T}-\frac{1}{T_o}\right)\right]\left[\frac{1-\exp\left(\frac{hcv_{0,i}}{kT}\right)}{1-\exp\left(\frac{hcv_{0,i}}{kT_0}\right)}\right] \qquad (2.2)$$

Here, h [J·s] is Planck's constant, k [J/K] is Boltzmann's constant, c [cm/s] is the light speed, v_0 [cm^{-1}] is wavenumber at the line-center, $E_i^{"}$ [cm^{-1}] the lower-state energy of the transition, T_0 [K] the reference temperature (296 K) and $Q(T)$ the partition function of absorbing molecular at a particular temperature. $Q(T)$ usually express as a third-order polynomial function in temperature and requires the storage of four coefficients at a given temperature range [35].

Fig. 2.2 shows an example of the H_2O absorption spectra calculated using the HITRAN database at the temperature range 300 K~1200 K and pressure 0.1~2.0 MPa.

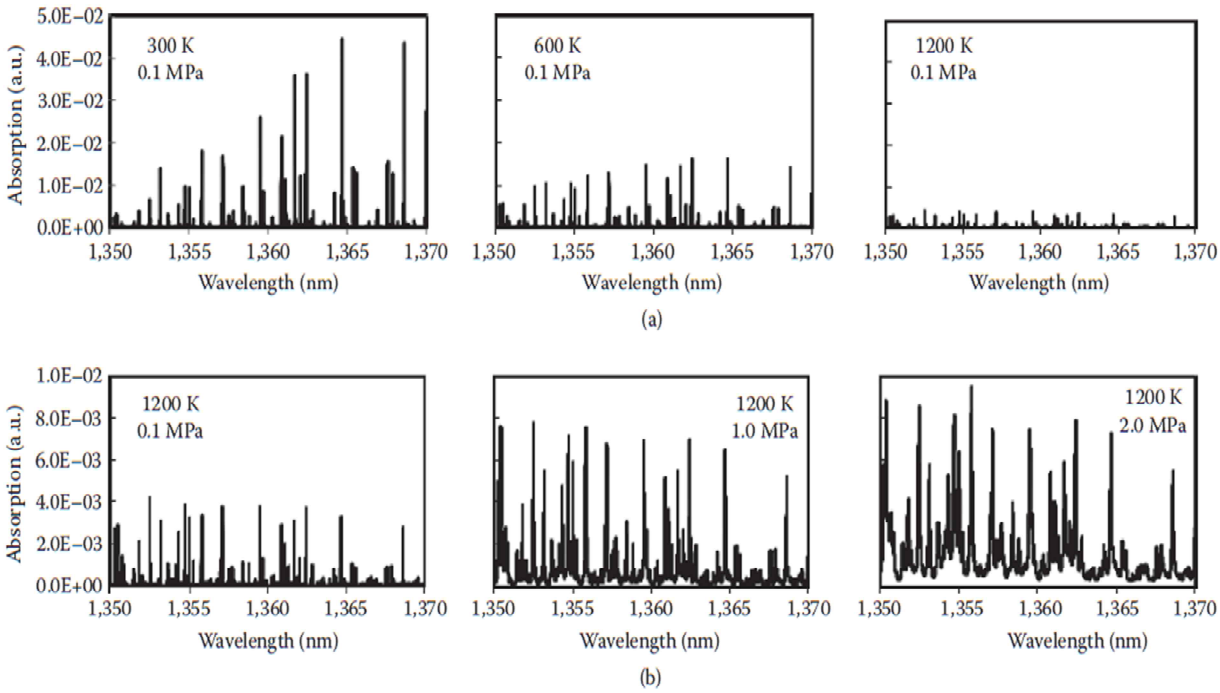

Fig. 2.2 Absorption spectra H_2O in the wavelength of 1350 ~1370 nm

([33] Deguchi. Y., Industrial applications of Laser Diagnostics, New York, CRS Press: Taylor & Francis 2011, pp.171.)

2.3 Broadening function

The radiation propagating through a gas is transformed by the absorption and emission processes. Although emission and absorption lines have different intensity distributions they may occur at the same wavelength. Also, this radiation has different characteristic affected according to atomic configuration or a certain molecular.

Broadening effect is determined by the physical mechanisms that perturb the energy levels of the transition or the absorbing molecules interact with beam. One of these broadening effects is Doppler broadening. It occurs random thermal motion of absorbing molecules, creating spread of Doppler shifts in the direction of the observer. The line profile of this spread is given by the Gaussian line profile.

$$G_D(v) = \frac{2}{\Delta v_D}\sqrt{\frac{\ln 2}{\pi}}\, exp\left[-4\ln 2\left(\frac{v-v_0}{\Delta v_D}\right)^2\right] \tag{2.3}$$

$$\Delta v_D = v_0\sqrt{\frac{8kT\ln 2}{mc^2}} \approx 7.1623\times 10^{-7} v_0\sqrt{\frac{T}{M}} \tag{2.4}$$

Here, Δv_D [cm^{-1}] is Doppler full-width at half maximum (FWHM), v_0 [cm^{-1}] is line center frequency and M [g/mol] is the molecular weight of the absorbing species. As gas temperature increase, so do FWHM increase from Eq. 2.4.

The other type broadening is pressure broadening, also referred to as collision broadening. This kinds of broadening is caused by the perturbation of the energy level owing to molecular collisions. Pressure broadening takes to a Lorentzian line profile.

$$G_C(v) = \frac{\Delta v_C}{2\pi}\frac{1}{(v-v_0)^2+\left(\frac{\Delta v_C}{2}\right)^2} \tag{2.5}$$

Where Δv_C [cm^{-1}] is the collisional FWHM. Also, it is proportional to the system pressure.

$$\Delta v_C = P \sum_j X_j \, 2\gamma_j \tag{2.6}$$

Where X_j is a mole fraction of j species gas, γ_j [cm^{-1}atm^{-1}] is collisional broadening coefficient due to the collisions between the absorbing and perturbing molecules j (foreign-gas broadening), or between the absorbing molecules themselves (self-broadening). Also, it is expressed a temperature function at reference temperature as shown following equation.

$$\gamma_j(T) = \gamma_j(T_0)\left(\frac{T_0}{T}\right)^{n_j} \tag{2.7}$$

Here, n_j is coefficient of temperature dependence, T_0 is reference temperature.

Because these broadening effects occur simultaneously, the overall broadening will be convolution of the Gaussian and the Lorentzian broadening profiles, creating called the Voigt profile. The Voigt profile is expressed as following.

$$G_D(a,x) = \int_{-\infty}^{+\infty} G_D(u) G_C(V-u)du = G_D(v_0)\frac{a}{\pi}\int_{-\infty}^{+\infty}\frac{\exp(-y^2)}{a^2+(x-y)^2}dy \tag{2.8}$$

$$a = \sqrt{\ln 2}\frac{\Delta v_C}{\Delta v_D} \tag{2.9}$$

$$x = \sqrt{\ln 2}\frac{v-v_0}{\Delta v_D} \tag{2.10}$$

$$\Delta v_V = \frac{\Delta v_C}{2} + \sqrt{\left(\frac{{\Delta v_C}^2}{4} + {\Delta v_D}^2\right)} \tag{2.11}$$

The variable *a* and *x* are relative to an influence of broadening effect. If collision broadening is increased, variable *a* also would be increased.

Peak height of the Voigt profile is given by Eq. 2.12~2.14.

$$G_V(v_0) = \left[\left(\frac{\beta}{\gamma_{ED}\sqrt{\pi}}\right) + \left(\frac{1-\beta}{\pi \cdot \gamma_C}\right)\right] \tag{2.12}$$

$$\beta = \left(\frac{\gamma_{ED}}{\gamma_C + \gamma_{ED}}\right) \tag{2.13}$$

$$\gamma_{ED} = \frac{\gamma_D}{\sqrt{\ln 2}} \tag{2.14}$$

Here, γ_C and γ_D are HWHM (Half-Width at Half Maximum line widths) of Gaussian and Lorentzian profiles. Therefore, the absorption spectra are needed quantitatively to recalculate by broadening function.

Fig. 2.3 shows the comparison of three line broadenings. In this study, Voigt profile was used considering both Doppler and collision broadening. Afterward, their broadening factors are mentioned in detail.

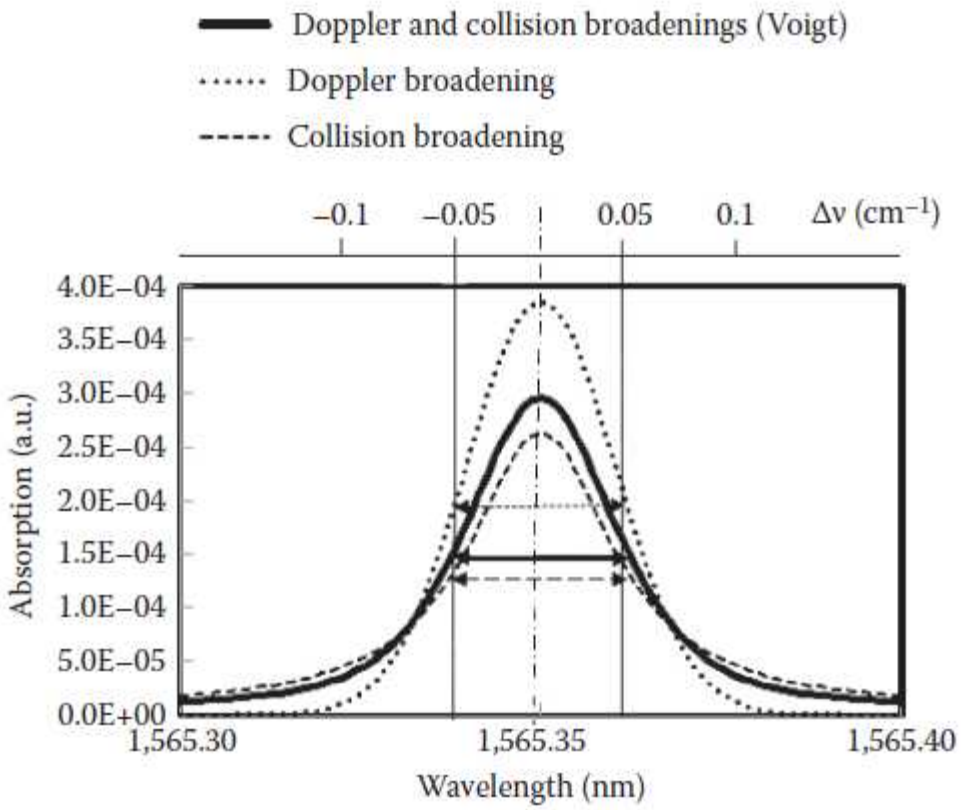

Fig. 2.3 Comparison of three line broadenings

([33] Deguchi. Y., Industrial applications of Laser Diagnostics, New York, CRS Press: Taylor & Francis 2011, pp.169.)

2.4 Diode Laser Absorption Spectroscopy

2.4.1 Tunable Laser Absorption Spectroscopy

Fig. 2.4 (a) shows the energy transfer process of TDLAS. If the electron moves up from lower state to upper state, energy is absorbed. Absorption of photons as a result of energy level change of electrons. The energy of a photon, lost or gained, is calculated using Planck's equation as following equation.

$$Energy\ \ Difference \quad (\Delta E) = hv \tag{2.15}$$

Here, h [6.62607×10^{-34} J s / cycles] is Planck's constant, and v stands for frequency in cycles/s.

Fig. 2.4 (b) shows the typical arrangement of TDLAS system. As shown in the picture, the system of TDLAS is simple in comparison with Laser-induced Florescence, Laser-Induced Breakdown Spectroscopy, Spontaneous Raman Spectroscopy and so on.

The feature of TDLAS technique is high sensitivity % ~ ppm (ppb), fast response (kHz) and non-intrusive assessment of gas concentrations. Because the atoms and molecules have their own spectral pattern, an analysis of spectra using TDLAS has excellent selectivity and sensitivity. Therefore, the high sensitivity and fast response of TDLAS enable the real-time monitoring of gas such as O_2, CO, CO_2, H_2O, NH_3, and NO.

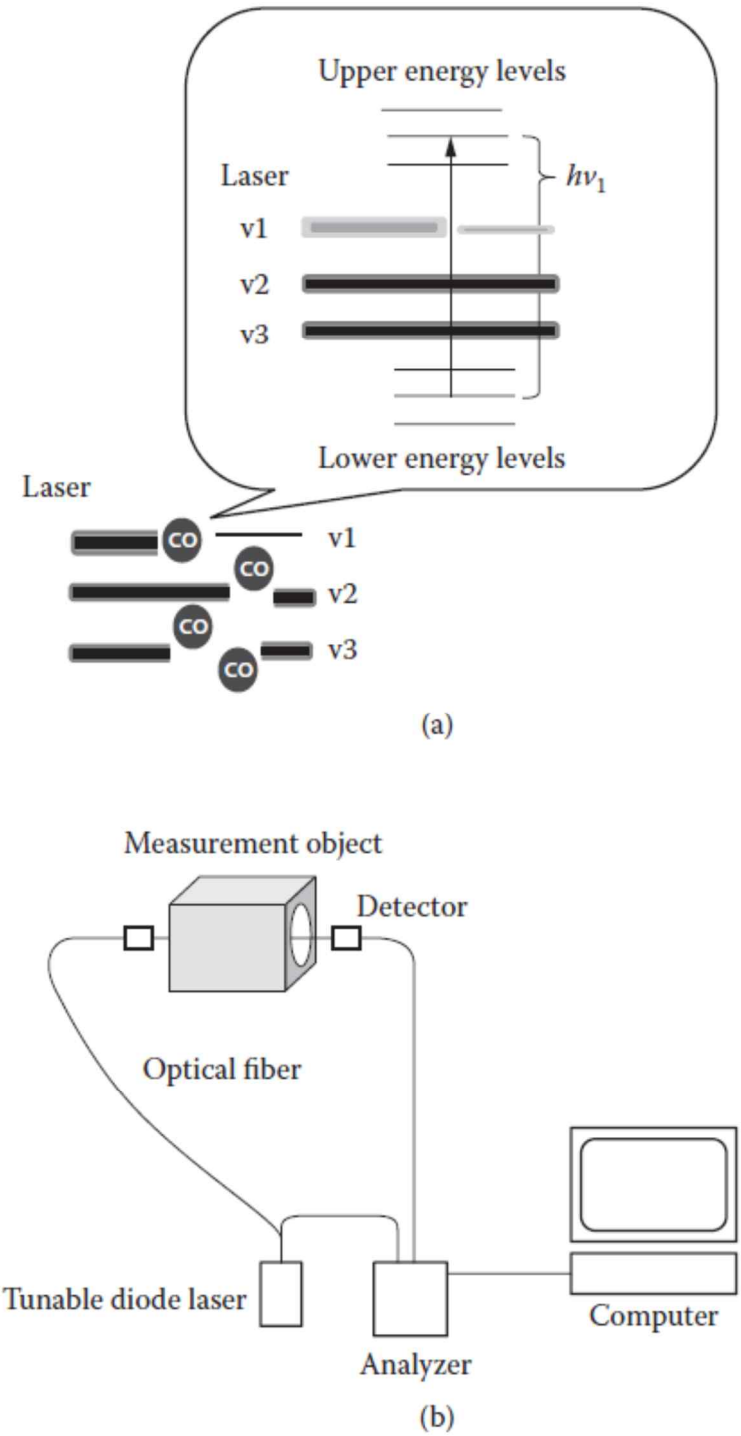

Fig. 2.4 Energy transfer process and typical TDLAS system

([33] Deguchi. Y., Industrial applications of Laser Diagnostics, New York, CRS Press: Taylor & Francis 2011, pp.14.)

2.4.2 Absorption Data signal and fitting process

Fig. 2.5 shows an output of signal and reference. These two divisions become absorption spectra. In this study, a polynomial noise reduction technique [10-11] was used to calibrate noises such as an effect of beam steering and an attenuation of the light by dirt and so on.

Fig. 2.6 is an example of fitted spectra used at actual experiment signals in this study. To reduce an influence by electric circuits, bias error and balanced technique, the signal and reference are subtracted before amplification

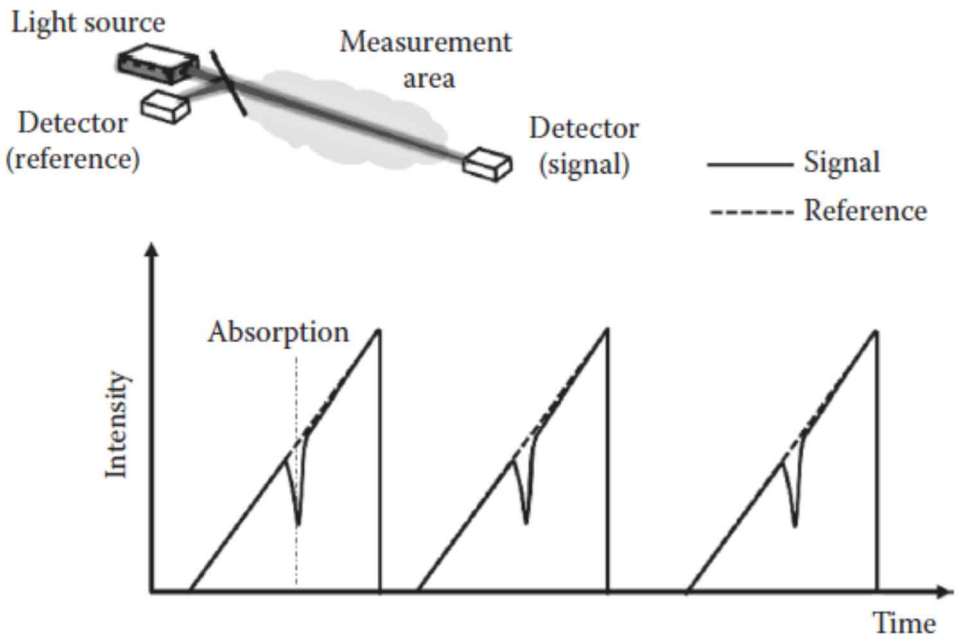

Fig. 2.5 Typical absorption signals

([33] Deguchi. Y., Industrial applications of Laser Diagnostics, New York, CRS Press: Taylor & Francis 2011, pp.177.)

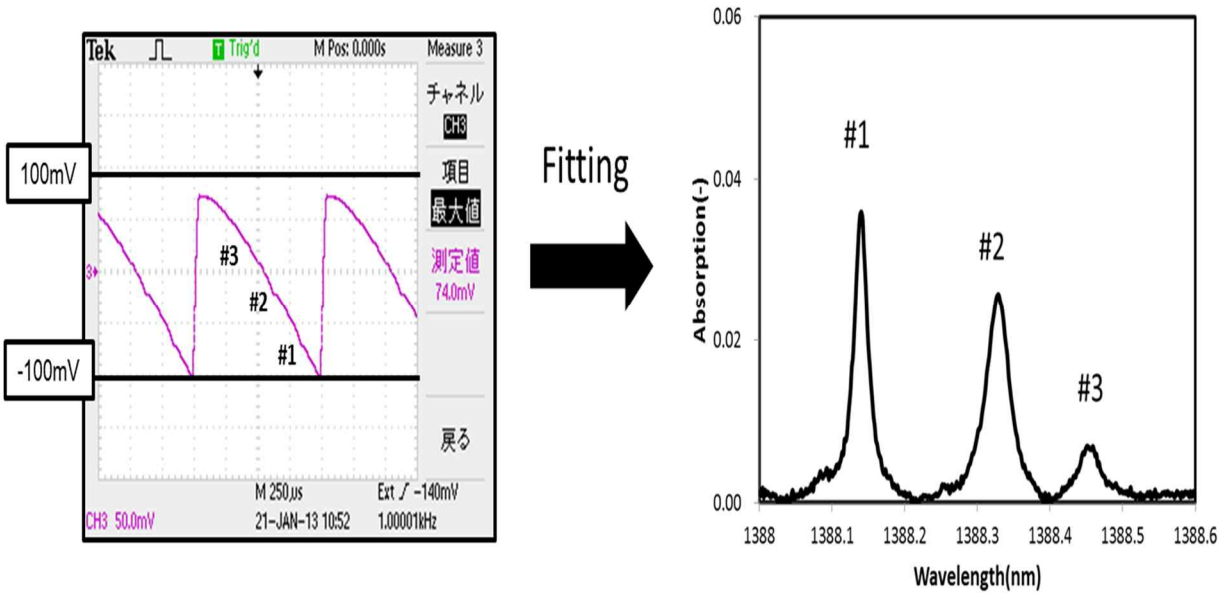

Fig. 2.6 A Fitting result of actual experiment signals

2.5 Temperature dependence of absorption lines

Fig. 2.7 shows the temperature dependence on absorption lines of water vapor at the range of 1388.0 ~1388.6 nm. Theoretical H_2O absorption spectra was calculated from the HITRAN2008 database [34] at 300 K, 500 K, 700 K and 900 K shown in Fig. 2.7(a), (b), (c), (d).

Fig. 2.7 (e) shows the absorption value calculated from 300 K to 1500 K in the three absorption lines. These absorption lines located at 1388.135 nm (#1), 1388.326 nm (#2), and 1388.454 nm (#3) have an independent sensitivity.

Fig. 2.7 (f) is the absorption ratios of two patterns (#1/#2, #1/#3) made from calculated intensities of the selected three absorption lines. Most of reconstruction algorithms for calculating temperature distribution in CT-TDLAS are based upon two-line thermometry method. In this study, curve fittings using three lines, six lines and whole lines were implemented by these spectra information. Therefore, it is very important to understand temperature dependence of absorption lines in CT-TDLAS.

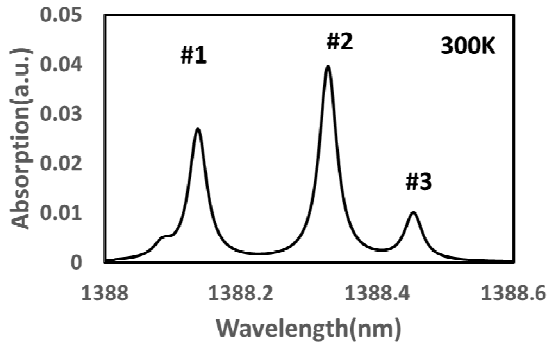

(a) 300 K, 0.1MPa

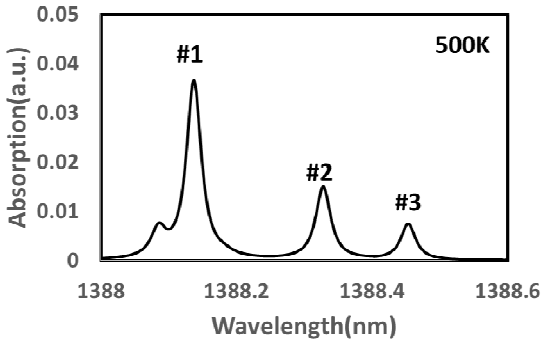

(b) 500 K, 0.1Mpa

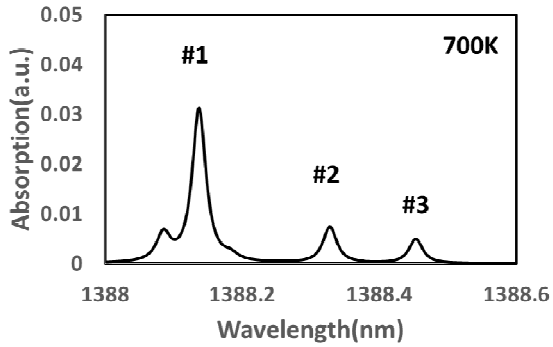

(c) 700 K, 0.1Mpa

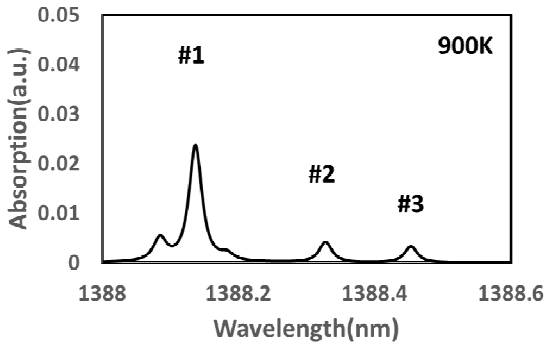

(d) 900 K, 0.1Mpa

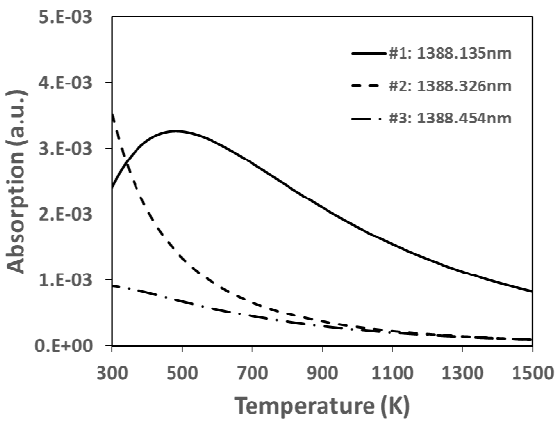

(e) Temperature dependence of three lines

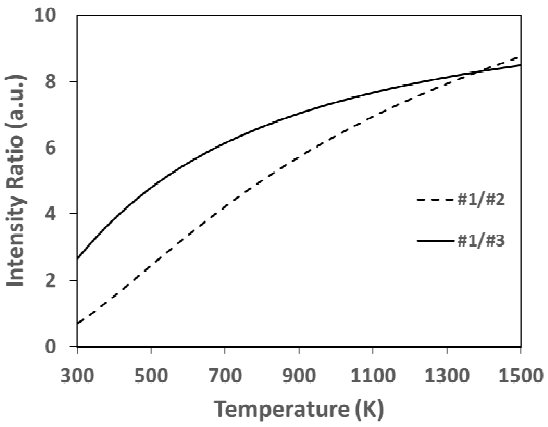

(f) Results of intensity ratio

Fig. 2.7 Temperature dependence of absorption lines (H_2O 1388.0 ~1388.6 nm)

2.6 CT-TDLAS

As noted earlier, the characteristics of TDLAS have non-intrusive and very fast as a diagnostic technique. Combined with computed tomography, the technique of TDLAS has the potential to provide more accurate information about an analysis of temperature and concentration distributions of a species. Nowadays, the various CT algorithms (ART, MART, SART, FBP etc.) have been developed and tested on the simulation of 2 D temperature and concentration distributions.

Fig. 2.8 shows the concept of analysis grids and laser beam paths. The absorption happens on the optical path passed through the each grid. The absorption signals become an integrated absorption value of the optical path. The integrated absorbance A across a specific spectral line in the laser path j can be written as follows [6].

$$A_{\lambda,j} = \sum_{i=1}^{I} n_i L_{i.j} \alpha_{\lambda,i} \tag{2.16}$$

Where the subscript i represent the grid point (I = 1, 2, … I), λ is transition frequency, n_i is number density at grid i, $L_{i,j}$ is optical path length at grid i and path j, $\alpha_{\lambda,i}$ is absorption coefficient at wavelength λ and grid i. Therefore, the absorption signals used an integrated value of the several optical paths become reconstructed 2D temperature and concentration distributions by the CT method. Because the integrated absorbance is dependent on both temperature and concentration, the temperature distribution is needed to be calculated as more than two different absorbance values.

Fig. 2.9 shows the procedure of CT analysis. The measured H_2O absorption spectra is normalized and compared to those of theoretical spectra to minimize the MSE (Mean Squared

Errors). The error is calculated and minimized from each of all laser paths. This procedure is described at the next section in detail.

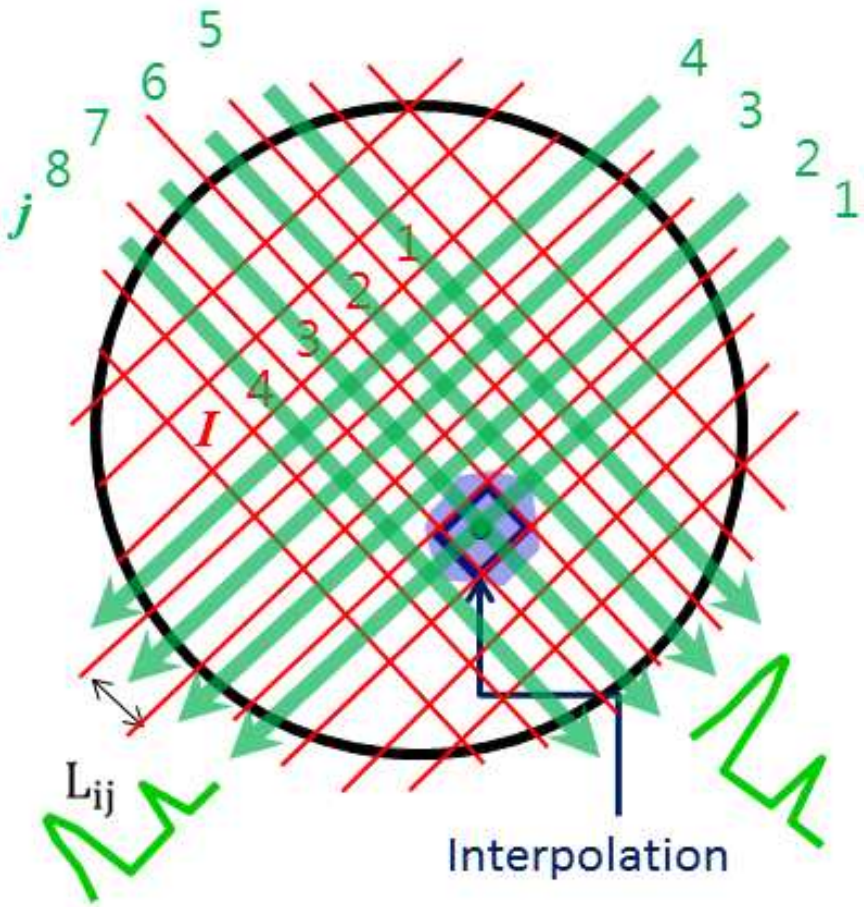

Fig. 2.8 Analysis grid and laser beam path

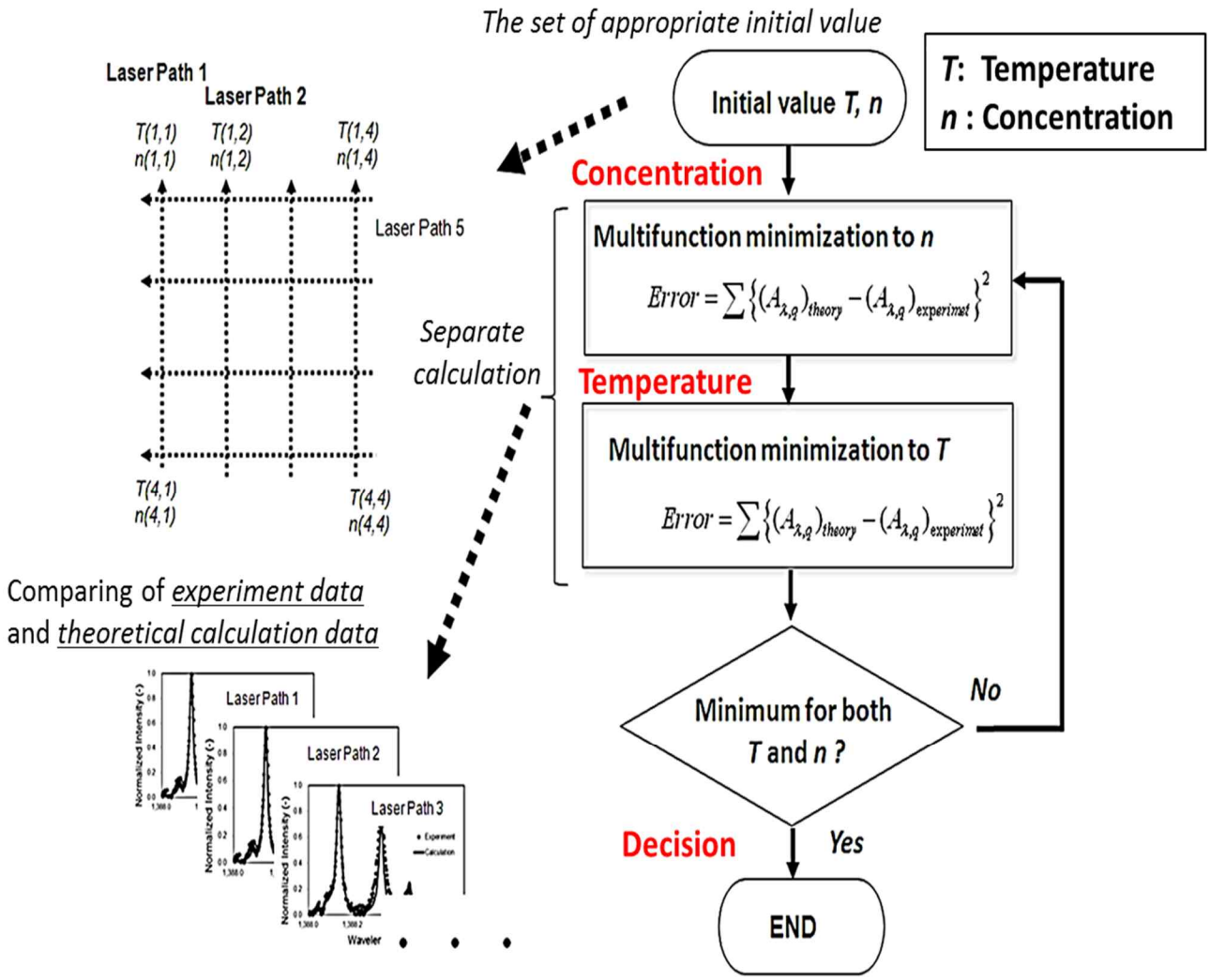

Fig. 2.9 CT analysis procedure

3. Enhancement of Reconstruction Data

3.1 Enhancement of ART and MART method

ART [36] is a class of iterative algorithms used in computed tomography. ART method was introduced by Gordon, Bender & Herman (1970) for solving the problem of three dimensional reconstruction from projections have been used for many years in radiology. In ART method, it is assumed the cross-sections consist of arrays of unknowns and reconstruction problem can be formulated as a system of linear equations. Eq. 3.1 represents the equation used for ART algorithm. Unknown absorption coefficients are calculated implicitly.

$$\alpha_{v1,j}(i)^{(k+1)} = \alpha_{v1,j}(i)^{(k)} + \beta \frac{A_{v1,j} - \sum_{i=1}^{I} \alpha_{v1,j}(i)^{(k)} \cdot L_{ij}}{\sum_{i=1}^{I} L_{ij}^{\ 2}} \qquad (3.1)$$

Here, α_{v1} is the absorption coefficient at the wavelength $v1$(1388.135 nm), $A_{v1,j}$ is the absorbance from the experiment data, k is the iteration number and β is the relaxation parameter, which plays an important role in determining a convergence rate.

As other algorithm, MART algorithm [37-38] is used in this study. It was known that MART algorithm allows less calculation load and less calculation errors than the ART algorithm. MART algorithm is written as follows.

$$\alpha_{v1}(\mathrm{i})^{(k+1)} = \alpha_{v1}(\mathrm{i})^{(k)} + \left[\frac{A_{v1,\mathrm{j}}}{\sum_{i}^{I} \alpha_{v1}(\mathrm{i})^{(k)} \cdot L_{ij}}\right]^{\beta L_{ij}} \qquad (3.2)$$

With initial or previous values of *n(i, j)* and *T(i, j)*, $\alpha_{v1}(i)$ values were iteratively calculated using Eq. 3.3.

$$\alpha_{v1,j}(i) = \mathrm{n(i,j)} \cdot S_{i,j}\{T(i,j), v1\} \cdot G_{vi,j} \cdot P \tag{3.3}$$

The integrated absorbance '*A*' across a specific spectral line in the laser path *j* is calculated as follows Fig. 3.4 and this minimization method was calculated by the following equation.

$$\mathrm{Error} = \sum\left\{(A_{\lambda,j})_{theory} - (A_{\lambda,j})_{experiment}\right\}^2 \tag{3.4}$$

The measured H_2O absorption spectra was normalized and compared to those of theoretical spectra to minimize the MSE (Mean Squared Errors). The error was calculated and minimized from each of all laser paths. This procedure is explained in Fig. 2.9. All values of $\alpha_{v1,j}(i)$ at all grids points were iteratively calculated using the ART and MART methods until convergences. The final values of *T(i, j)* and *n(i, j)* after iterations were then reconstructed for temperature and concentration fields. It is needed to evaluate their performances on ART and MART methods. In this chapter, the performance of the ART and MART algorithm was evaluated by using the burner experiment data. The experimental data was obtained by the experimental setup as shown in Fig. 3.1 (a). A DFB laser (NTT Electronics Co., NLK1E5GAAA) at 1388 nm with scanning range of 0.6 nm was used to detect H_2O vapor absorption spectra. The laser wavelength was scanned at 1 kHz and absorption spectra were measured to calculate instantaneous 2 D temperature distribution using 8-path measurement cells as shown in Fig. 3.1 (b). Laser beam was separated by an optical fiber splitter (OPNETI CO., SMF-28e 1310 nm SWBC 1×16) and the separated laser beams were irradiated into the target area by 8 collimators(THORLABS Co., 50-1310-APC). The transmitted light intensities were detected

by photodiodes (Hamamatsu Photonics and G8370-01), and their intensity signals were stored into the host computer. The data acquisition rate was set to 500 kHz (500 data points on every 1 scan of absorption spectra) and temperatures in the measurement plane were also measured by chromel-alumel thermocouples with a diameter of 100μm (KMT-100-100-120), in order to compare both the results. Methane gas was used as a fuel. During all experimentations, mass flow velocities of CH_4 and air were constantly maintained at each of 30 ℓ /min and 102 ℓ /min. The diameter of burner was manufactured to 40 mm, and the laser paths were set to 8 mm spacing with each other. The temperature and the concentration of H_2O measured at the burner center by sensors (thermocouple and humidity sensor) were 438 K and 2% respectively.

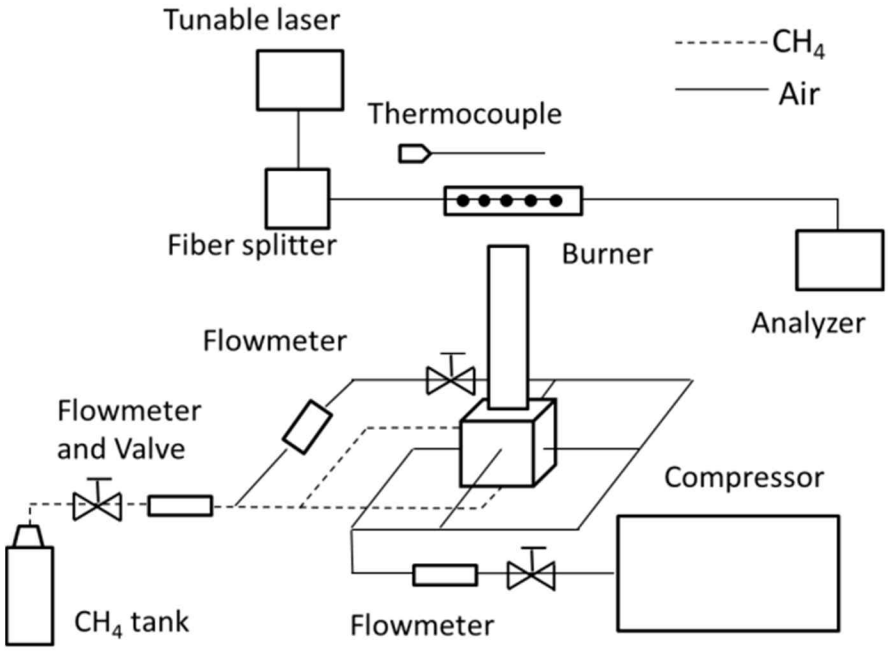

(a) Schematic experiment system

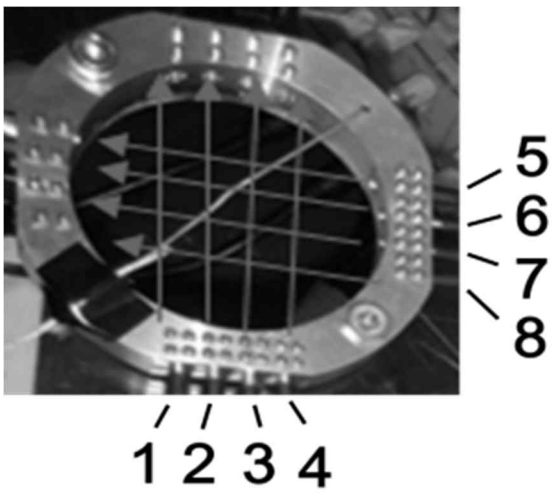

(b) 8 path cell

Fig.3.1 Experimental setup and cell

Fig. 3.2 shows the measured absorption spectra on the 8-path lasers across the Bunsen burner. The laser paths 3, 4, 7 and 8 in Fig.3.2 were set to high temperature regions of the burner. It can be seen that the ratio of line intensities of #1 and #2 has strong temperature dependences as already explained in Fig. 2.7 (e) and (f). The laser paths 1, 2, 5 and 6 were set to low temperature region and the ratio of line intensities of #1 and #2 has lower values than those of the laser paths 3, 4, 7 and 8. These absorption values were used for temperature reconstructions. For temperature reconstructions, MART algorithm was adopted, and its performance was validated.

Implicit solution was performed until all values of $\alpha_{v1}(i)$ at all grids points converged to constant values. Iterative calculation was made for #1 (v1, 1388.135 nm) at first, next for #2 (v2, 1388.326 nm). When performing iterative calculations, the temperatures measured by thermocouples were used as the initial values. Then, the initial values of gas concentrations were obtained by the initial values of temperature using Eq. 3.3. Absorption coefficients were newly calculated using the absorption values from the horizontal laser 1 to 4 using Eq. (5). After iterative calculations for the horizontal lasers (1~4), the absorption coefficients of the vertical lasers (5~8) were also renewed.

Fig. 3.3 shows the result of MSE (Mean Squared Errors) obtained by ART algorithm for all iteration numbers. The relaxation value (β) was changed in the range of ($0.05 < \beta < 1$). For the case of ART algorithm, the result of MSE became the smallest values when β was set to 0.1. The MSE was saturated within the iteration number 50. This implies that the iteration numbers do not need to be large if an optimal β is chosen.

Fig. 3.4 shows MSE obtained by MART algorithm during all iteration calculations. β values were also changed in the range of ($0.05 < \beta < 1$). In case of ART algorithm, the MSE was the smallest values when β was set to 0.5. The MSE was saturated within the iteration number 10.

This implies that the calculation time is 5 times shorter than that of ART algorithm if an optimal β is chosen.

Fig. 3.5 shows the comparison of calculation performances between ART and MART algorithms. It could be inferred that errors by MART algorithm were less than those by ART algorithm with rapid calculation convergences.

Fig. 3.6 shows the result of temperature and concentration distributions obtained by MART algorithm. It could be seen that peak temperature and concentration regions were located to the edges. This was due to the fact that the center of flame burner (high temperature region) was installed at the edge of the measurement apparatus. The peak values of the reconstructed temperature and H_2O concentration were each of 429.7 K and 2.13% respectively.

Therefore, it was validated that calculation errors by MART algorithm were less than those by ART algorithm. Further, the calculation speed of MART algorithm was 5 times faster than that of ART algorithm. The minimum iteration number to be saturated at the minimum values of error was 10. This implies that several dozens of iteration number would be enough for attaining the minimum errors. Therefore, MART method was adopted in this thesis and its performance was validated for CT-TDLAS.

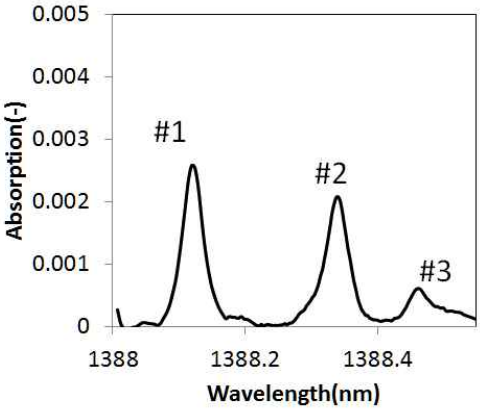

(a) Laser path1

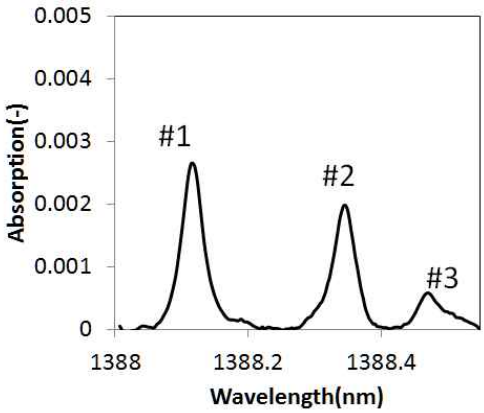

(b) Laser path2

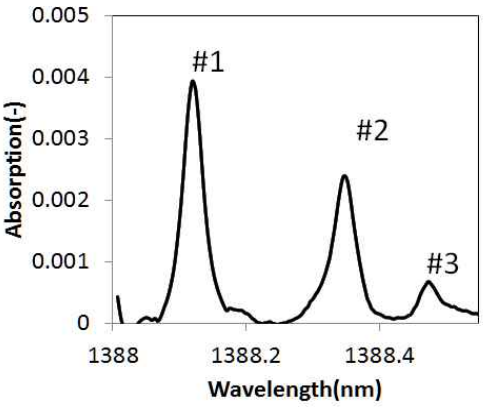

(c) Laser path3

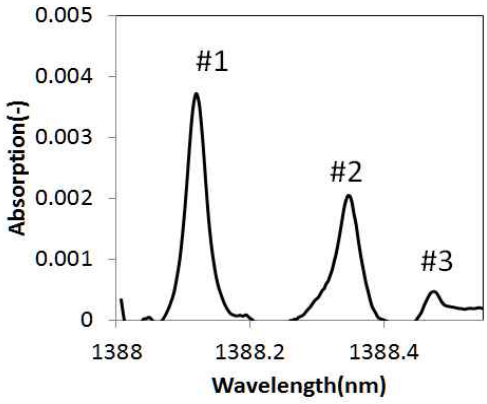

(d) Laser path4

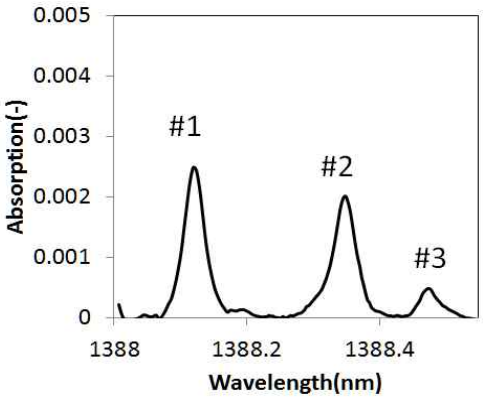

(e) Laser path5

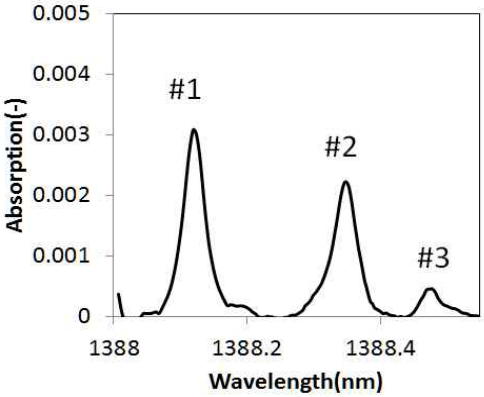

(f) Laser path6

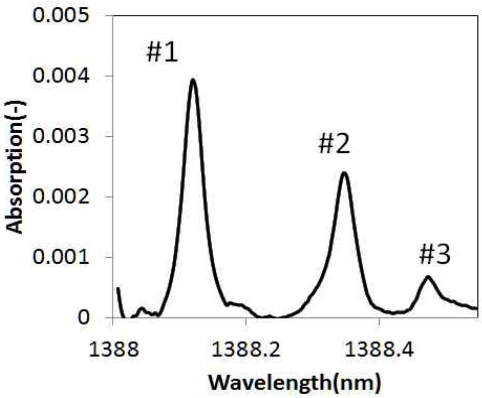

(g) Laser path7

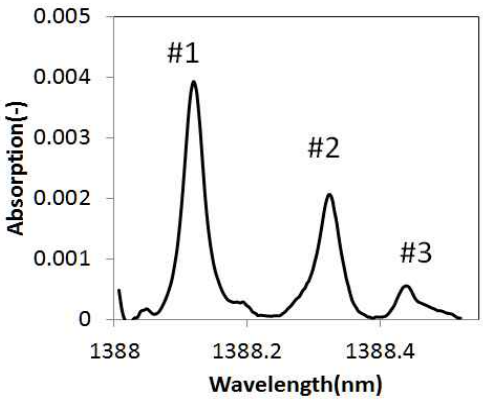

(h) Laser path8

Fig. 3.2 The measured absorption spectra H_2O for 8 path lasers.

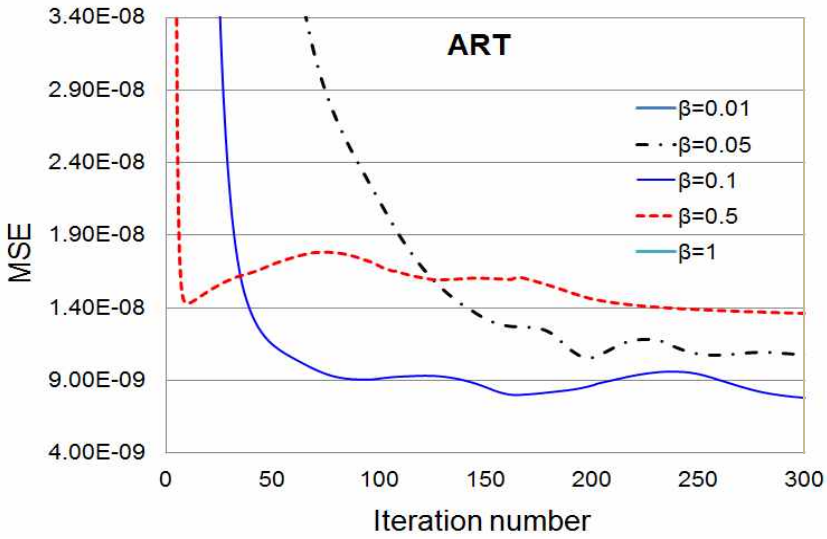

Fig. 3.3 Variations of MSE with iteration numbers for relaxation parameters in ART algorithm.

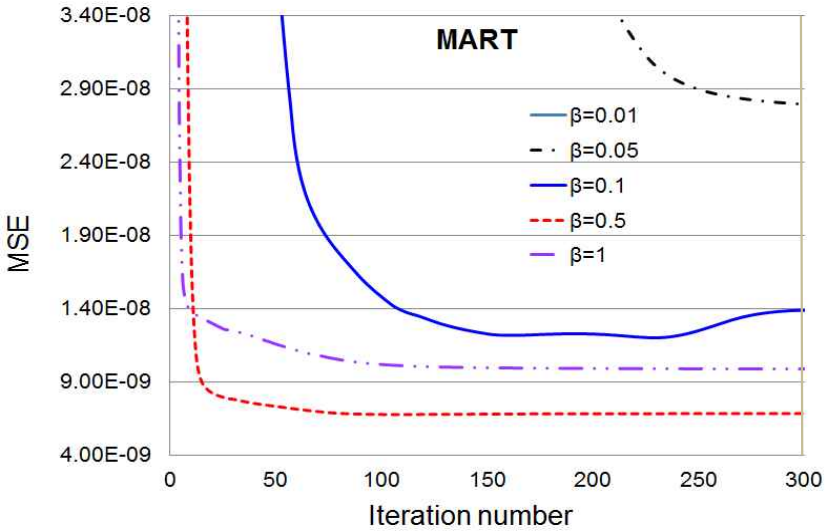

Fig. 3.4 Variations of MSE with iteration numbers for relaxation parameters in MART algorithm.

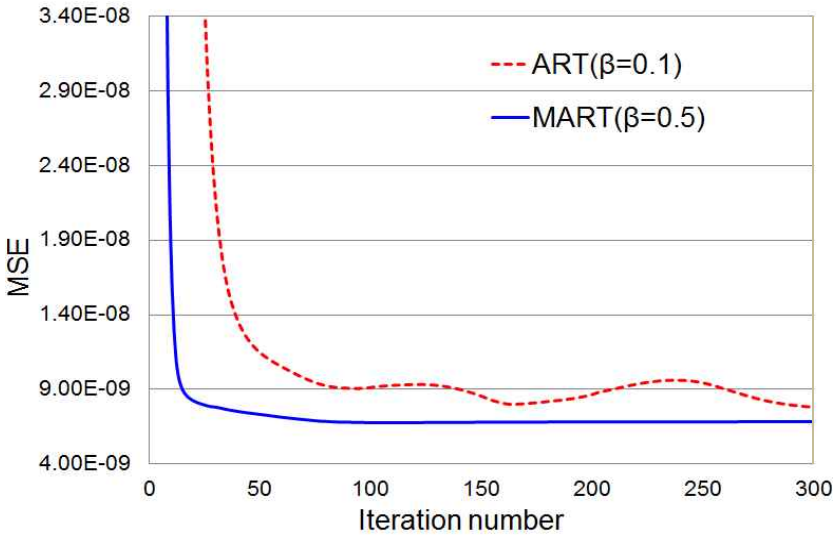

Fig. 3.5 The comparisons between ART algorithm and MART algorithm.

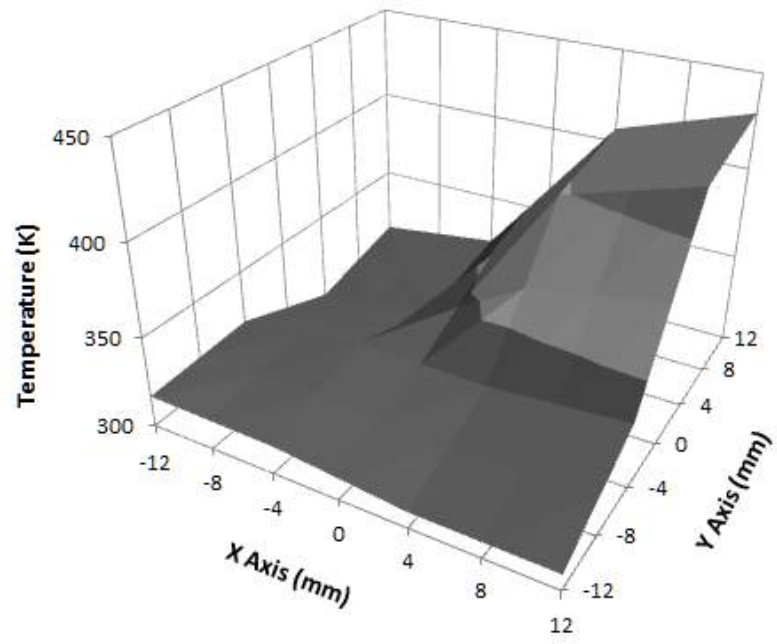

(a) Temperature distribution

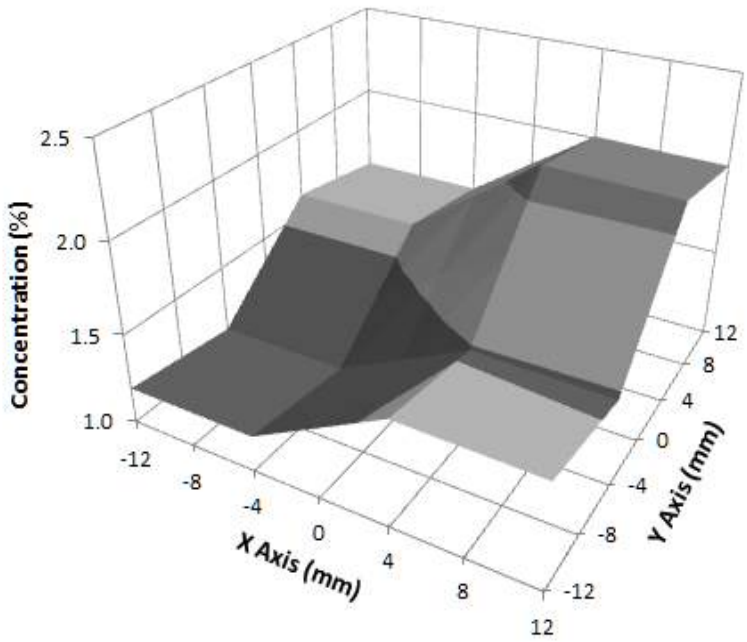

(b) Concentration distribution

Fig.3.6 The result of temperature and concentration distributions obtained by MART.

3.2 The estimate of initial value

A selection of initial value has influence on the performance of computed tomography during convergence calculation. So, it is important that a neighboring initial value is provided at the reconstruction calculation. If the initial of large error is given, a direction of calculation would be diverged. Eventually, the unintelligible results would be popped out far from a convergence.

In this chapter, MLOS (Multiple Line of Sight)[38] and PLOS (Plus Line of Sight) methods are introduced to estimate an appropriate initial value. By using already known absorptions of intersected lasers, the ratio at gird point is assessed. Information of the ratio can be converted temperature by Fig. 2.7 (f).

Fig. 3.7 shows an estimate process of initial temperature. MLOS and PLOS methods estimating the initial temperature are written as follows equations.

$$R_{PLOS} = \frac{A_{\#1,p} + A_{\#1,q} \cdots}{A_{\#2,p} + A_{\#2,q} \cdots} \tag{3.3}$$

$$R_{MLOS} = \frac{A_{\#1,p} \times A_{\#1,q} \cdots}{A_{\#2,p} \times A_{\#2,q} \cdots} \tag{3.4}$$

Here, the subscript p and q are number of laser beams, the subscript #1 and #2 are wavelengths at peak point and A is absorption at wavelength of peak point (#1, #2). By using these methods, the reconstructed calculation can be converged without divergence.

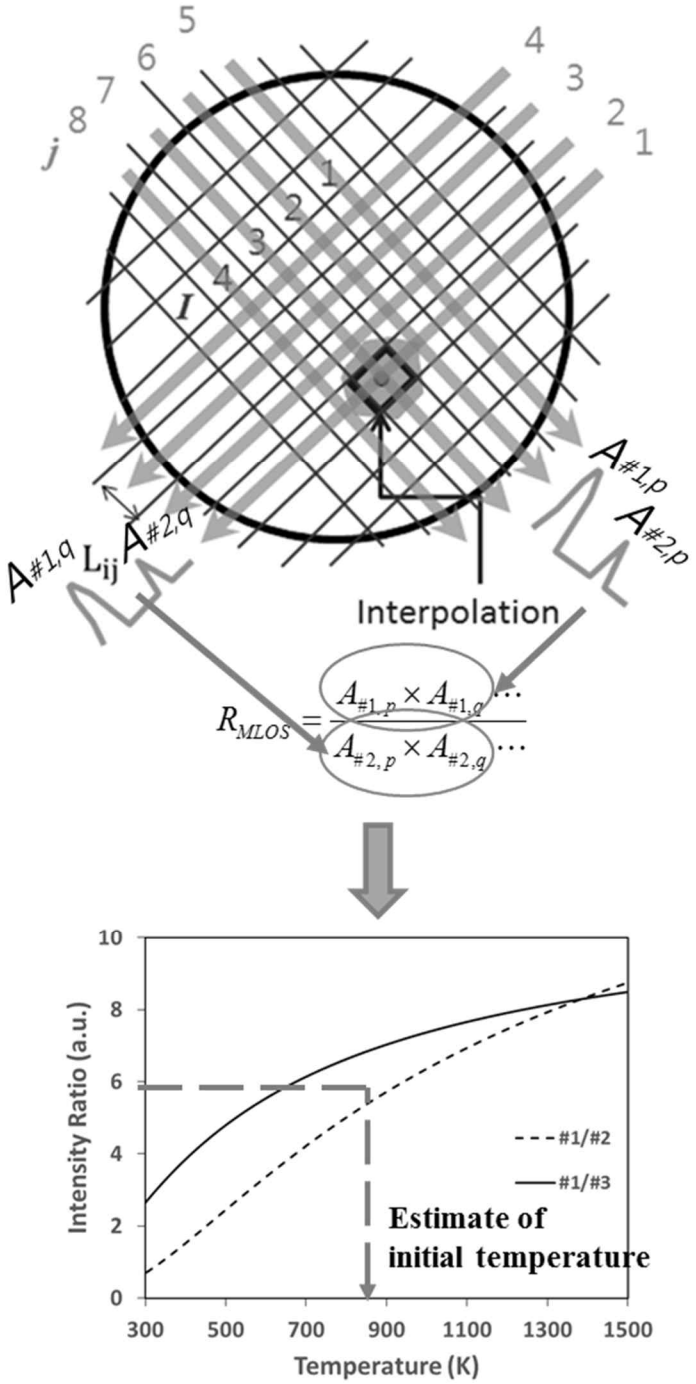

Fig. 3.7 Estimate process of initial temperature

3.3 Decision of experimental broadening factors

3.3.1 Experiment apparatus

It is important that more exact broadening factors are investigated to make accurately the curve fitting of theoretical and experimental absorption spectra. A flat plate burner can constantly maintain the temperature of the region laser beams pass. The absorption experiment data would be ideally gathered under constant temperature conditions.

Fig 3.8 (a) shows a measurement cell was made up to 1 path laser and Fig.3.8 (b) shows the experimental equipment of flat plate burner in this study.

A DFB laser (NTT Electronics Co., NLKE5GAAA), a semiconductor laser capable of fast and continuous wavelength with scanning range of 0.6 nm, was used to measure water vapor absorption spectra at 1388 nm. This laser wavelength was scanned at 1kHz frequency. The transmitted lasers were detected by photodiodes (Hamamatsu Photonics, G8370-01) and then the detected signals were taken by analyzers (8861 Memory Highcoda HD Analog16, HIOKI).

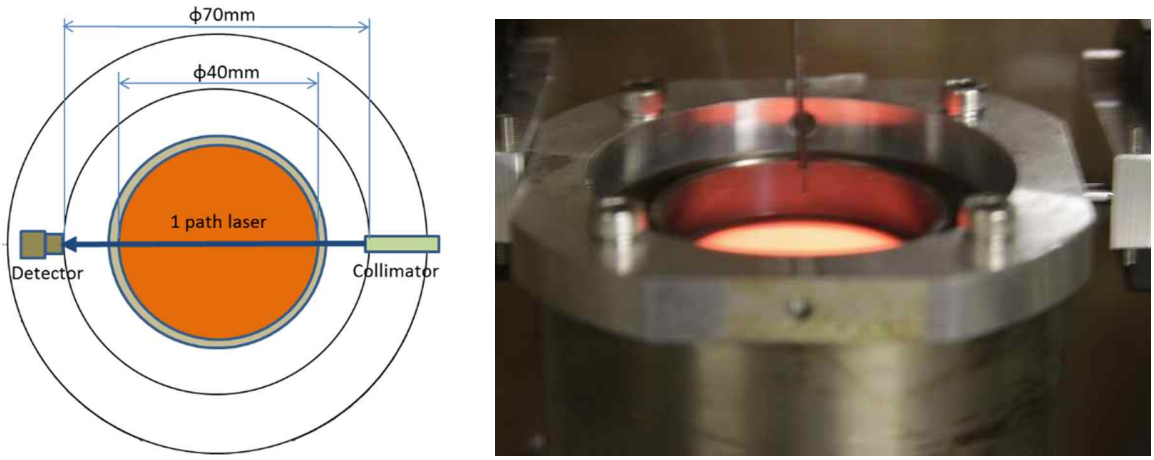

(a) Measurement cell of 1 path laser

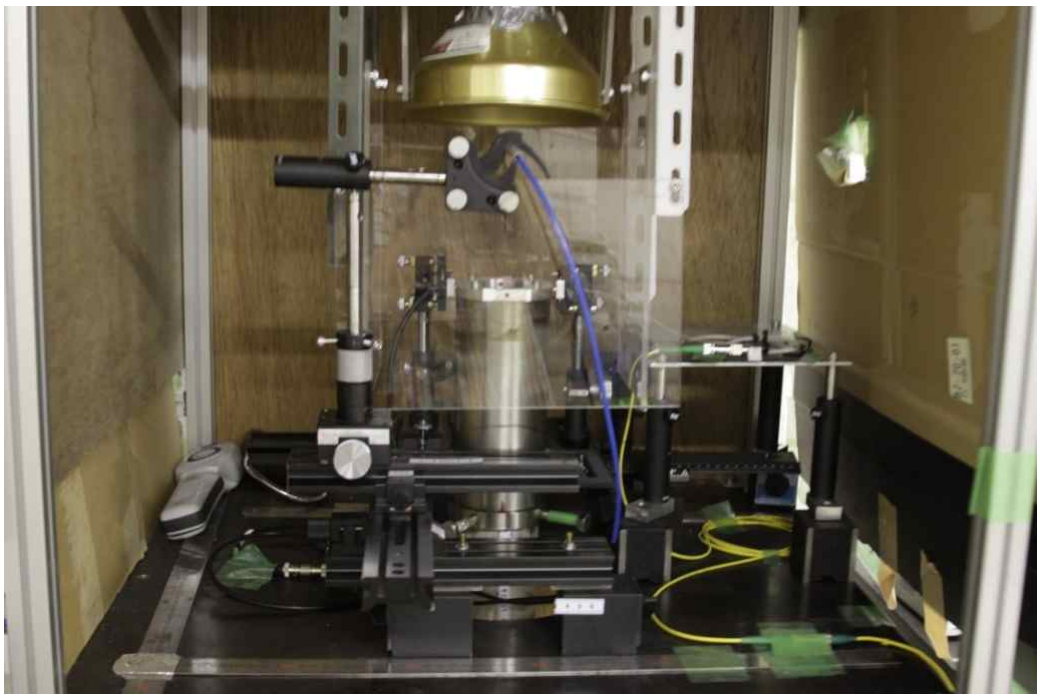

(b) Experimental equipment of the flat plate burner

Fig 3.8 Experimental equipment of the flat plate burner

3.3.2 Experimental repeatability test

Fig 3.9 shows a good repeatability of the flat plat burner at the different temperature. The repeatability experiment at a temperature range of 400 K~700 K similar to engine exhaust gas was conducted a total of 3 times. The results in figure indicate the measurement temperatures are constantly maintained. In other words, it means that a laser beam is able to pass in the steady temperature distrubution.

- Measurement tool: Thermocouple
- Area : 32 mm × 1 mm
- Grid size : 2 mm × 1 mm
- Total measurement cells : 17

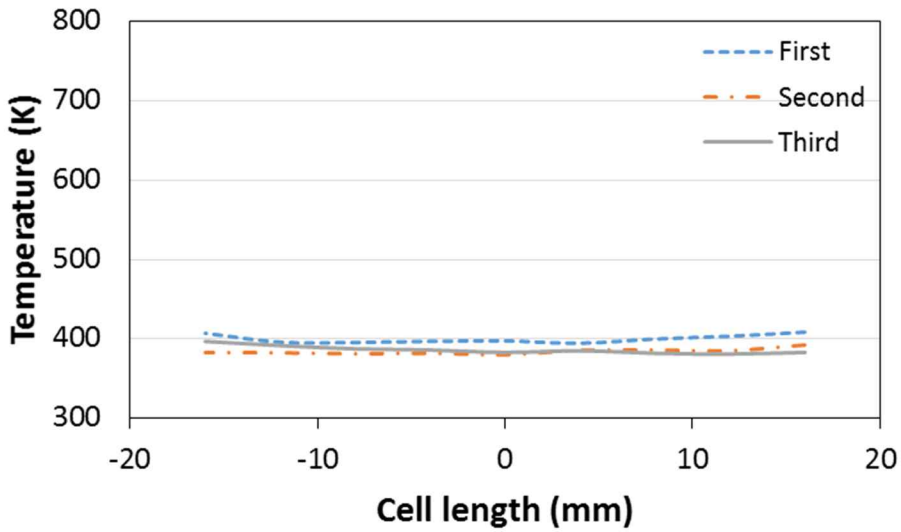

(a) 400 K

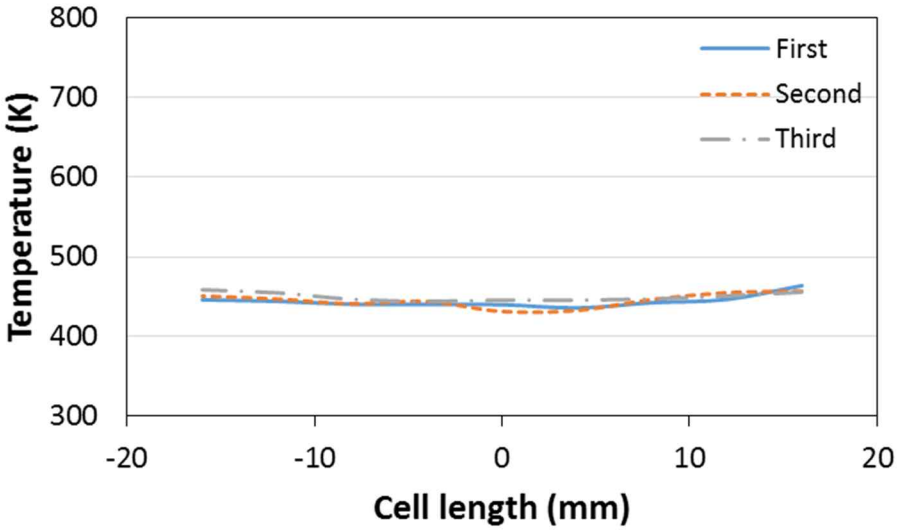
800
700
600
500
400
300
Temperature (K)
-20
-10
0
10
20
Cell length (mm)
First
Second
Third

(b) 450 K

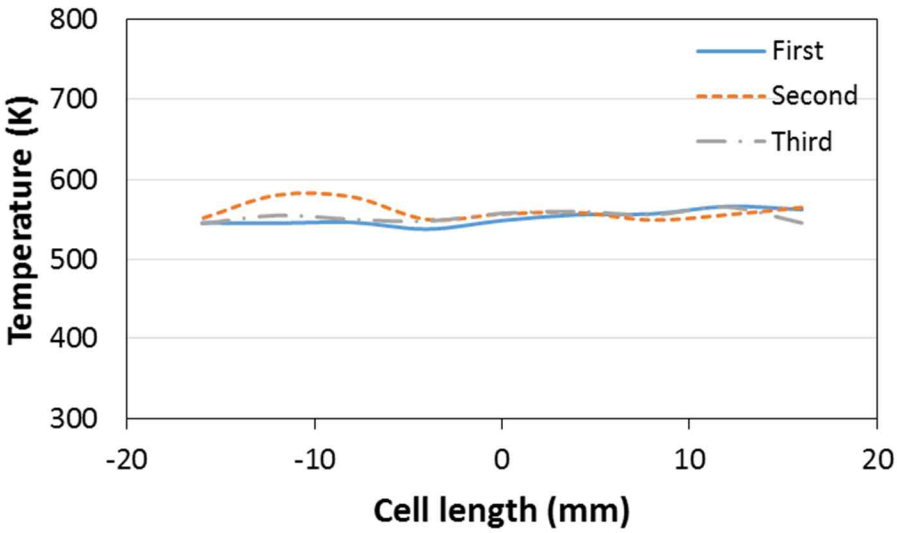
800
700
600
500
400
300
Temperature (K)
-20
-10
0
10
20
Cell length (mm)
First
Second
Third

(c) 550 K

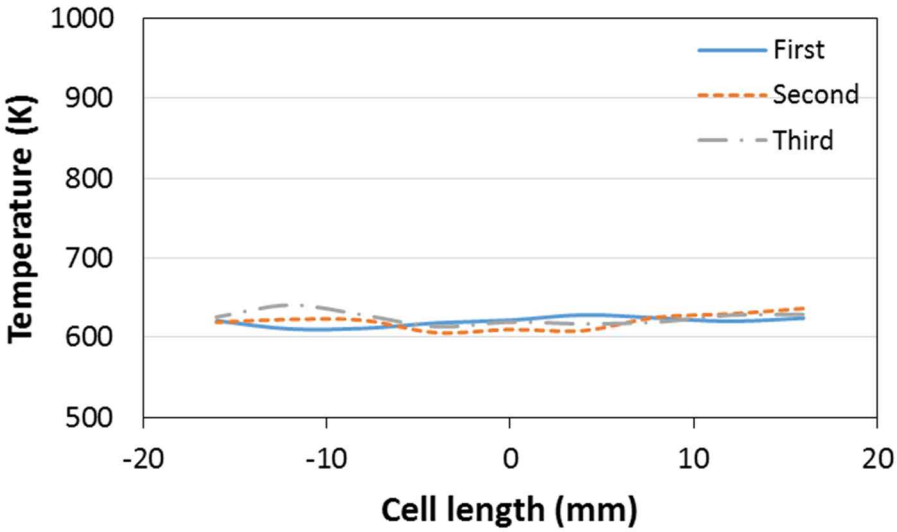

(d) 600 K

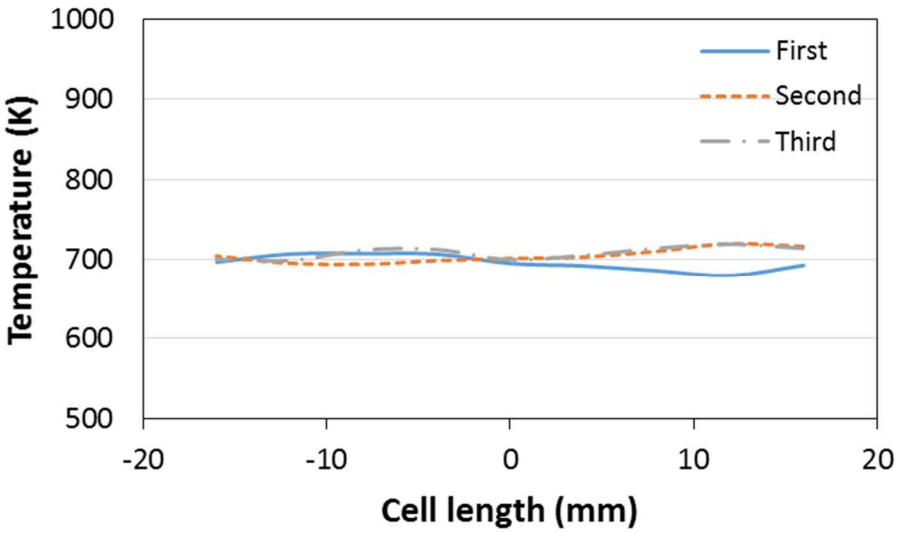

(e) 700 K

Fig 3.9 The result of experimental repeatability using flat plat burner at the varied temperature

3.3.3 Analysis of absorption graph

Fig 3.10 shows the analyzed absorption spectra from 1 path beam at the different temperature. These results were used to compare the theoretical absorption calculated from Eq. 2.2. The absorption spectra of both calculation and experiment are normalized and fitted by using LMS technique.

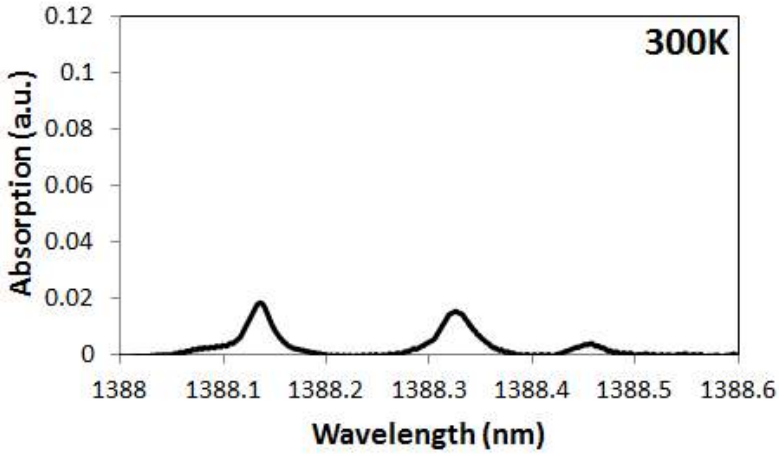

(a) 300 K

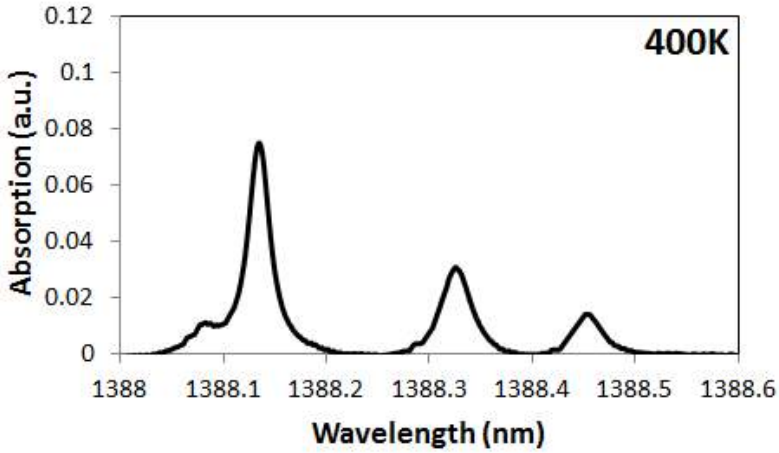

(b) 400 K

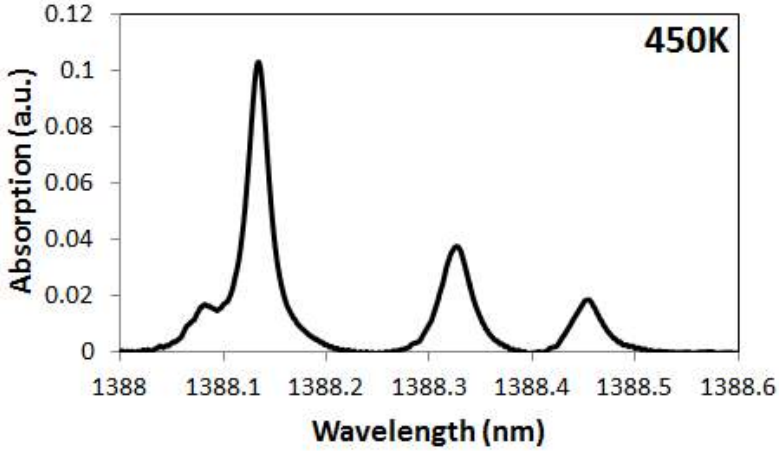
450K
Absorption (a.u.)
0.12
0.1
0.08
0.06
0.04
0.02
0
1388
1388.1
1388.2
1388.3
1388.4
1388.5
1388.6
Wavelength (nm)

(c) 450 K

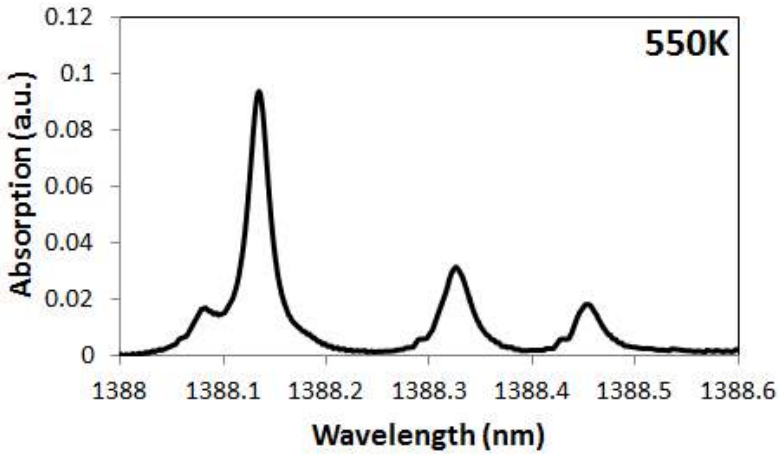
550K
Absorption (a.u.)
0.12
0.1
0.08
0.06
0.04
0.02
0
1388
1388.1
1388.2
1388.3
1388.4
1388.5
1388.6
Wavelength (nm)

(d) 550 K

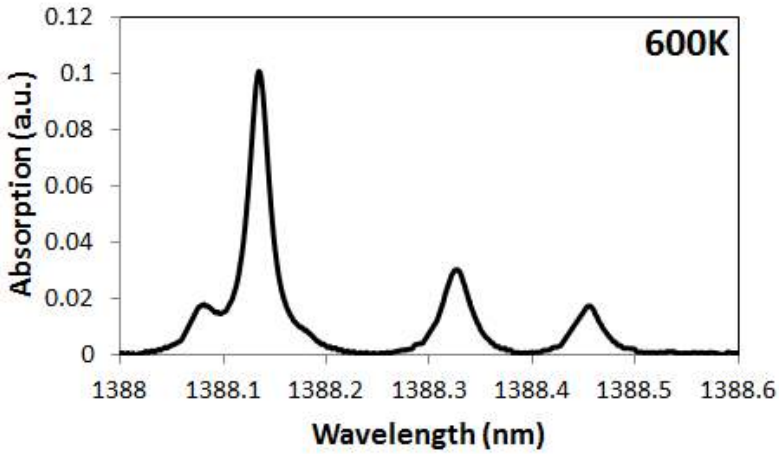

(e) 600 K

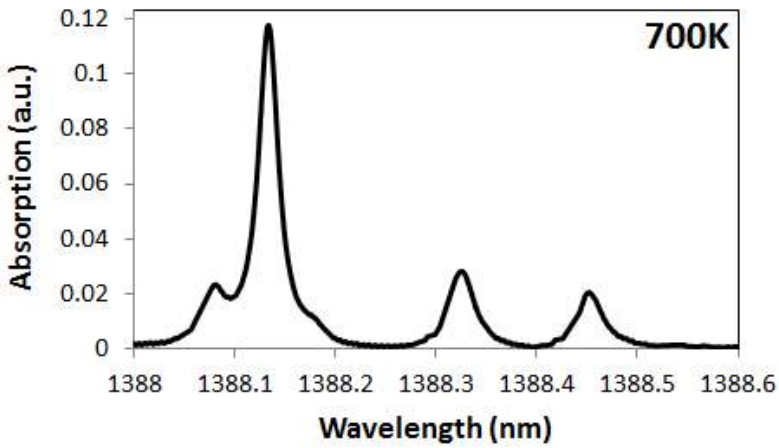

(f) 700 K

Fig 3.10 Experimental absorption graphs of H_2O spectra at 1338.0 ~ 1338.6 nm from laser experiment at flat plate burner

3.3.4 Investigation of broadening factors

For investigation of experimental broadening factors, $\gamma_j(T_0)$ and n_j unknown coefficient of Eq. 2.7 were calibrated by using absorption spectra data of Fig. 3.10. Changing of values $\gamma_j(T_0)$ and n_j, absorption spectra were fitted in the range of $0<\gamma_j(T_0)<1$ and $0<n_j<1$. Reaching a minimum error of fitting, selected broadening factors were finally $\gamma_j(T_0)=0.16$, $n_j=0.37$. Fig 3.11 shows the fitting results of the normalized absorption from calculation and experiment. Therefore, Voigt profile using these factors was calculated by Whiting method [39] in this study.

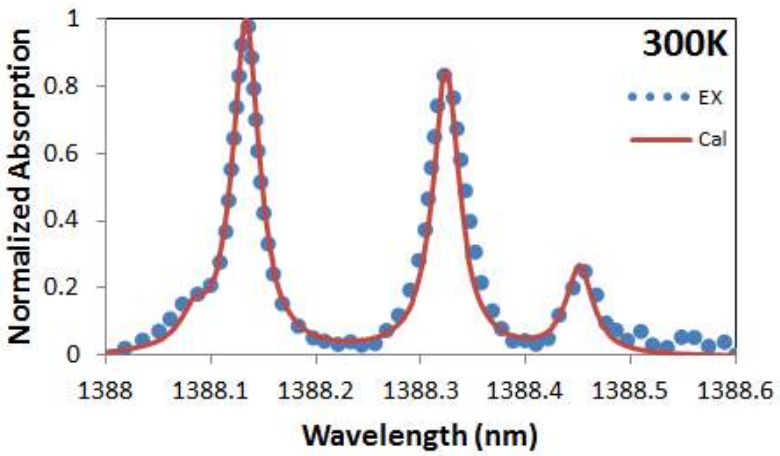

(a) 300 K

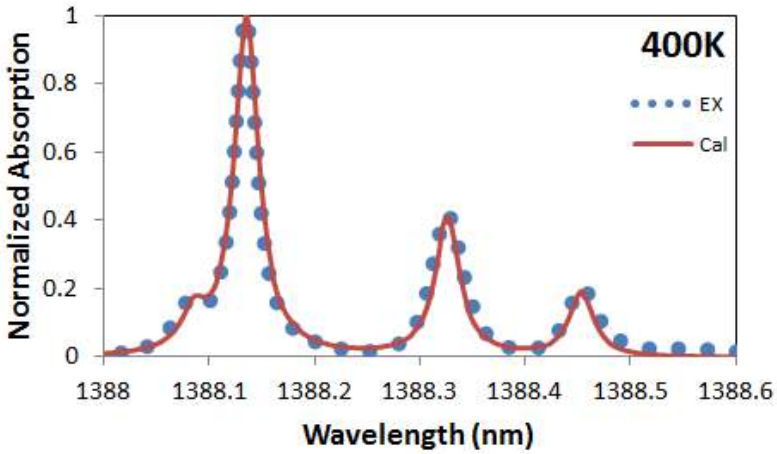
400K
EX
Cal
Normalized Absorption
1
0.8
0.6
0.4
0.2
0
1388
1388.1
1388.2
1388.3
1388.4
1388.5
1388.6
Wavelength (nm)

(b) 400 K

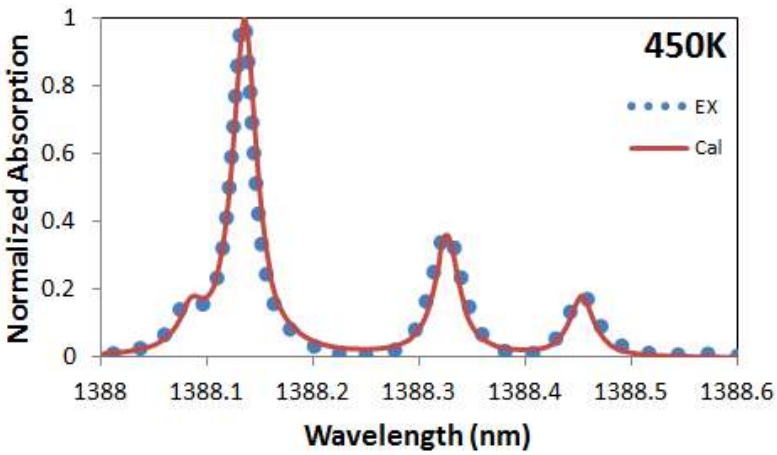
450K
EX
Cal
Normalized Absorption
1
0.8
0.6
0.4
0.2
0
1388
1388.1
1388.2
1388.3
1388.4
1388.5
1388.6
Wavelength (nm)

(c) 450 K

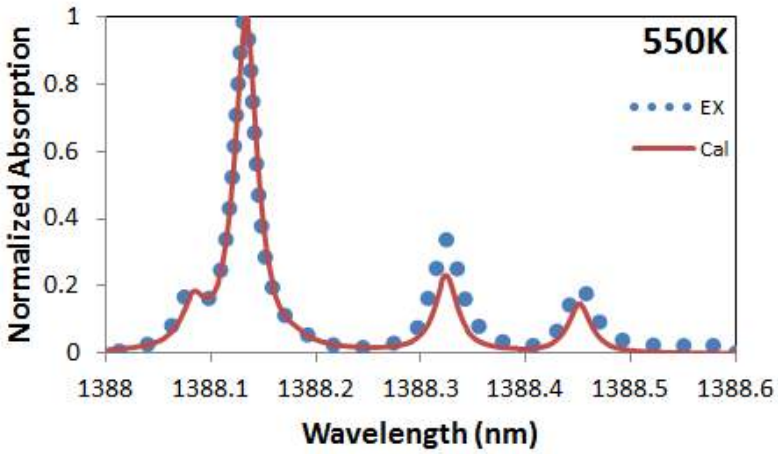
550K
EX
Cal
Normalized Absorption
1
0.8
0.6
0.4
0.2
0
1388
1388.1
1388.2
1388.3
1388.4
1388.5
1388.6
Wavelength (nm)

(d) 550 K

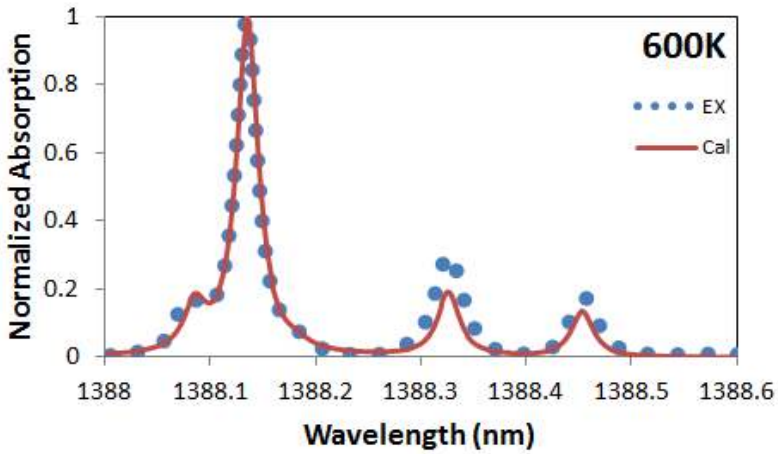
600K
EX
Cal
Normalized Absorption
1
0.8
0.6
0.4
0.2
0
1388
1388.1
1388.2
1388.3
1388.4
1388.5
1388.6
Wavelength (nm)

(e) 600 K

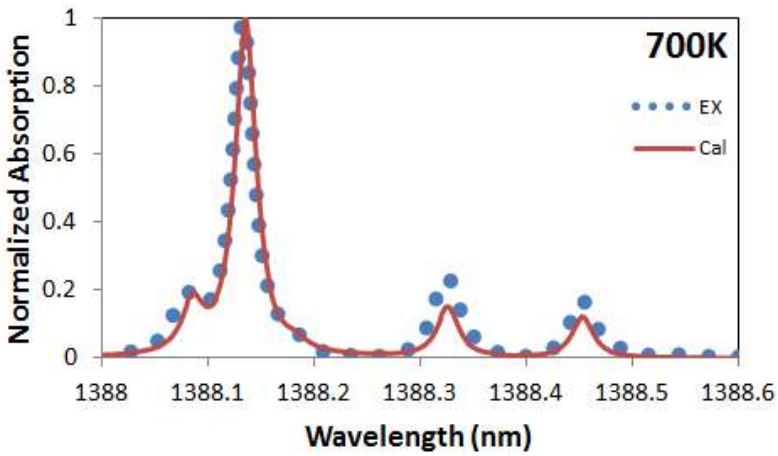

(f) 700 K

Fig 3.11 The Fitting results of normalized absorptions from calculation and experiment

4. Developments Signal Fitting Algorithms

4.1 Two-Ratios of Three-wavelength Fitting

In this chapter, it is introduced two ratio of three-wavelength fitting method. Also, a reconstruction performance of both a well-used generally two-line thermometry method and two ratio of three-wavelength fitting is compared and evaluated.

4.1.1 Making phantoms for 2D temperature distribution

To evaluate a performance of algorithm, the virtual temperature distribution was made by using Gaussian function. The Gaussian function is written as follows below equation.

$$T_{i,j} = T_0 + D \cdot exp\left(-\frac{((x-x_0)^2+(y-y_0)^2)}{\sigma^2}\right) \quad (4.1)$$

Here, x and y are cell length of X and Y axis, x_0 and y_0 mean a center position of X and Y axis. T_0 is a minimum temperature (T_0 =300 K), D is a deviation of temperature and σ means a gradient factor, which used 2.2 in this study. The maximum temperature was used 580 K. The calculation result of Gaussian temperature distribution shows in Fig. 4.1 (a). To evaluate a temperature distribution having a diverse pattern, the temperature distribution used by superimposed two Gaussian function. The superimposed two Gaussian function is written as below.

$$T_{i,j} = T_0 + \mathrm{D}_1 \cdot \exp\left(-\frac{((x-x_0)_1{}^2+(y-y_0)_1{}^2)}{\sigma_1{}^2}\right) + \mathrm{D}_2 \cdot \exp\left(-\frac{((x-x_0)_2{}^2+(y-y_0)_2{}^2)}{\sigma_2{}^2}\right) \quad (4.2)$$

The temperature peaks of two vortices were made by Eq. 4.2. The subscript 1and 2 mean vortex 1 and vortex 2. The information of used parameters shows below Table 4.1. Fig. 4.1 (b) shows the temperature distribution made by using superimposed two Gaussian function.

Table 4.1 Information of parameters used for two Gaussian function

Fig.4.1(a)	**X_0**	**Y_0**	**Deviation of temperature (D)**	**Sigma (σ)**
Vortex 1	0	0	280	8.0
Fig. 4.1(b)	**X_0**	**Y_0**	**Deviation of temperature (D)**	**Sigma (σ)**
Vortex 1	-8	0	250	8.0
Vortex 2	8	0	280	8.0

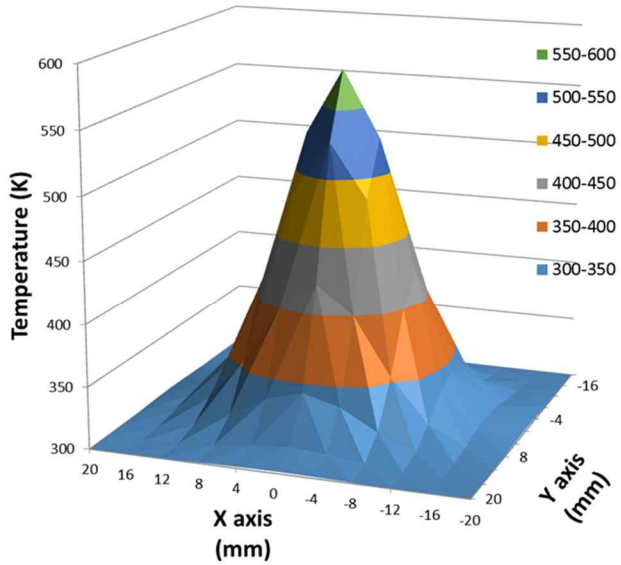

(a) 2D Temperature distribution made by Gaussian function

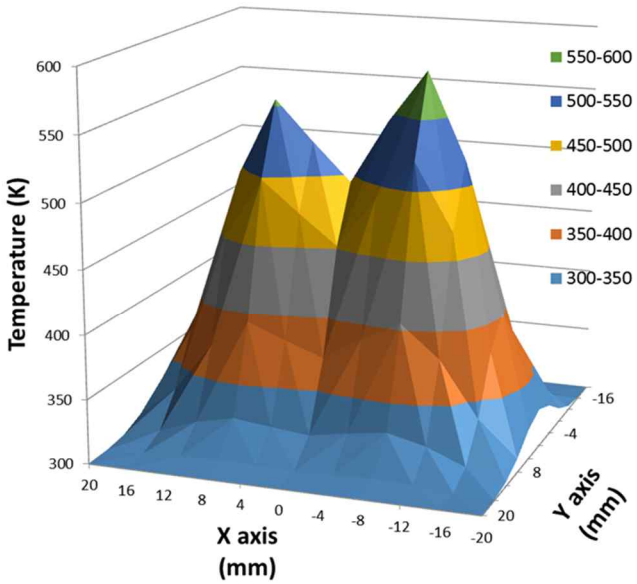

(b) 2D Temperature distribution made by superimposed two Gaussian function

Fig. 4.1 Phantoms for 2D temperature distribution

4.1.2 Information analysis grids and laser beams

Fig 4.2 shows the analysis grids and 22 beam paths in this study. The dimension of grid is 11×11 and total number of grids are composed of 121 square mesh. The width of mesh is 4 mm. The interpolation means domain of interest based on absorption of line-of-sight. In each of grids, the temperature and concentration of species are included. From these information absorptions of 22 beam paths were calculated as follows Eq. 4.3.

$$A_j = \sum_i^I n_{i,j} L_{i,j} \alpha_{i,j} \tag{4.3}$$

Here, A_j is absorption of laser beam j and means a sum of all cells beam j go through on region of measurement. In this study, $L_{i,j}$ (unit cell length) is 4 mm.

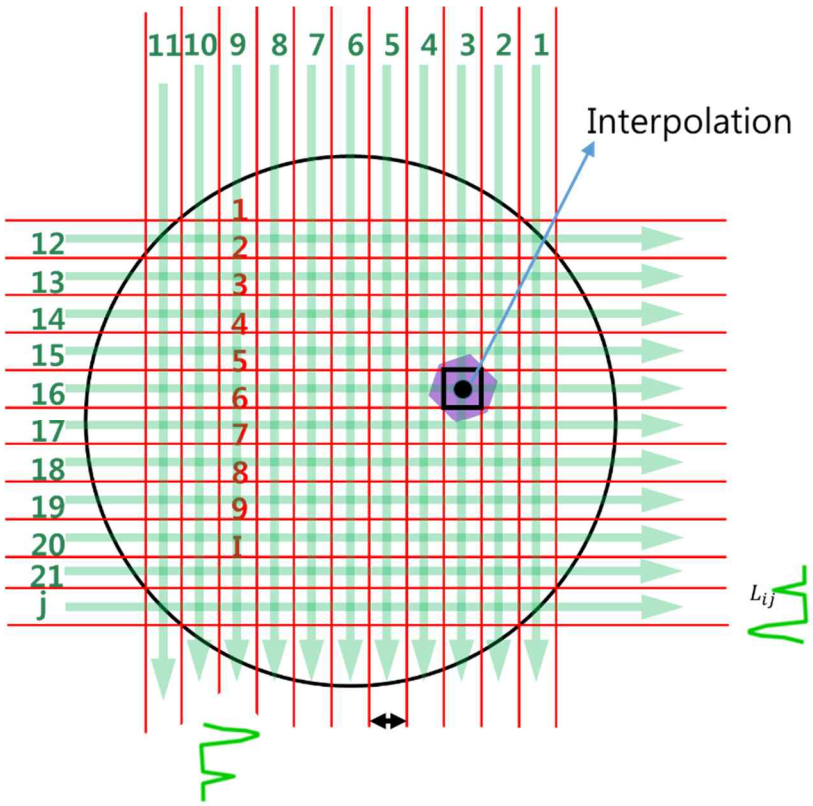

Fig. 4.2 Analysis grids and 22 beam paths

4.1.3 Performance evaluation of calculation

For the analysis using computed tomography, MART algorithm was used as the iterative calculation in this study. Absorption coefficient was iteratively calculated by CT analysis procedure shown in Fig. 2.9. An error was a difference of absorption acquired from calculation and phantom data. It was calculated from the following Eq. 4.4

$$Error = \sum_{j=1}^{J}\sum_{i=1}^{I}\left\{(A_{\lambda,i,j})_{cal} - (A_{\lambda,i.j})_{pha}\right\}^2 \tag{4.4}$$

Here, the subscript λ is wavelength, *i* is number of cell, *j* is number of laser.

Finally, the average temperature deviation was used to evaluate a result of reconstruction calculation. It is given in Eq. 4.5.

$$eT = \frac{\sum_{i=1}^{I}\left|T_{cal,i} - T_{pha,i}\right|}{I} \tag{4.5}$$

Here, *eT* is the average temperature deviation of the calculated temperature and virtual temperature, *I* is total number of cells. It need to quantify the temperature closeness for more objective comparison. The closeness is quantified by the following relative error equation.

$$ReT = \frac{1}{I}\sqrt{\sum_{i=1}^{I}\left(\frac{T_{cal,i} - T_{pha,i}}{T_{max} - T_{min}}\right)^2} \tag{4.6}$$

Here, T_{max} is maximum temperature at the virtual temperature distribution, T_{min} is minimum temperature at the virtual temperature distribution.

Fig. 4.3 shows the result of the average deviation of phantom and calculation temperature. Fig. 4.3 (a) is the result of the average temperature deviation using PLOS and MLOS methods at one Gaussian function of Fig. 4.2 (a). Fig. 4.3 (b) is the result of superimposed two Gaussian functions of Fig. 4.2 (b).

MLOS method was a little less the error rate than PLOS method. Thus, MLOS method was chosen as the calculation method for the estimate of initial value.

One-ratio method from two-wavelength (#1/#2 from #1, #2) means two-line thermometry method used commonly. As two-ratio method from three-wavelength (#1/2, #1/#3 from #1, #2, #3) means three-line thermometry, which this method is to average an acquired temperatures from two-ratio. Two-ratio method was less an error rate than one-ratio method and this means that the average temperature was calibrated more completely and stably.

Fig. 4.4 is the result of the reconstructed 2D temperature distribution calculated by using MART and MLOS. The boundary condition was set a room temperature (300 K). In Fig. 4.4 (a) the average temperature deviation (*eT)* calculated from Eq. 4.7 was a range of -2.7~64.9 K and the relative error was 0.0225. In Fig. 4.4 (b) the average temperature deviation was a range of -0.9~45.7 K and the relative error was 0.0189. In Fig. 4.4 (c) the average temperature deviation was a range of -24~45.9 K and the relative error was 0.02. In Fig. 4.4 (d) the average temperature deviation and the relative error were a range of -18~35.5 K and 0.019 at all grids.

Using two ratio of three-wavelength and MLOS methods with MART algorithm, the best CT-TDLAS method is theoretically demonstrated by these results. But a problem of this method remains still due to making a curve fitting using only peak points.

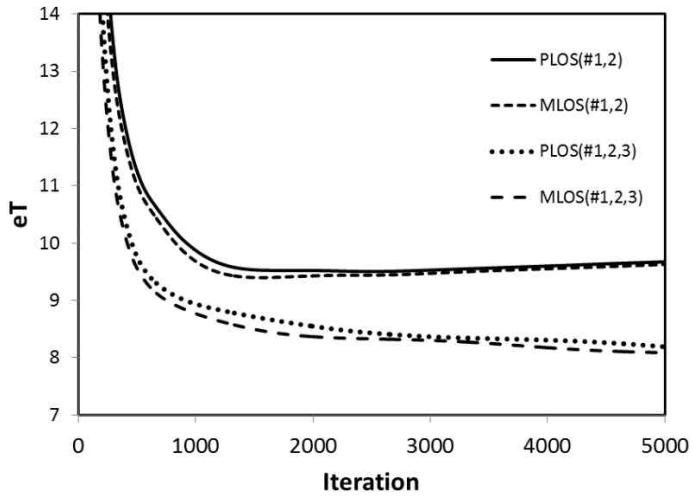

(a) The result of the average temperature deviation using PLOS and MLOS methods at one Gaussian function

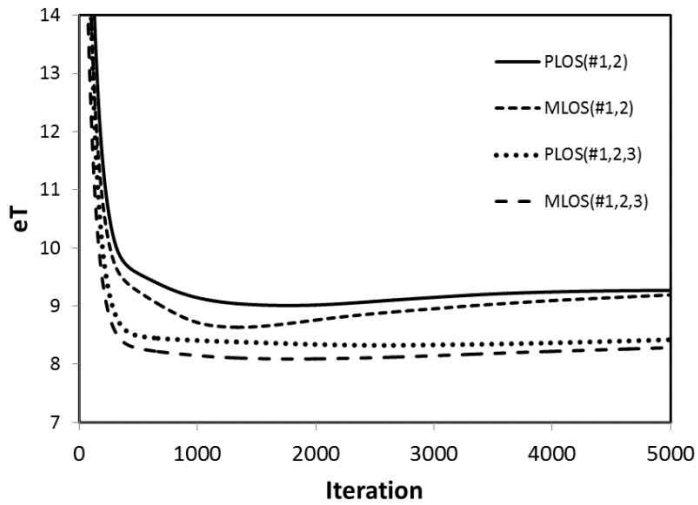

(b) The result of the temperature deviation using PLOS and MLOS methods at superimposed two Gaussian functions

Fig. 4.3 The average deviation with virtual and calculated temperature

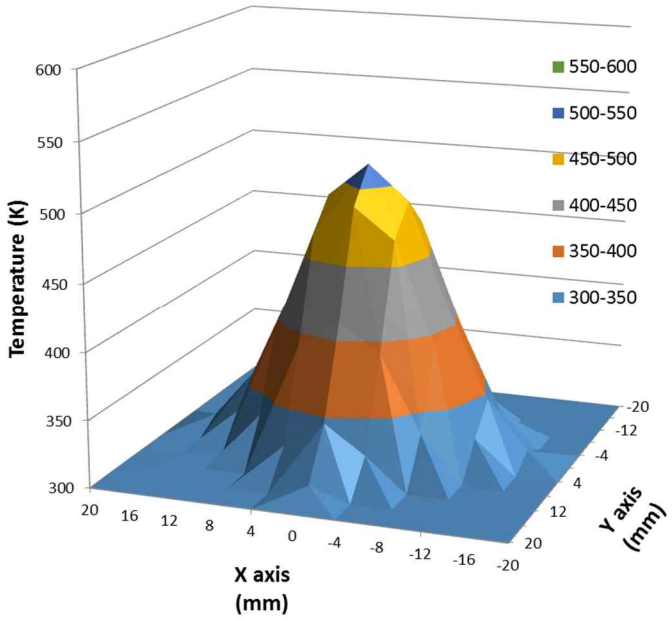

(a) The result of the temperature distribution by using one ratio of two-wavelength at one Gaussian function

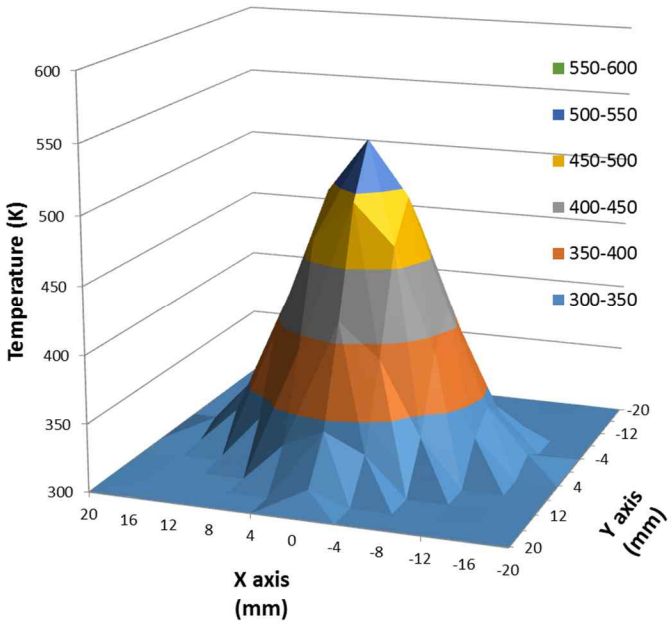

(b) The result of the temperature distribution by using two ratio of three-wavelength at one Gaussian function

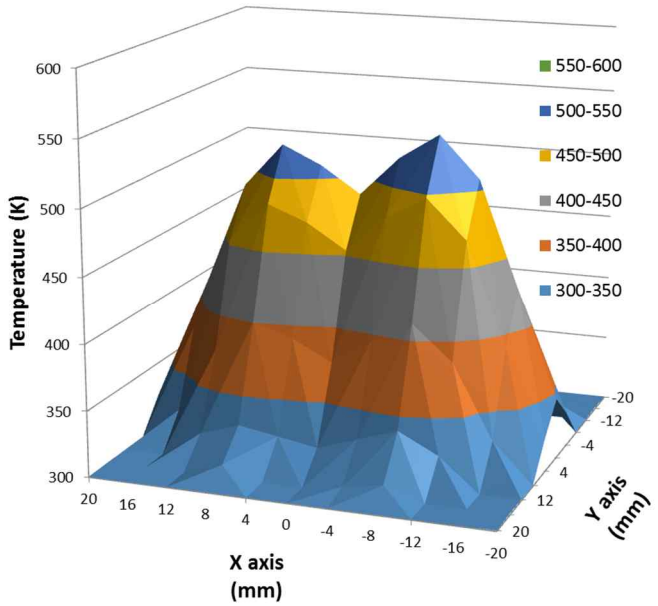

(c) The result of the temperature distribution by using one ratio of two-wavelength at superimposed two Gaussian functions

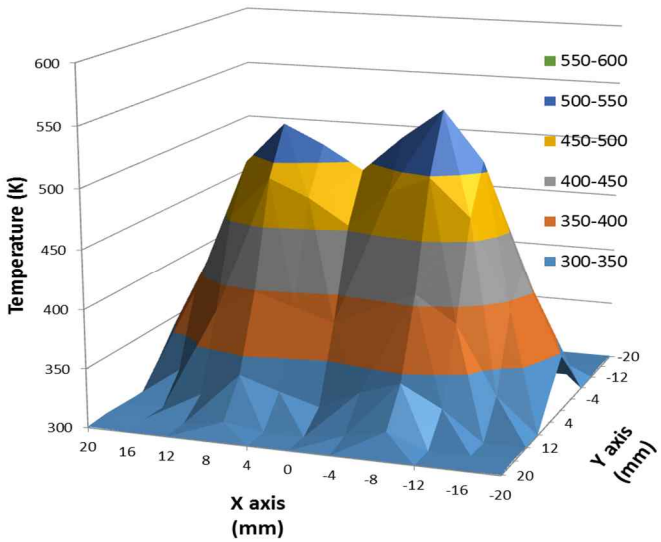

(d) The result of the temperature distribution by using two ratio of three-wavelength at superimposed two Gaussian functions

Fig. 4.4 The reconstructed 2D temperature distribution using MART and MLOS methods

4.1.4 Experimental setup

Fig. 4.5 shows the schematic experimental arrangement used in this study. Total 10 beams were installed on aluminum frame by arranging horizontal and vertical. A DFB laser (NTT Electronics Co., NLKE5GAAA), a semiconductor laser capable of fast and continuous wavelength scanning with a range of 0.6 nm, was used to measure water vapor absorption spectra at 1388 nm. A diameter of measuring space is 40 mm and the optics and detector are enclosed by purged N_2 to remove interfering absorption by ambient H_2O vapor in air along the optical path.

For comparison with the reconstructed temperature and measured temperature, temperature measurement was performed by a chromel-alumel thermocouple with a diameter of 100μm. The number of temperature measurement points is 576 (24×24).

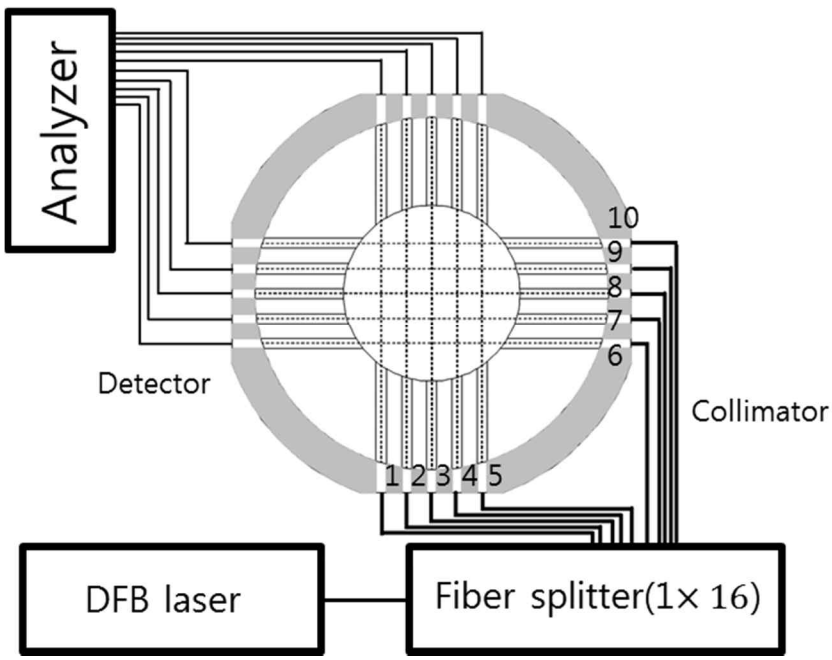

Fig. 4.5 The schematic experimental setup with 10 beams

4.1.5 Experiment results

Fig. 4.6 shows the result of 2D temperature measurement at the burner flame measured by thermocouple. Being a located burner at the center of measurement cell (X=0, Y=0), the temperature was measured with interval of 2 mm by moving the thermocouple along measurement space. It shows the highest temperature is over 1100 K and temperature becomes to room temperature at X=20 mm.

Fig. 4.7 shows the results of simultaneous measurement 10 path H_2O absorption spectra at the burner of the center position. Transforming of the beam signal, a polynomial noise reduction technique [10-11] was used to reduce noises such as the effect of beam steering in all lasers.

The laser path 1, 5, 6 and 10 pass through the low temperature region and the laser path 2, 4, 7 and 9 pass through middle temperature region and laser path 3 and 8 pass through the high temperature region.

As shown at Fig. 2.7(e), the intensities of absorption line #1 have strong temperature dependence but those of #2 and #3 are not strong. The ratios (#1/#2) were high at laser paths 3 and 8 (high temperature region) and the ratios at laser path 2, 4, 7 and 9 (middle temperature region) were smaller than those of high temperature region (laser paths 3 and 8).

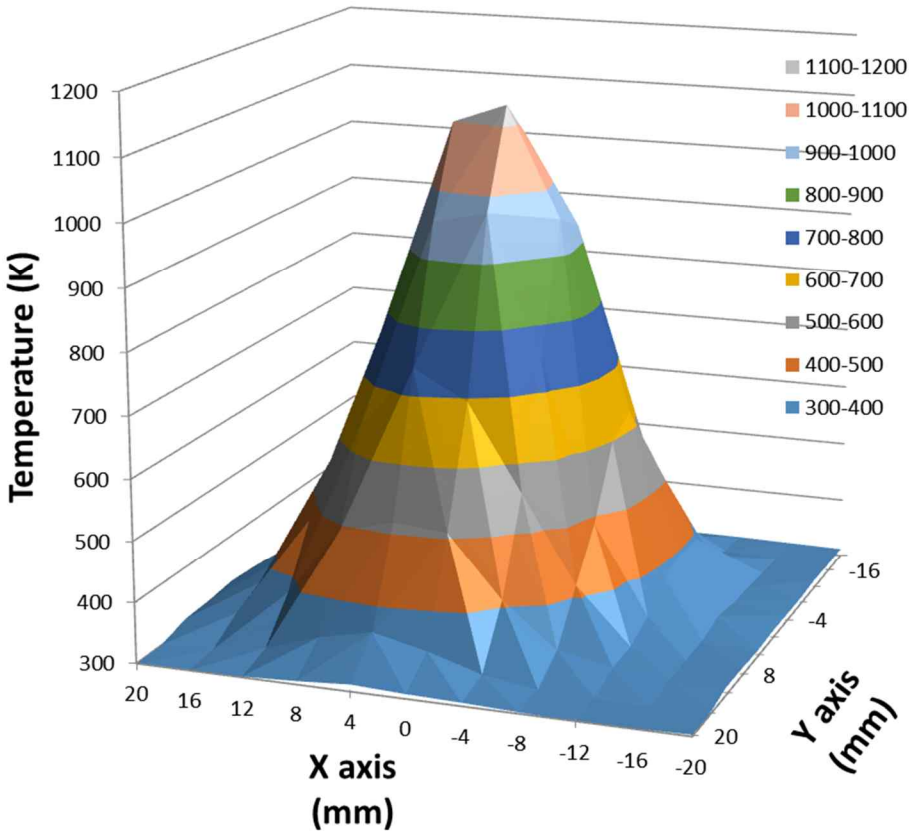

Fig. 4.6 2D temperature distribution measured by thermocouple

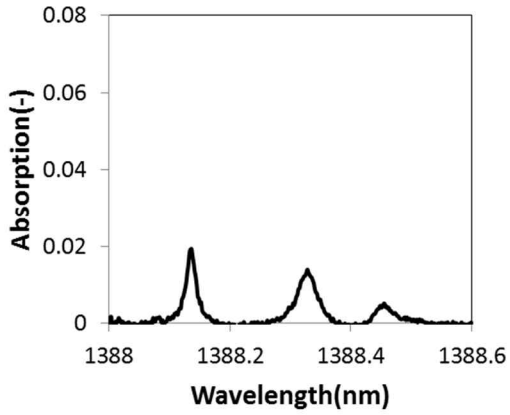

(a) Laser path 1

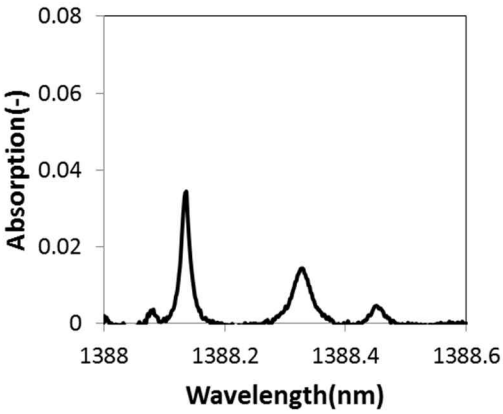

(b) Laser path 2

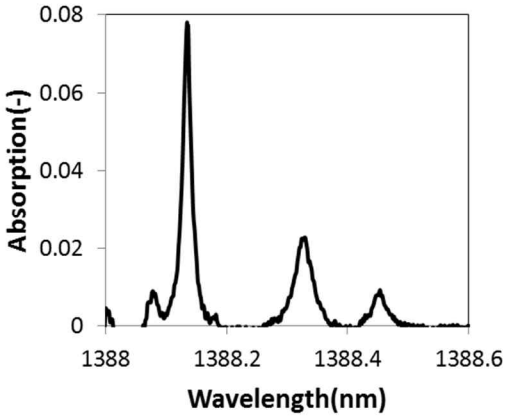

(c) Laser path 3

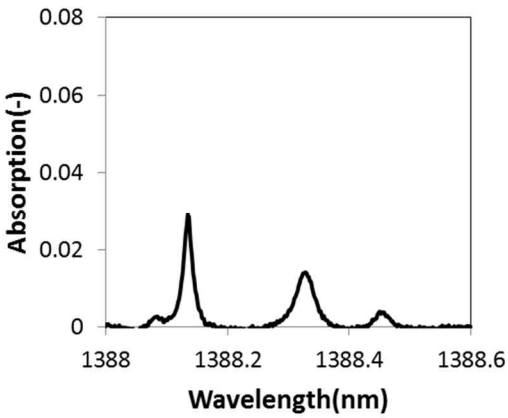

(d) Laser path 4

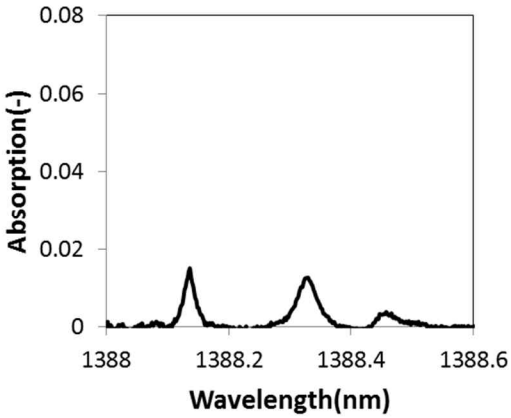

(e) Laser path 5

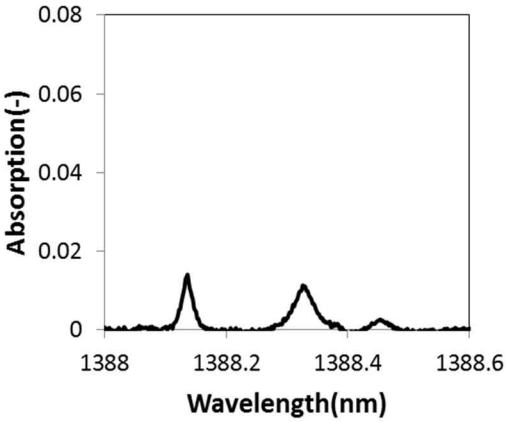

(f) Laser path 6

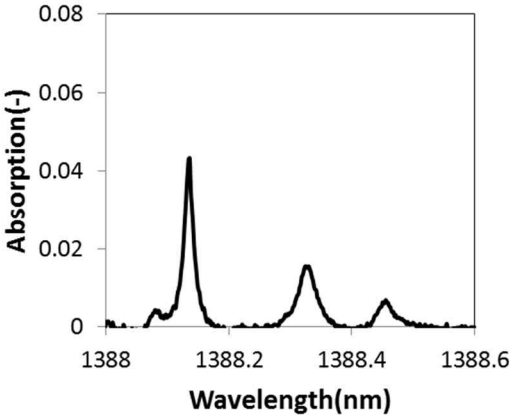

(g) Laser path 7

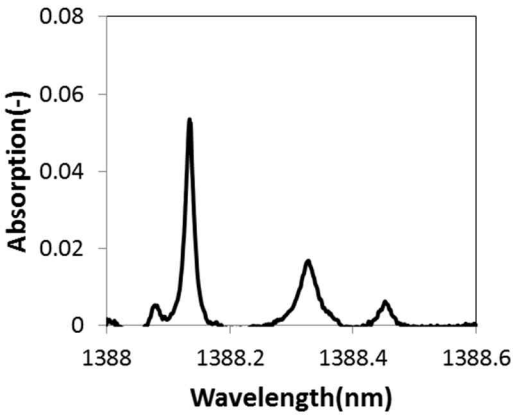

(h) Laser path 8

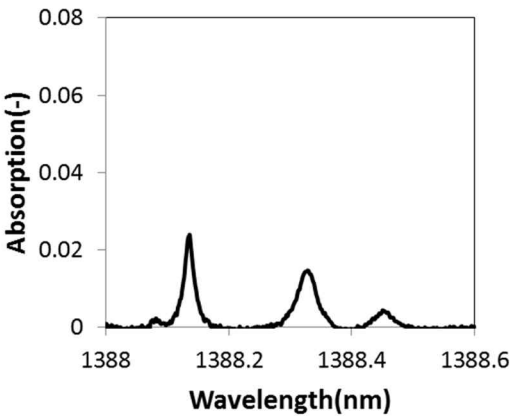

(i) Laser path 9

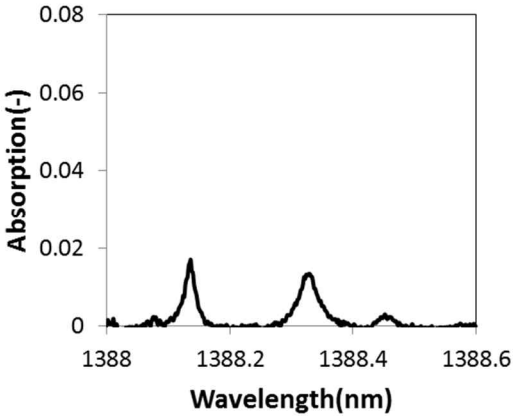

(j) Laser path 10

Fig. 4.7 The absorption graphs of H_2O spectra with 10 path lasers

4.1.6 Simulation results

Fig. 4.8 shows the results of the average temperature deviation simulated from the burner experiment. one-ratio method from two-wavelength (#1/#2) and two-ratio method from three-wavelength (#1/#2, #1/#3) were calculated and compared with each other. In a same way virtual data simulated, a result of error rate of two-ratio method was shown less than that of one-ratio method. A performance of two-ratio method used with MART and MLOS is also experimentally demonstrated.

Fig. 4.9 shows the reconstructed 2D temperature distribution by using MART and MLOS algorithms from experiment data. The average deviation of the calculated and measured temperature calculated from Eq. 4.7. In Fig. 4.4 (a) the average temperature deviation and the relative error were a range of -191~417 K and 0.107. In Fig. 4.4 (b) the average temperature deviation and the relative error were a range of -185~161 K and 0.098 at all grids. But the ratio-thermometry method has an unstable calculation fields if Gaussian filter is not used.

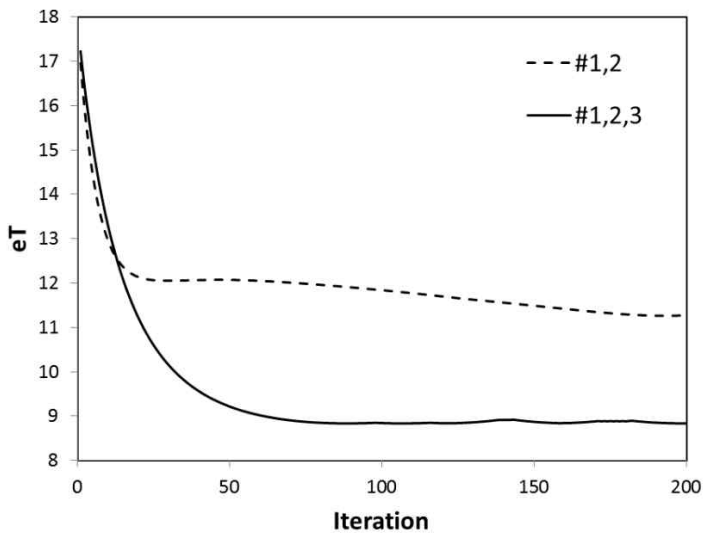

Fig. 4.8 The comparison of the average temperature deviation of one ratio and two ratio method using data of burner experiment

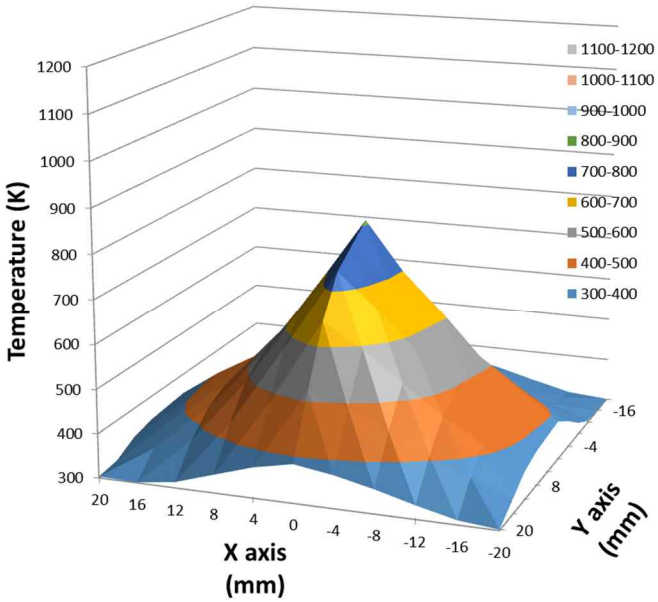

(a) 2D temperature distribution simulated by using one ratio of two-wavelength

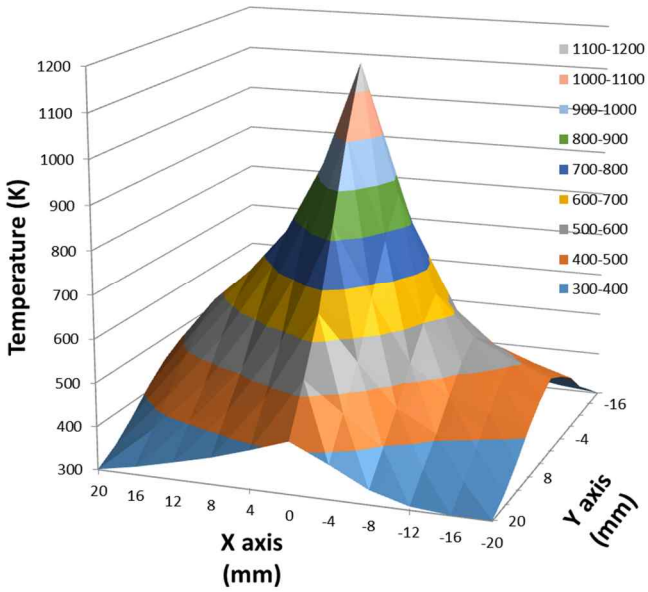

(b) 2D temperature distribution simulated by using two ratio of three-wavelength

Fig. 4.9 The reconstructed 2D temperature distribution calculated using MART and MLOS methods from the experiment data

4.2 Full-Profile Cross-Correlation Algorithm

Most of algorithms for the reconstruction of temperature distribution in CT-TDLAS are based on two or three-line thermometry method. These algorithms utilize only the peak intensity information of representative wavelengths at 1388.135 nm and 1388.326 nm for the case of H_2O vapor. So, this method gives an unstable calculation convergence due to signal noise, bias error, and signal mismatches. In this study, it is proposed a new reconstruction algorithm based on cross-correlation at all wavelengths for temperature calculation.

4.2.1 Normalized Cross Correlation

In signal processing, cross-correlation is a measure of similarity of two series as a function of the lag of one relative to the other. This is typically done at every step by subtracting the mean and dividing by the standard deviation. That is, the cross-correlation of a template, *t(x, y)* with a subimage *f(x, y)* is written as following equation.

$$\frac{1}{n}\sum_{x,y}\frac{(f(x,y)-\overline{f})\cdot(t(x,y)-\bar{t})}{\sigma_f\sigma_t} \tag{4.7}$$

Here, *n* is the number of pixels in *t(x, y)* and *f(x, y)*, $\bar{t}$ is the average of *f* and $\bar{f}$ is the standard deviation of *f*. In functional analysis terms, this can be thought of as the dot product of two normalized vectors. The upper equation is modified as following equation in this study.

Fig. 4.10 shows the calculation process of the template matching method. According to progressing of calculation iteratively, the templated matching is completed. Fig. 4.11 shows the configuration of pattern change in accordance with temperature change. This data is utilized to be a criterion of temperature template matching.

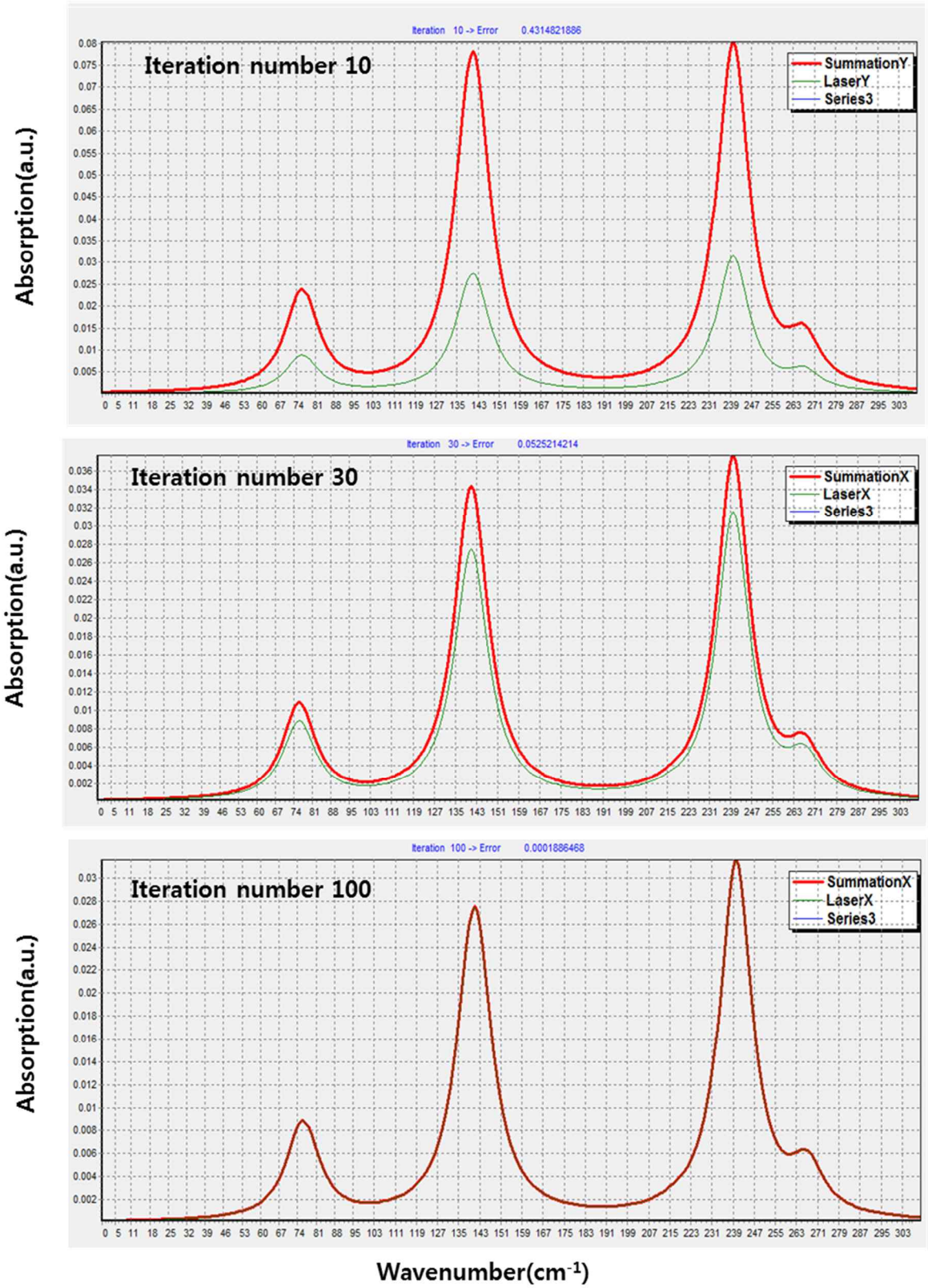

Fig. 4.10 Calculation process of the template matching method

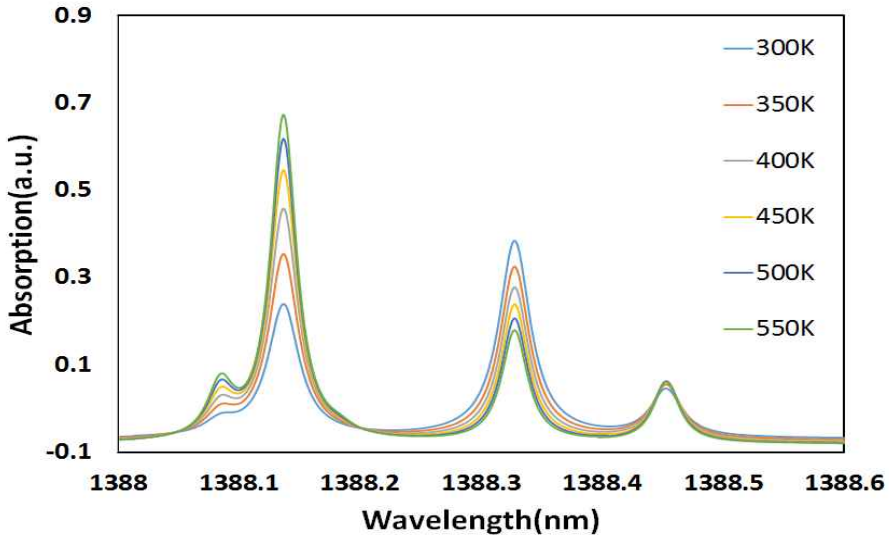

(a) Pattern changes at region of low temperature

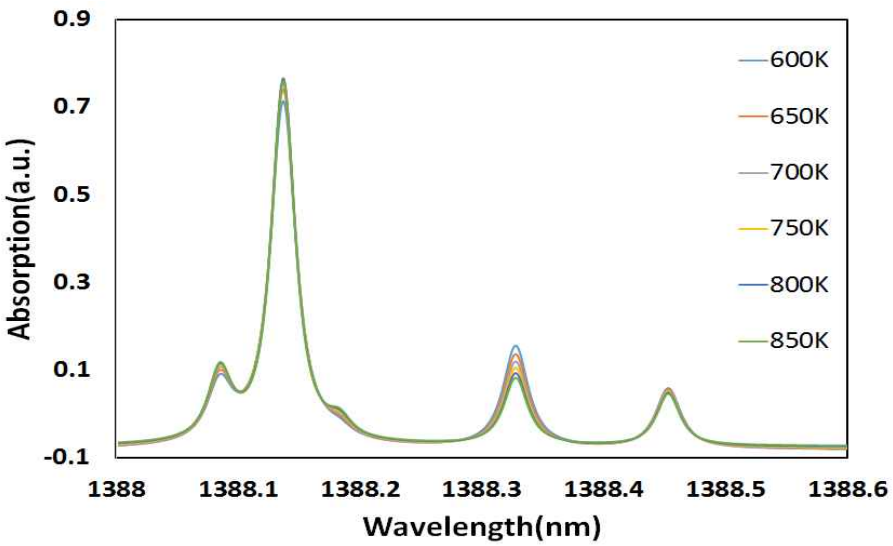

(b) Pattern changes at region of high temperature

Fig. 4.11 The configuration of pattern change in accordance with temperature change

4.2.2 Making phantoms data

For evaluating the performance of algorithm, the virtual temperature distribution was made by using Gaussian distribution by Eq. 4.1. The information of parameter used Gaussian function summarized in Table 4.2.

Fig. 4.12 shows the phantom for 2D temperature distribution. Maximum temperature was set into 600 K. By using the virtual temperature distribution and Eq. 4.3, the absorption spectra were made from the virtual lasers. $L_{i,j}$ (length of unit cell) is 4 mm in this study.

Table 4.3 is information of selected spectra lines of H_2O at reference temperature from HITRAN2008 database [34]. By using 40 spectra, the pattern matching was made in the range of all absorption wavelengths.

Fig. 4.13 and Fig. 4.14 are the virtual absorption spectra of horizontal and vertical lasers of H_2O spectra at 1338.0 ~ 1338.6 nm from the virtual lasers. These graphs were made by a sum of absorptions at each cells passing a line of sight.

Table 4.2 Information of parameters used for Gaussian function

Fig.4.1(a)	X_0	Y_0	Deviation of temperature (D)	Sigma (σ)
Vortex 1	0	0	300	8.0

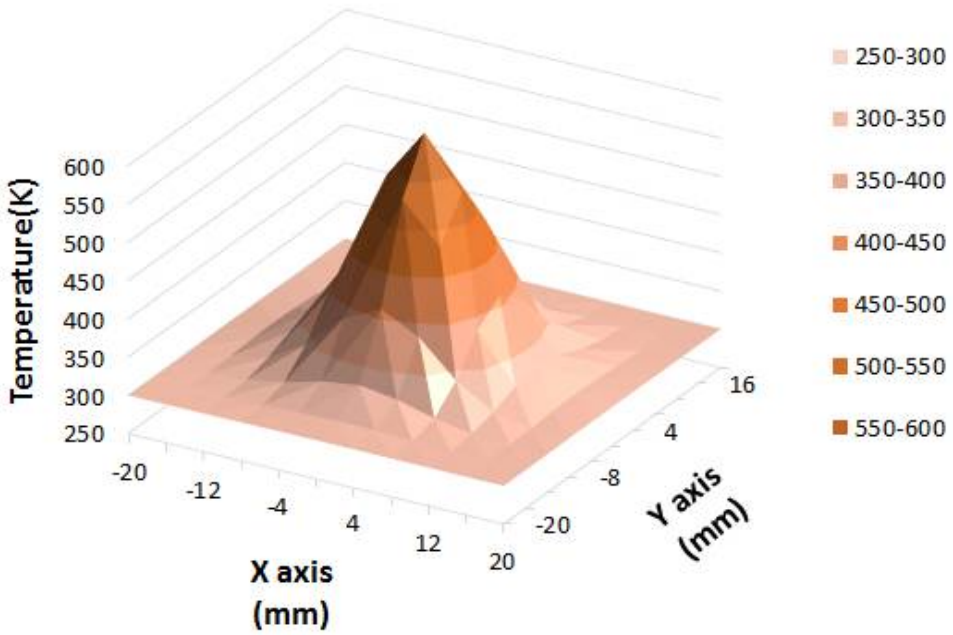

Fig. 4.12 Phantom for 2D temperature distribution

Table 4.3 Information of spectra lines of H_2O at reference temperature

Frequency [cm^{-1}]	Wavelength [nm]	Line- strength [$cm^{-1} \cdot atm^{-1}$]	E″ [cm^{-1}]
7202.037	1388.496	9.18×10^{-10}	3224.546
7202.060	1388.492	2.74×10^{-10}	2495.166
7202.087	1388.486	3.56×10^{-4}	136.1639
7202.256	1388.454	2.74×10^{-2}	446.5107
7202.327	1388.440	3.76×10^{-5}	488.1077
7202.448	1388.417	4.08×10^{-10}	3135.764
7202.494	1388.408	9.78×10^{-10}	2670.79
7202.583	1388.391	3.04×10^{-6}	1201.921
7202.700	1388.368	1.64×10^{-7}	1411.642
7202.722	1388.364	5.75×10^{-8}	1817.451
7202.805	1388.348	1.07×10^{-9}	3870.224
7202.909	1388.328	1.15×10^{-1}	70.0908
7202.911	1388.328	5.27×10^{-10}	3216.193
7202.999	1388.311	1.68×10^{-6}	1819.335
7203.037	1388.303	2.25×10^{-9}	2586.529
7203.239	1388.264	8.58×10^{-8}	2630.192
7203.265	1388.259	3.78×10^{-8}	2053.969
7203.376	1388.238	1.74×10^{-9}	3736.171
7203.450	1388.224	5.40×10^{-8}	2552.857
7203.479	1388.218	5.30×10^{-10}	2490.354
7203.635	1388.188	3.26×10^{-8}	446.6966
7203.658	1388.184	1.58×10^{-4}	1742.306
7203.763	1388.163	1.18×10^{-7}	1131.776
7203.784	1388.159	8.38×10^{-6}	2000.863
7203.822	1388.152	3.48×10^{-5}	446.5107
7203.824	1388.152	3.91×10^{-10}	4016.115
7203.890	1388.139	5.65×10^{-2}	742.0762
7203.894	1388.138	1.88×10^{-2}	742.073
7203.935	1388.130	4.53×10^{-4}	285.4186
7203.950	1388.127	1.77×10^{-6}	1050.158
7203.968	1388.124	9.65×10^{-7}	2042.31
7204.030	1388.112	1.20×10^{-4}	1640.506
7204.053	1388.107	1.65×10^{-9}	3299.991
7204.069	1388.104	4.83×10^{-9}	1474.98
7204.135	1388.092	1.70×10^{-5}	1772.414
7204.166	1388.086	7.89×10^{-3}	931.237
7204.232	1388.073	2.86×10^{-9}	3058.398
7204.353	1388.050	4.63×10^{-7}	2439.954
7204.426	1388.036	1.21×10^{-8}	2248.063
7204.546	1388.013	3.36×10^{-8}	1525.135

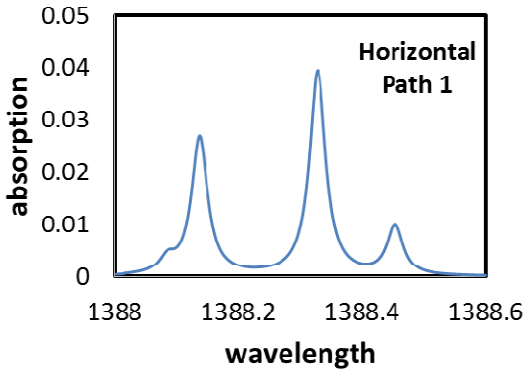
Horizontal
Path 1
absorption
0.05
0.04
0.03
0.02
0.01
0
1388
1388.2
1388.4
1388.6
wavelength

(a)

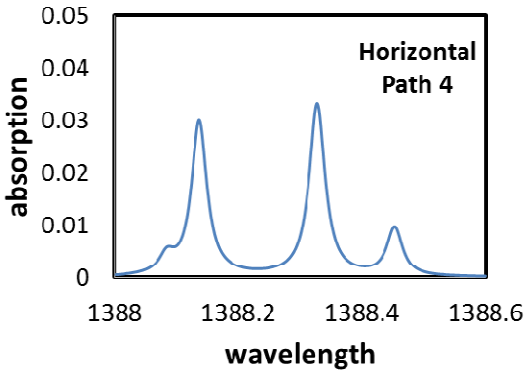
Horizontal
Path 4
absorption
0.05
0.04
0.03
0.02
0.01
0
1388
1388.2
1388.4
1388.6
wavelength

(d)

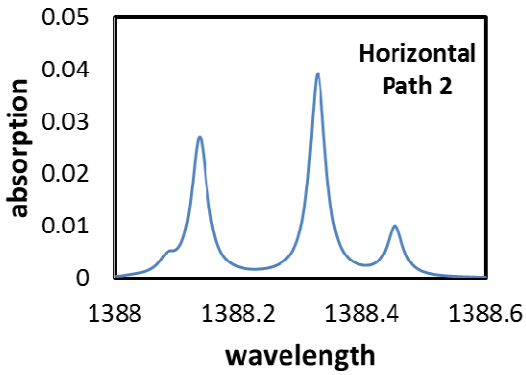
Horizontal
Path 2
absorption
0.05
0.04
0.03
0.02
0.01
0
1388
1388.2
1388.4
1388.6
wavelength

(b)

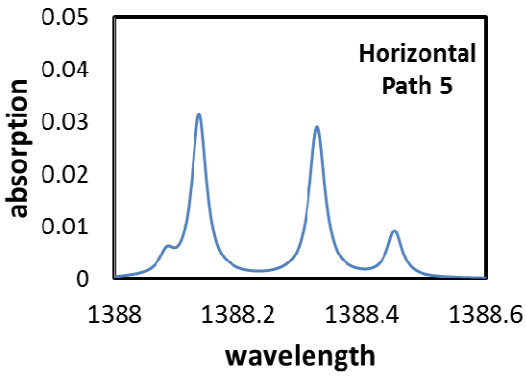
Horizontal
Path 5
absorption
0.05
0.04
0.03
0.02
0.01
0
1388
1388.2
1388.4
1388.6
wavelength

(e)

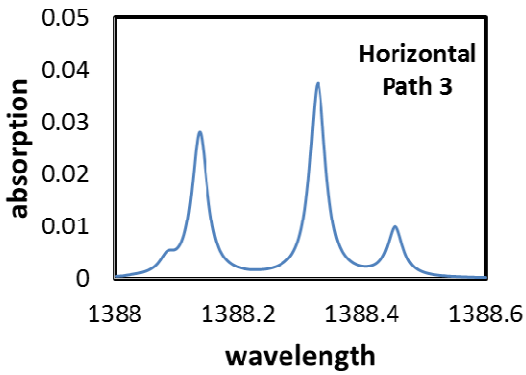
Horizontal
Path 3
absorption
0.05
0.04
0.03
0.02
0.01
0
1388
1388.2
1388.4
1388.6
wavelength

(c)

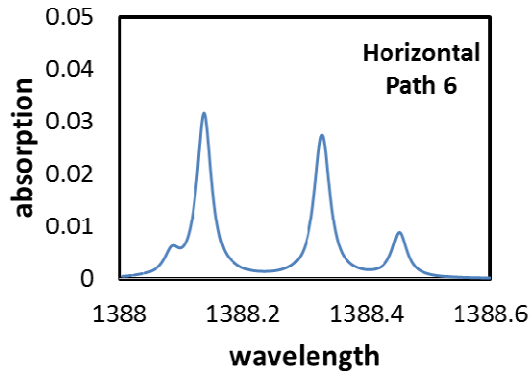
Horizontal
Path 6
absorption
0.05
0.04
0.03
0.02
0.01
0
1388
1388.2
1388.4
1388.6
wavelength

(f)

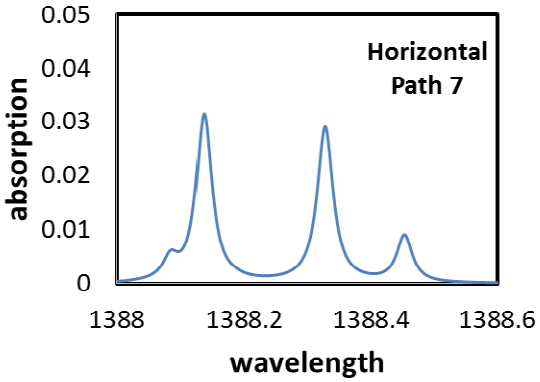

(g)

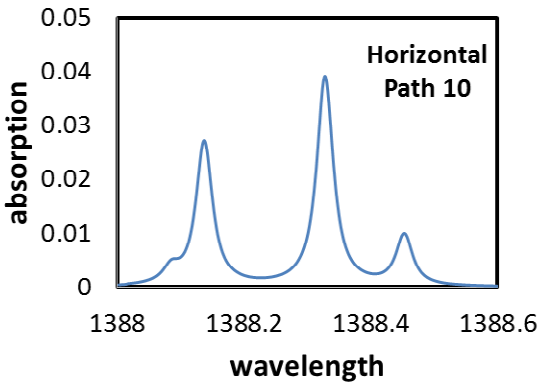

(j)

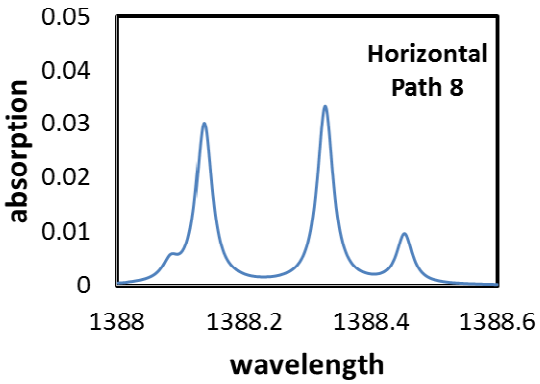

(h)

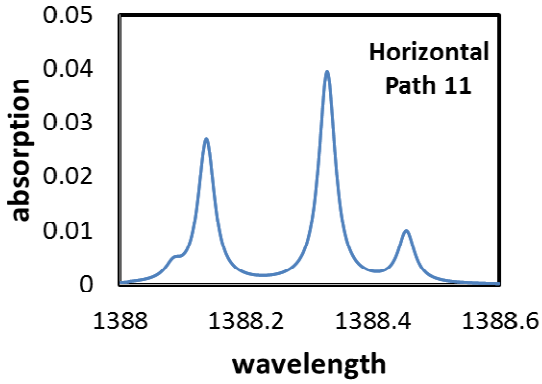

(k)

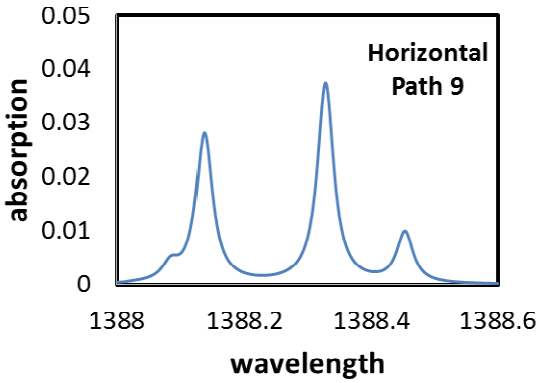

(i)

Fig. 4.13 The virtual H_2O absorption spectra of horizontal lasers at 1338.0 nm ~ 1338.6 nm

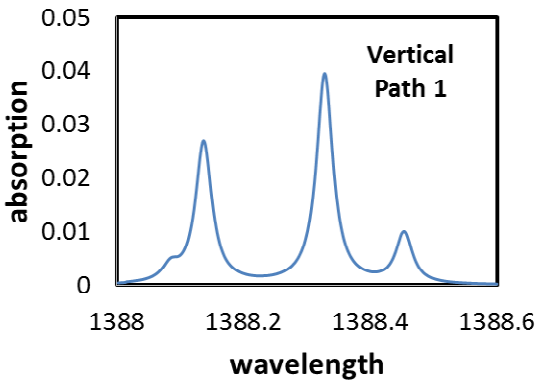
0.05
0.04
0.03
0.02
0.01
0
absorption
Vertical
Path 1
1388
1388.2
1388.4
1388.6
wavelength

(a)

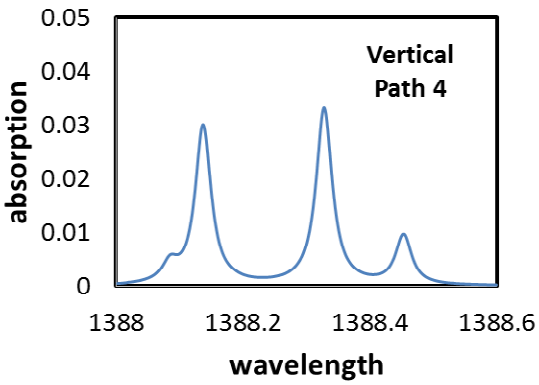
0.05
0.04
0.03
0.02
0.01
0
absorption
Vertical
Path 4
1388
1388.2
1388.4
1388.6
wavelength

(d)

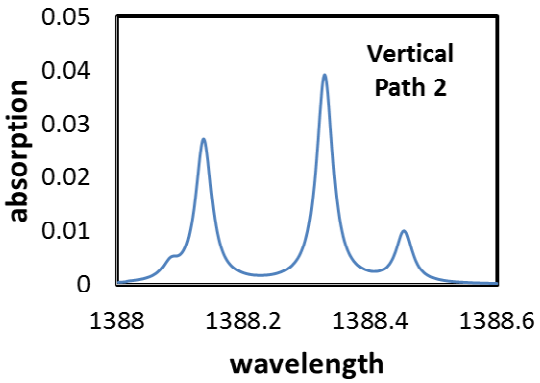
0.05
0.04
0.03
0.02
0.01
0
absorption
Vertical
Path 2
1388
1388.2
1388.4
1388.6
wavelength

(b)

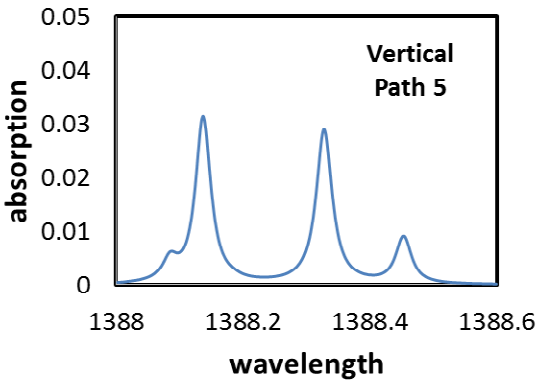
0.05
0.04
0.03
0.02
0.01
0
absorption
Vertical
Path 5
1388
1388.2
1388.4
1388.6
wavelength

(e)

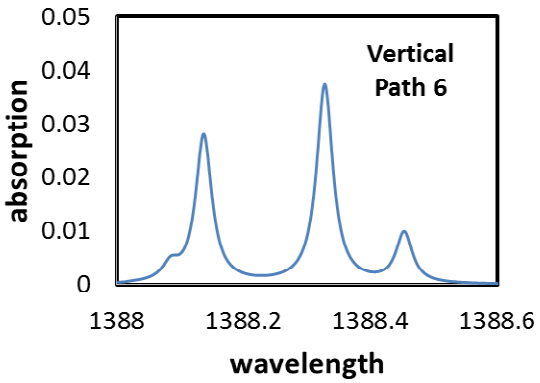
0.05
0.04
0.03
0.02
0.01
0
absorption
Vertical
Path 6
1388
1388.2
1388.4
1388.6
wavelength

(c)

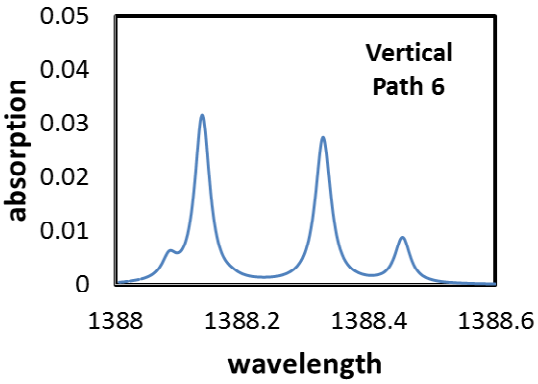
0.05
0.04
0.03
0.02
0.01
0
absorption
Vertical
Path 6
1388
1388.2
1388.4
1388.6
wavelength

(f)

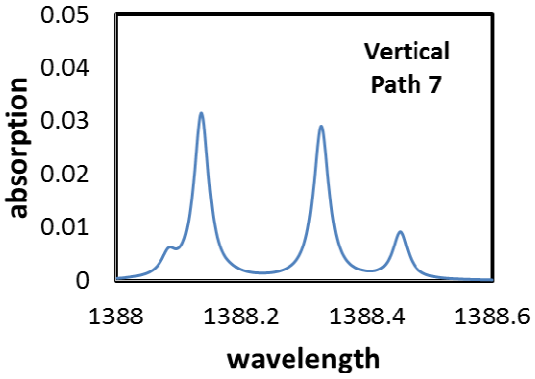

(g)

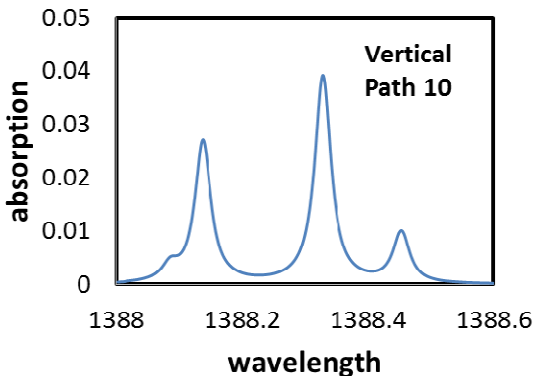

(j)

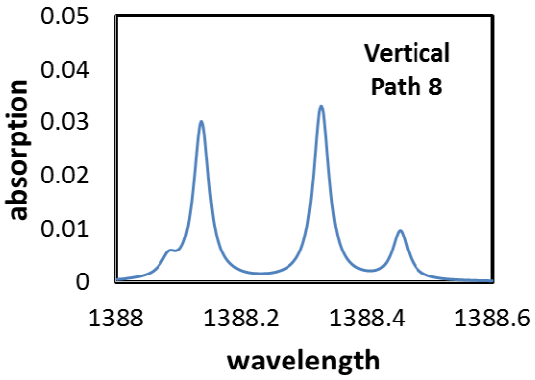

(h)

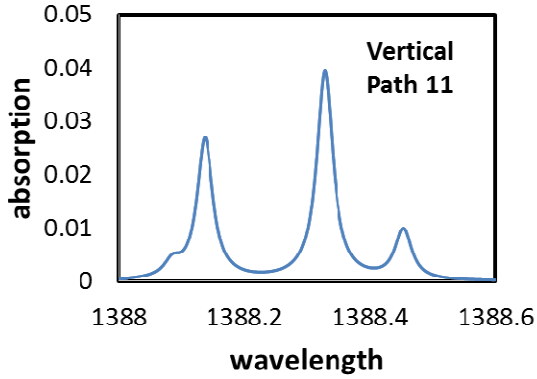

(k)

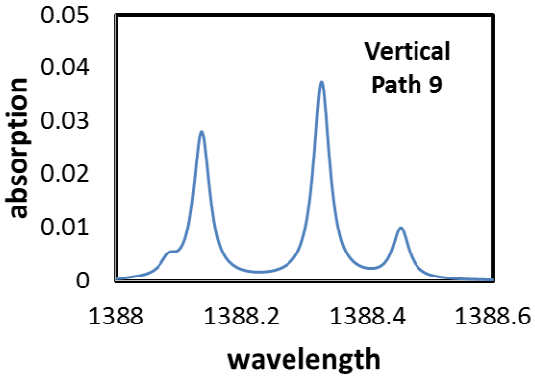

(i)

Fig. 4.14 The virtual H_2O absorption spectra of vertical lasers at 1338.0 nm ~ 1338.6 nm

4.2.3 Template matching method

In this chapter, it was elaborated on template matching algorithm renewed from Eq. 4.1

Eq. 4.7 is the template matching algorithm using absorption spectra.

$$C_{\alpha,t} = \frac{\sum_{i=1}^{n}(\alpha_i - \overline{\alpha_i})(t_i - \overline{t_i})}{\sqrt{\sum_{i=1}^{n}(\alpha_i - \overline{\alpha_i})^2 \sum_{i=1}^{n}(t_i - \overline{t_i})^2}} \quad (4.7)$$

Here, subscript *i* is wavelength which is 340 equal divisions in the range of 1388.0 nm ~1388.6 nm, α is the calculated absorption coefficient, t is the theoretical absorption coefficient, not included *n* (number density). *C* is the cross correlation coefficient. In case a completely same pattern, *C* becomes 1. If it is completely opposite, *C* becomes -1. Maximum value *C* is chosen by making the template matching with a given temperature patterns. The correlation coefficient of temperature was made as an interval of 5 K and the curve fitting was proceeded as a pattern that most closely matches.

An error whether or not convergence is decided by Eq. 4.4 and the convergence calculation is until an error is less than 10^{-20}. If convergence condition is not matched, $\boldsymbol{\alpha}_{C_{\alpha,t}}$ (new absorption coefficient) is calculated by using a new temperature acquired from template matching. A difference between a new absorption coefficient and a previous absorption coefficient becomes an error through template matching. This error is imposed as much as 10% to modify the previous absorption coefficient. Also, the modified absorption coefficient is iteratively calculated by using MART algorithm. Fig. 4.15 shows a flow chart of pattern matching algorithm.

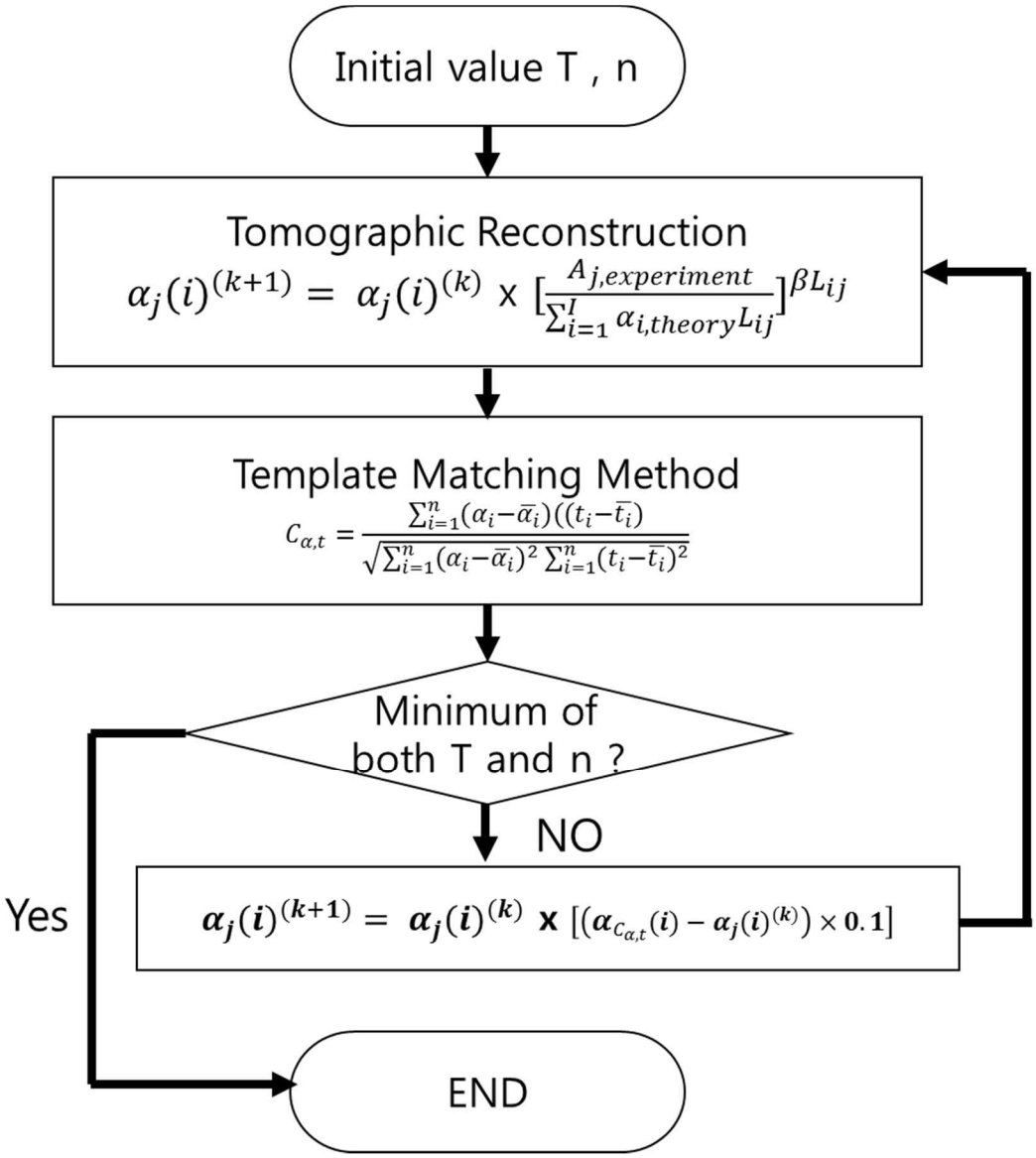

Fig. 4.15 Flow chart of pattern matching algorithm

4.2.4 Simulation results

Fig. 4.16 show the result of the reconstructed temperature distribution. At the center position the temperature was 450 K, the boundary temperature was 275 K. The result of the average temperature deviation and the relative error were 25 ~ 150 K and 0.078. Because the used wavelengths was referred too much than needs during the curve fitting, the temperature seemed not to be matched at the center region. But Full-Profile Cross-Correlation method was able to conduct a more stable calculation than two or three thermometry methods.

In this chapter, it was described about the development of Full-Profile Cross-Correlation method. The theoretical simulation was obviously performed and the result of temperature error was a little big at the center. Therefore, a procedure of experimental verification was omitted. At the next chapter, it will be introduced a newly enhanced method based on cross correlation method.

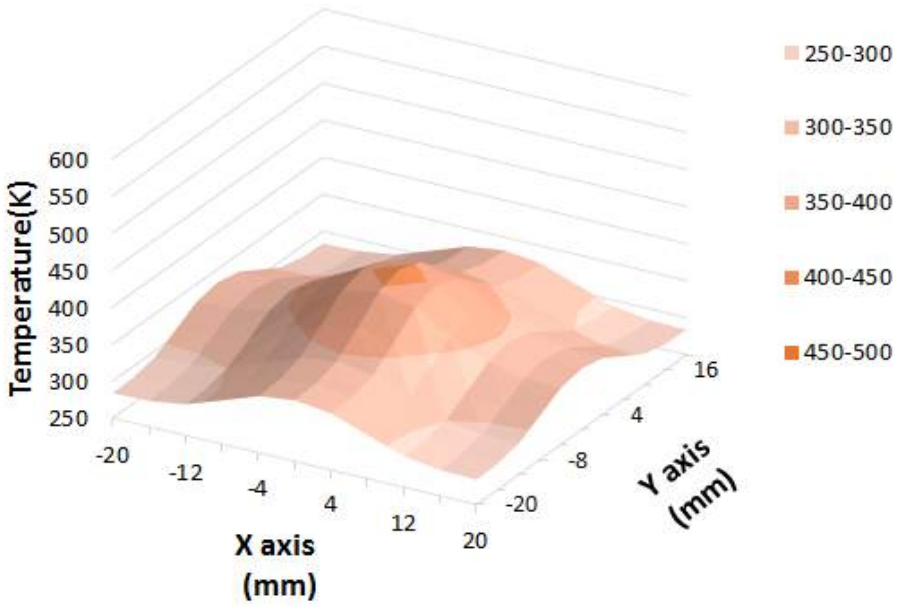

Fig. 4.16 The reconstructed temperature distribution

4.3 6-Line-Profiles Fitting Algorithm

As mentioned earlier, Full-Profile Cross-Correlation method was restricted when it was given an information of overloaded wavelengths. But 6-Line-Profiles Fitting Algorithm method is to fit as LMS (Least Mean Squares) using 6 wavelengths instead of a template matching method.

4.3.1 Concept of 6-Line-Profiles Fitting Algorithm

A fundamental concept is to fit by using n (number density) and α (absorption coefficient) from Eq. 4.3. Changing simultaneously n and T in each of cells, the calculated absorption coefficient and the data of temperature table made from Fig. 4.11 are fitted into an optimization scale. n and T are changed consistently by LMS and the convergence condition is until an error is less than 10^{-20}. If it isn't, $\boldsymbol{\alpha}_L$(a new absorption coefficient) is recalculated by using a new temperature acquired from LMS fitting. Fig. 4.17 shows a flow chart of 6-Line-Profiles Algorithm.

Table 4.4 Information of the selected 6 lines

Frequency [cm^{-1}]	Wavelength [nm]	Line- Strength [$cm^{-1} \cdot atm^{-1}$]	E″ [cm^{-1}]
7202.255	1388.453	2.73×10^{-2}	446.51
7202.909	1388.326	1.15×10^{-1}	70.09
7203.658	1388.183	1.59×10^{-4}	1742.30
7203.903	1388.136	1.88×10^{-2}	742.08
7203.906	1388.135	5.65×10^{-2}	742.07
7204.166	1388.085	7.88×10^{-3}	931.24

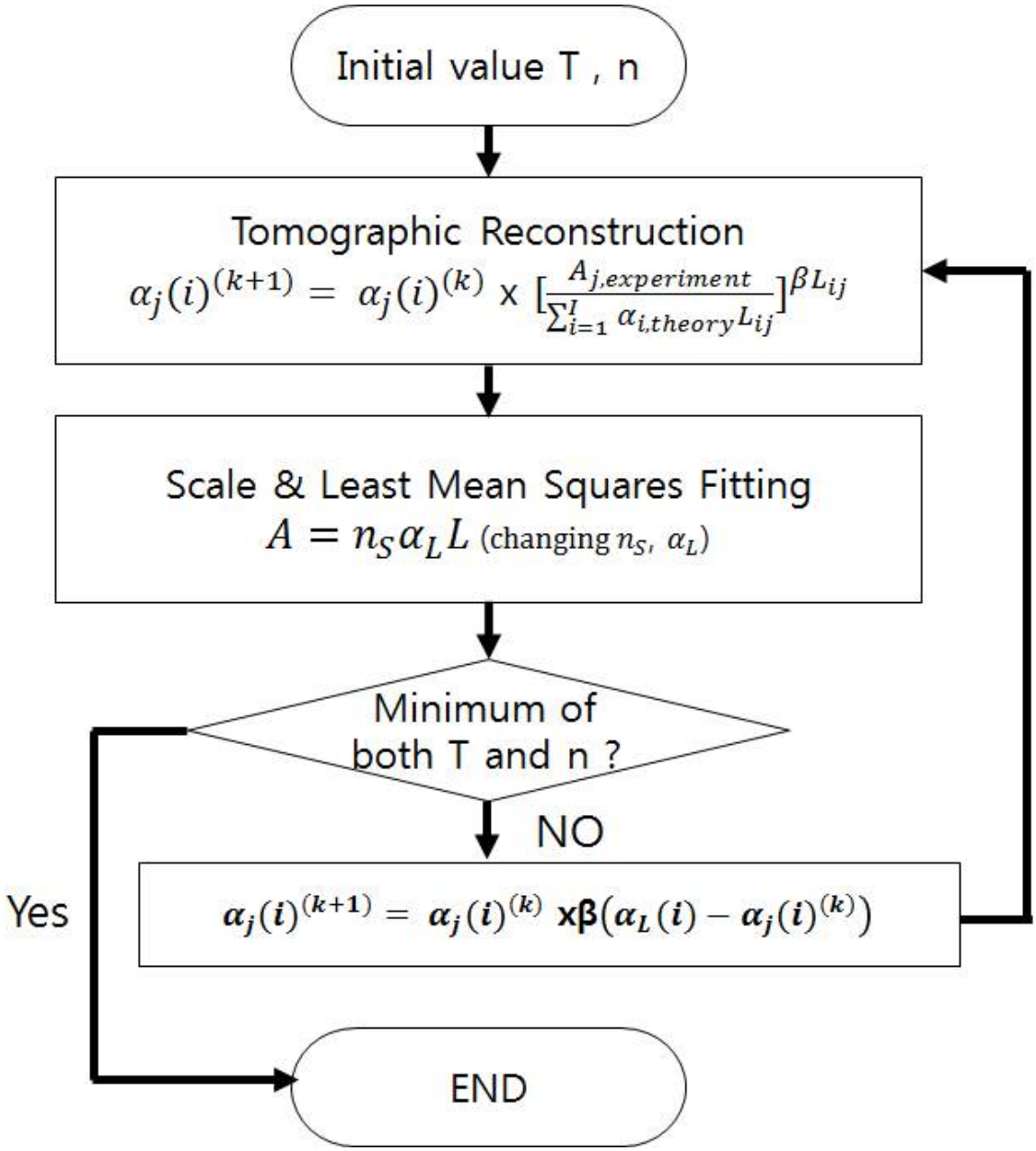

Fig. 4.17 Flow chart of 6line profiles algorithm

4.3.2 Making phantoms for 2D temperature and concentration distributions

Virtual temperature distribution was made by using Gaussian distribution by Eq. 4.1. Fig. 4.18 and Fig. 4.19 are the phantoms for 2D temperature and H_2O number density distributions. In Fig. 4.18 a maximum temperature is 600 K and a maximum H_2O number density is 0.16 at the center. In Fig. 4.19, a maximum temperature is 1000 K and a maximum H_2O number density is 0.24 at the center. In both pictures a minimum temperature is 300 K and a minimum H_2O number density 0.02 at the edgy. The information of parameters used for Gaussian function show in Table 4.5.

Table 4.5 Information of parameters used for Gaussian function

Fig 4.18	**X_0**	**Y_0**	**Deviation (D)**	**Sigma (σ)**
Temperature	0	0	300	8.0
Number density	0	0	0.14	8.0
Fig 4.19	**X_0**	**Y_0**	**Deviation (D)**	**Sigma (σ)**
Temperature	0	0	700	8.0
Number density	0	0	0.22	8.0

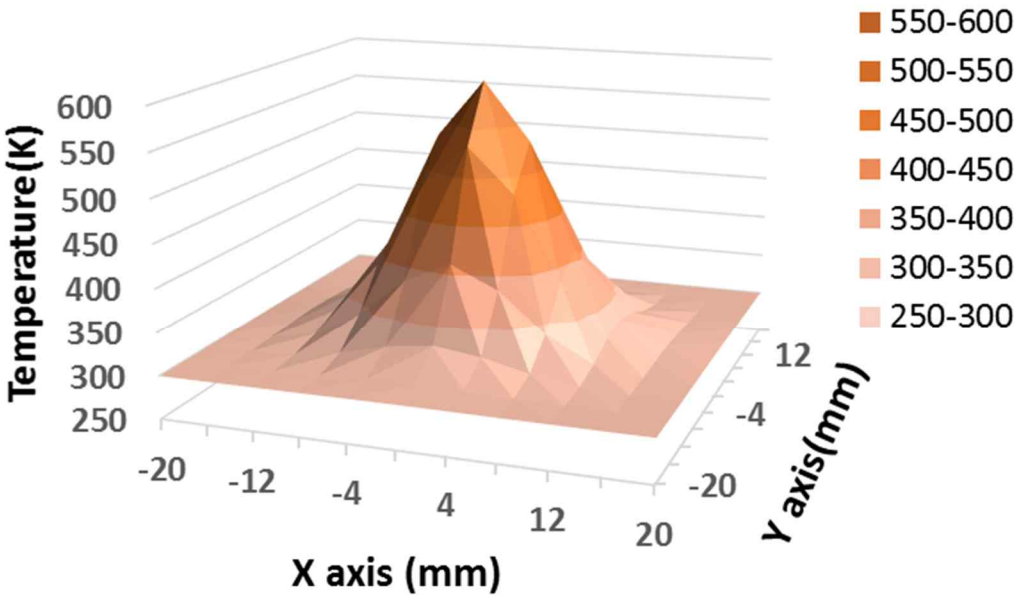

(a) 2D temperature distribution

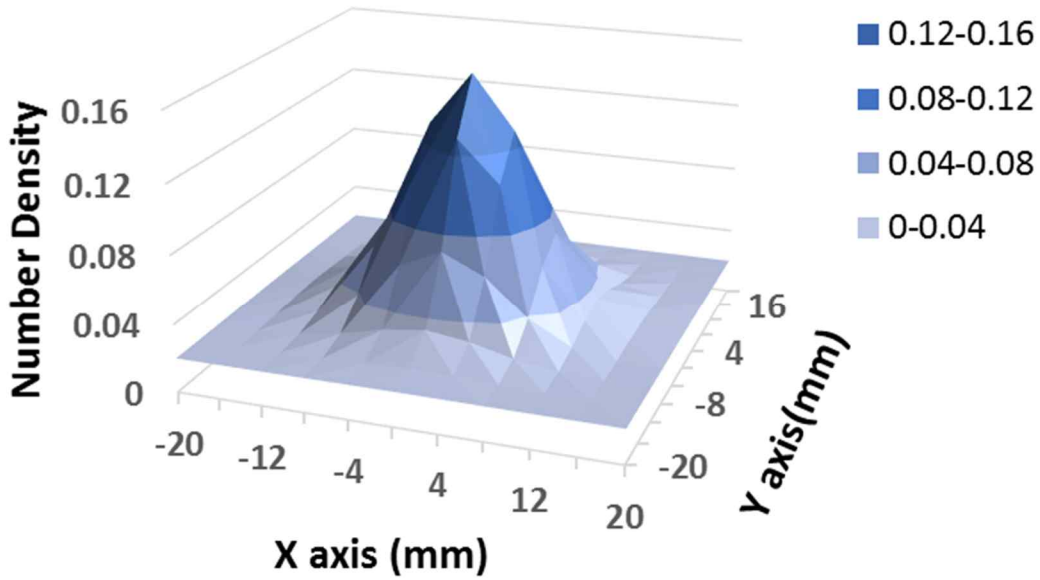

(b) 2D H_2O number density distribution

Fig. 4.18 Phantoms for 2D temperature and H_2O number density distributions

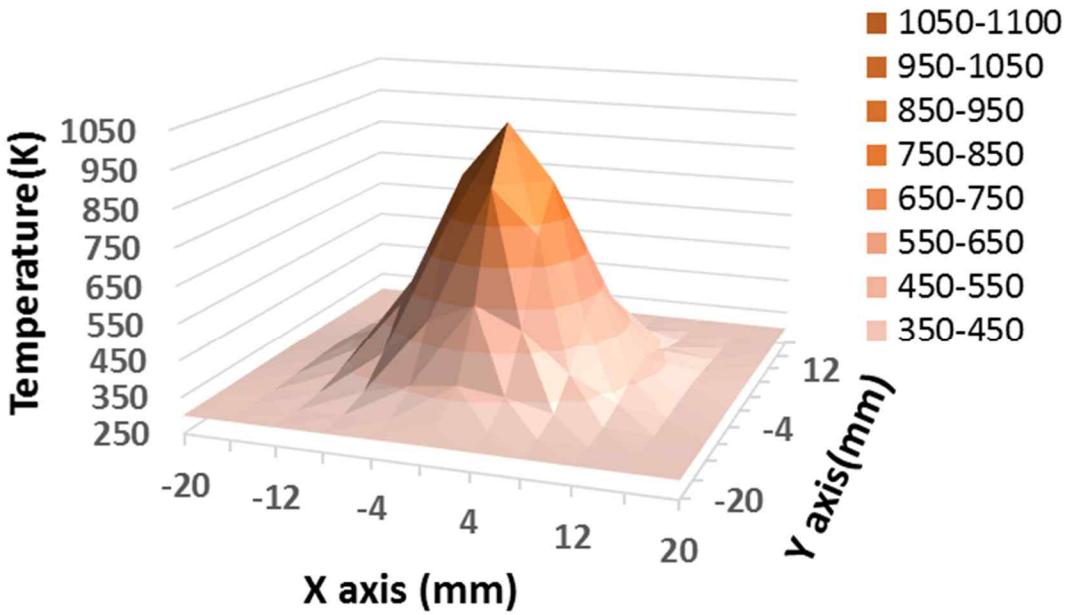

(a) 2D temperature distribution

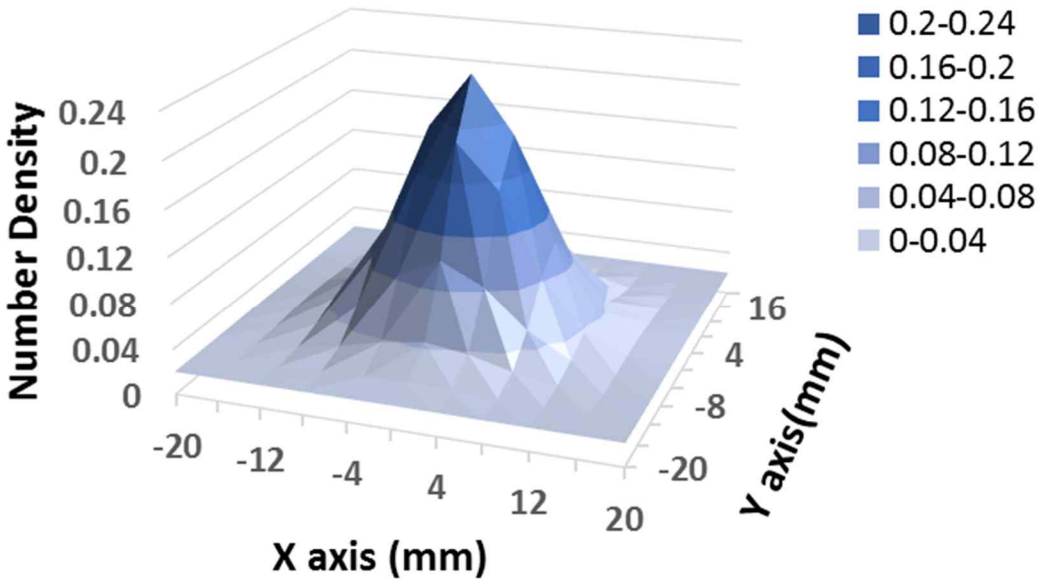

(b) 2D H_2O number density distribution

Fig. 4.19 Phantoms for 2D temperature and H_2O number density distributions

4.3.3 Simulation results

Fig. 4.20 (a), (b) show the result of reconstructed 2D temperature and number density distributions from the phantom data of Fig. 4.18. The temperature error in the center is only 4 K and maximum error is 54 K at region of boundary. The average temperature deviation and the relative error were a range of -54 ~ 45 K and 0.06 and the average H_2O number density deviation and the relative error were a range of -0.015 ~ 0.029 and 0.04. H_2O number density error is maximum at the center.

Fig. 4.21 (a), (b) show the result of reconstructed 2D temperature and H_2O number density distributions from the phantom data of Fig. 4.19. The temperature error in the center is only -5.8 K and maximum error is -69 K at region of boundary. The average temperature deviation and the relative error were a range of -69 ~ 52 K and 0.048. This result means the reconstruction performance is twice as good as that of J. Song et al [15]. The average H_2O number density deviation and the relative error were a range of -0.014 ~ 0.018 and 0.0327. Number density error is maximum 0.018 at the center.

The reconstructed 2D temperature and H_2O number density distributions are good agreement with the virtual data of Fig. 4.18 and Fig. 4.19.

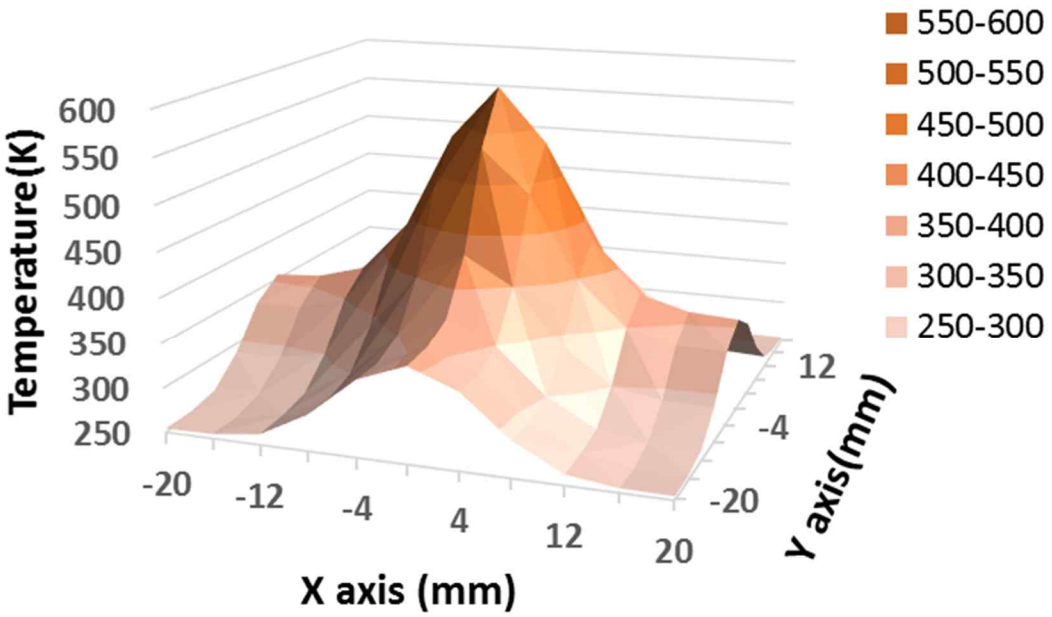

(a) 2D temperature distribution

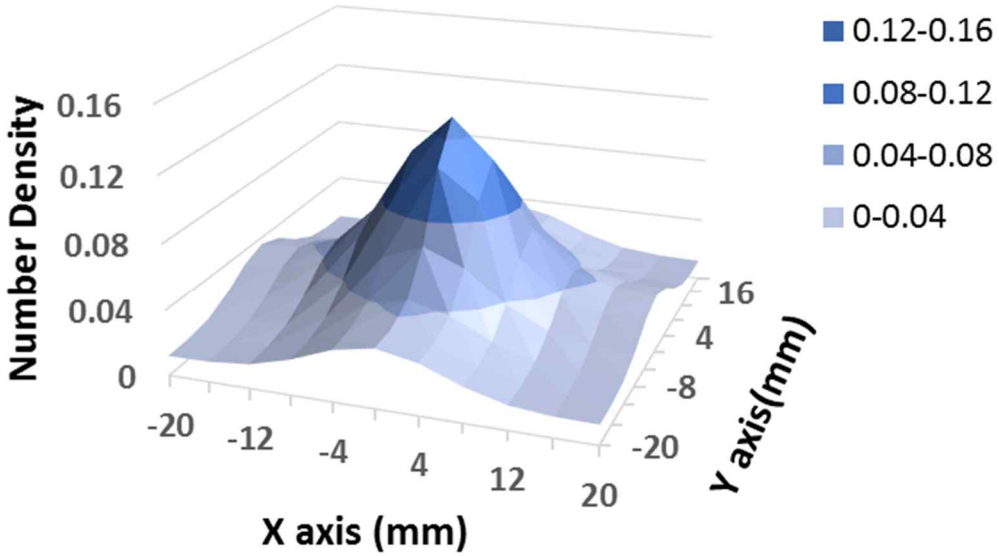

(b) 2D H_2O number density distribution

Fig. 4.20 The reconstructed 2D temperature and H_2O number density distributions

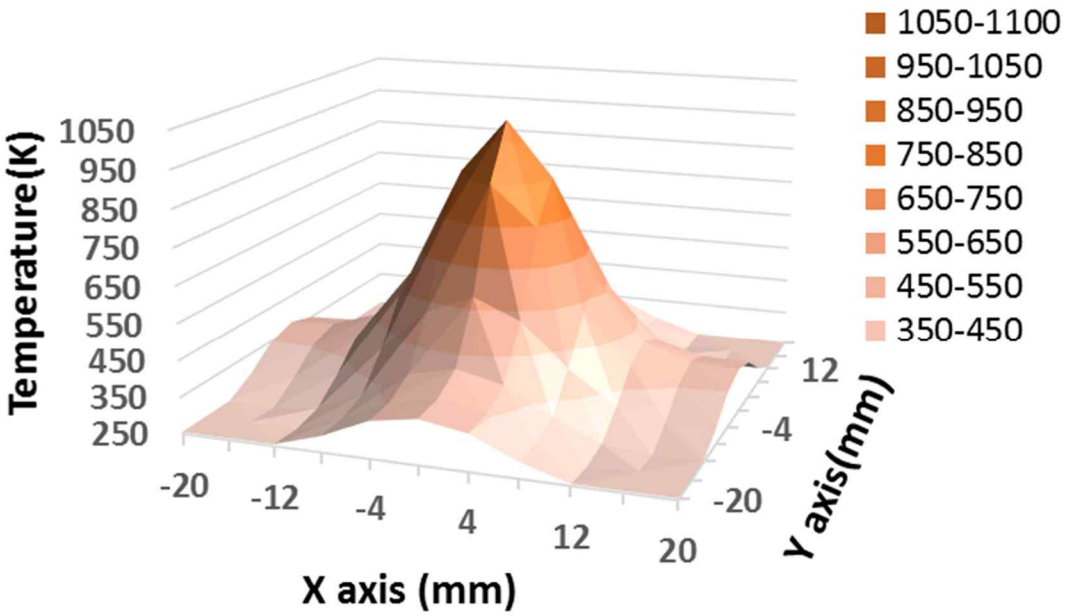

(a) 2D temperature distribution

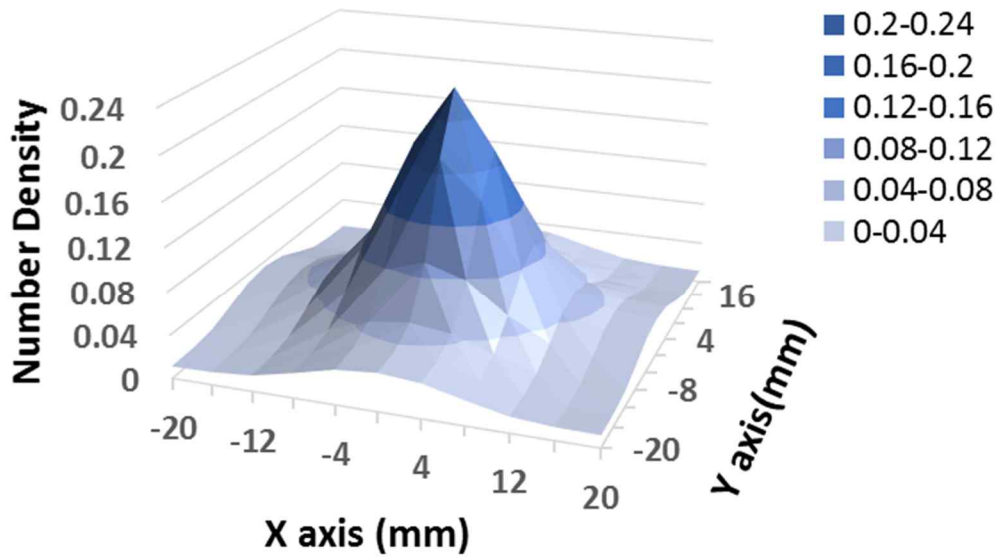

(b) 2D H_2O number density distribution

Fig. 4.21 The reconstructed 2D temperature and H_2O number density distributions

4.3.4 Experiment setup

Fig. 4.22 is an outline of the experimental apparatus and measurement cell and Fig. 4.23 is the actual pictures of the engine experiment system in this study.

A set of TDLAS system is equal to them of chapter 4.13. The data acquisition rate was 500 kHz (500 data points on every 1 scan of absorption spectra) and the temperature in the measurement region was measured by chromel-alumel thermocouples with a diameter of 100μm (KMT-100-100-120). With measuring the temperature, the absorption spectra were measured simultaneously by TDLAS system.

The experiment was performed by using OHC gasoline engine (FUJI HEAVY INDUSTRIES, Inc., EX13) as shown in Fig. 4.23. Laser paths were set at the outlet of the engine exhaust pipes. The diameter of 16 path measurement cells is 70 mm and the diameter of the engine exhaust pipe is 22 mm with thickness of 3.5 mm. The pipe length is 160 mm. The center of an exhaust outlet was set to match up with the center of measurement cells

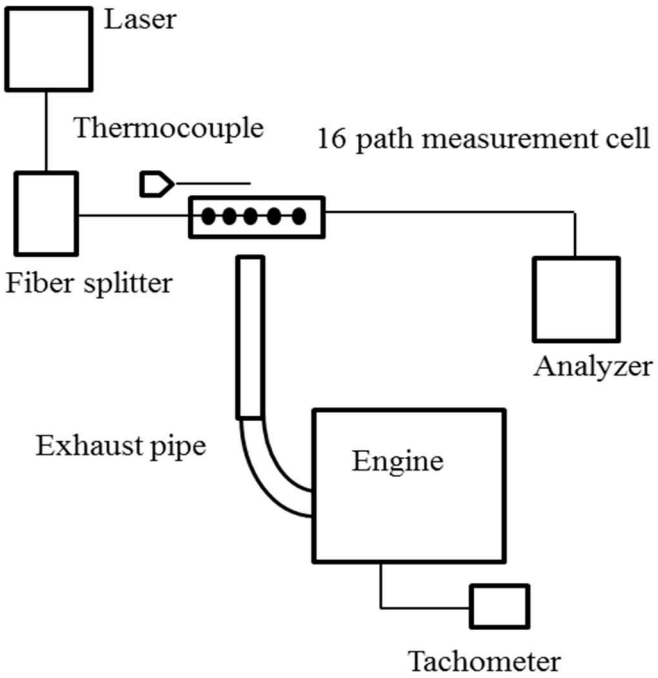

(a) Experimental apparatus

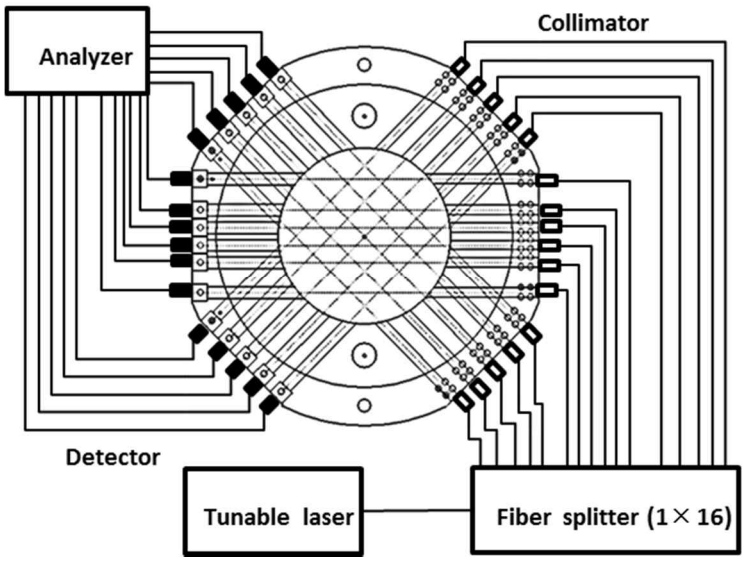

(b) 16 path measurement cell measurement system

Fig. 4.22 The outline of the experimental apparatus and measurement cell

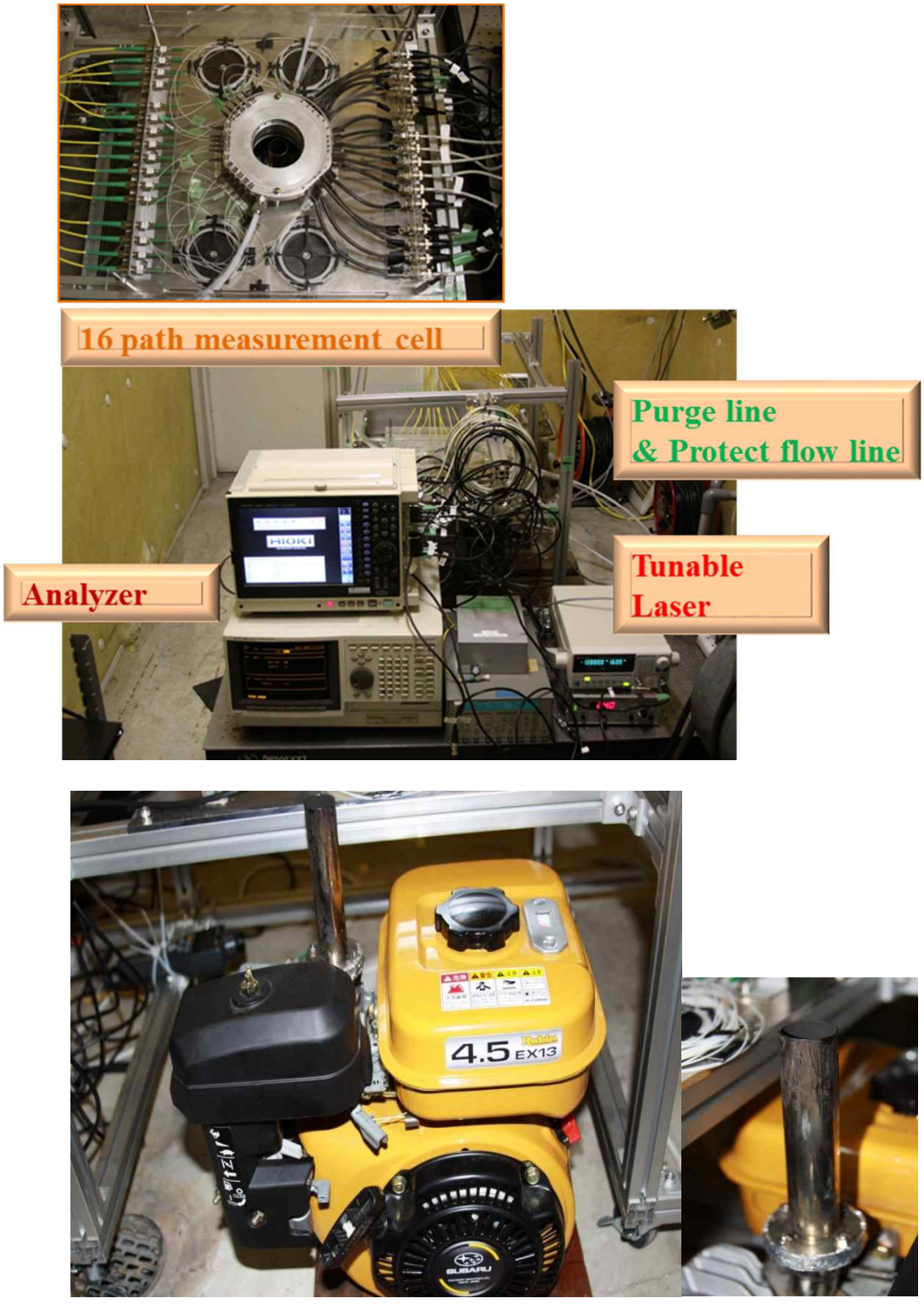

Fig. 4.23 Pictures of engine experiment system

4.3.5 Results of experiment and simulation

Fig. 4.24 shows the absorption graphs of H_2O spectra with 16 path lasers. Absorption graphs are stabilized by using averaged 500 absorption periods.

Fig. 4.25 shows the temperature history measured by thermocouple at X=0 mm, Y=0 mm point. Temperatures of exhaust gas and engine speed were continuously measured during 10 seconds. The measured temperature was about 500 K when engine speed reached to 2900 rpm at 9 seconds.

Fig. 4.26 shows the result of 2D temperature measurement at 9 seconds in engine exhausts using the only 10 paths of measurement cell because our algorithm did not considered lasers of the diagonal path. Nevertheless, 12 virtual lasers was added by using inverse distance interpolation method [15] for improving a spatial resolution. The reconstructed high temperature was 501.6 K at the center and was 353 K at the boundary region. Also, the reconstructed H_2O number density was 0.0358 at the center and was 0.0111 at the boundary region.

The result of 2D temperature measurement using CT-TDLAS showed good agreement with the thermocouple measurements. Also, the number density could be forecasted by using simultaneous fitting method of 6-Line-Profiles Fitting Algorithm. An excellent reconstruction performance of 6-Line-Profiles Fitting Algorithm was theoretically and experimentally demonstrated in virtual data and actual engine.

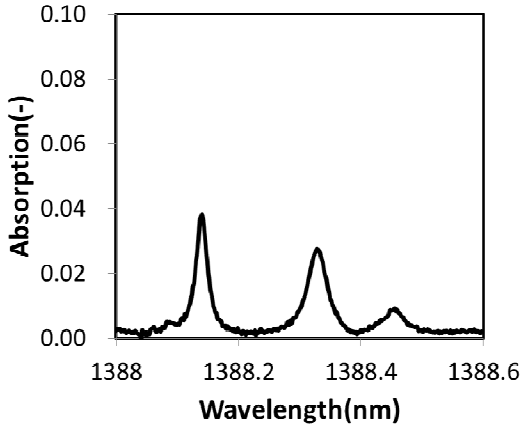

(a) Laser path 1

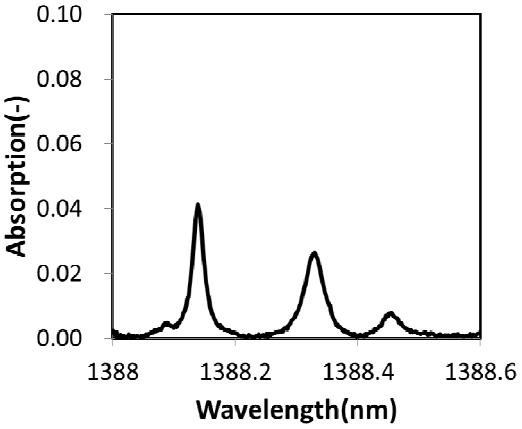

(b) Laser path 2

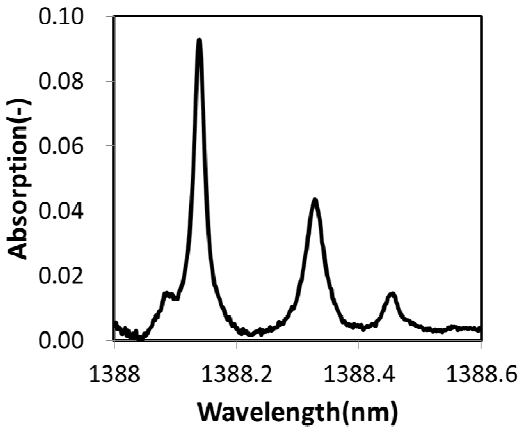

(c) Laser path 3

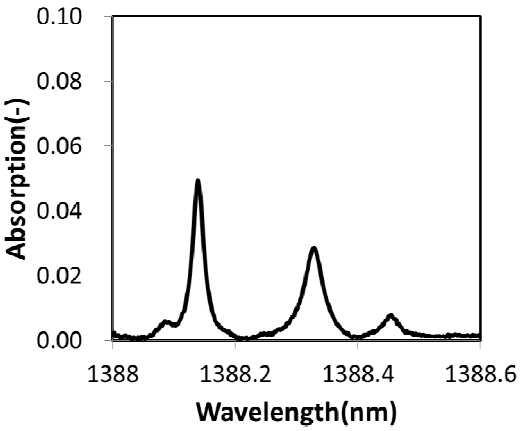

(d) Laser path 4

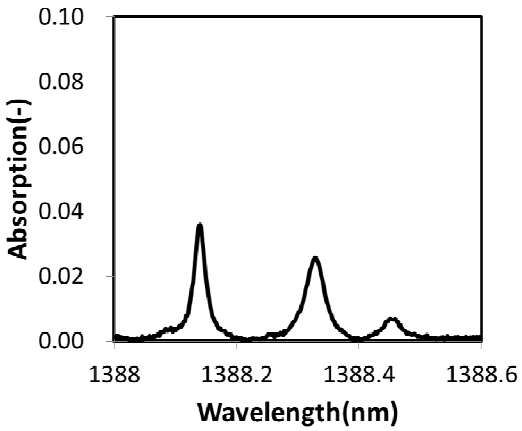

(e) Laser path 5

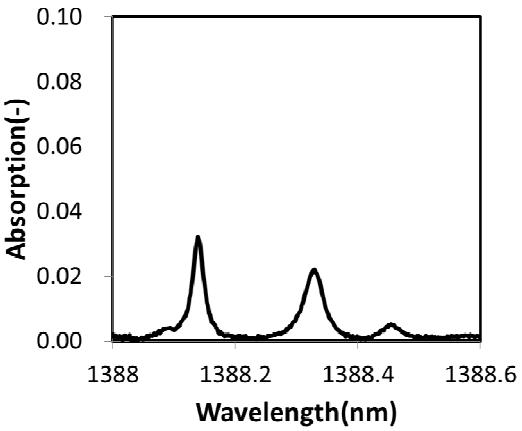

(f) Laser path 6

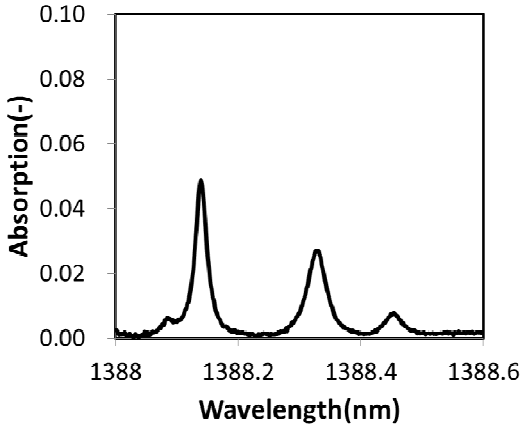

(g) Laser path 7

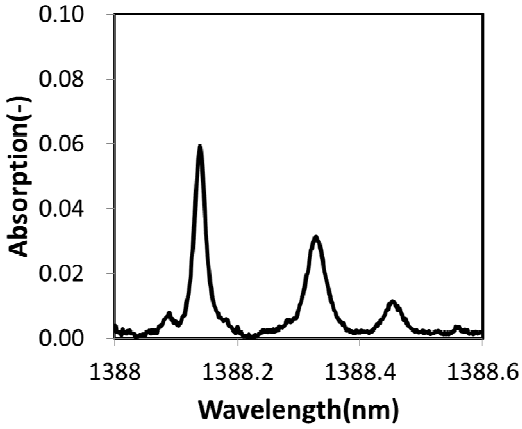

(h) Laser path 8

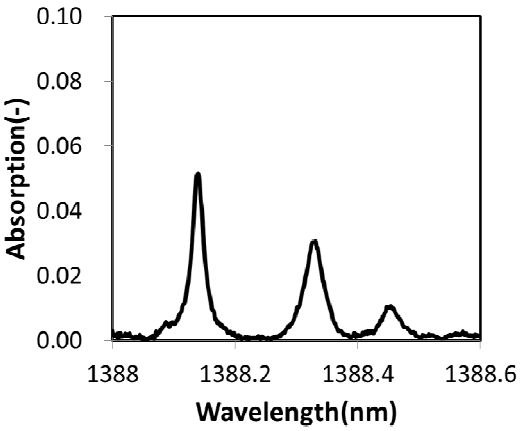

(i) Laser path 9

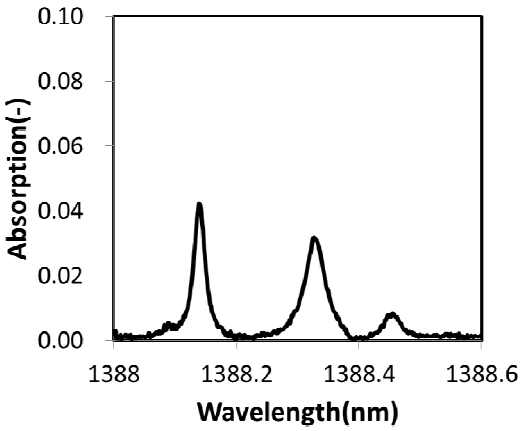

(j) Laser path 10

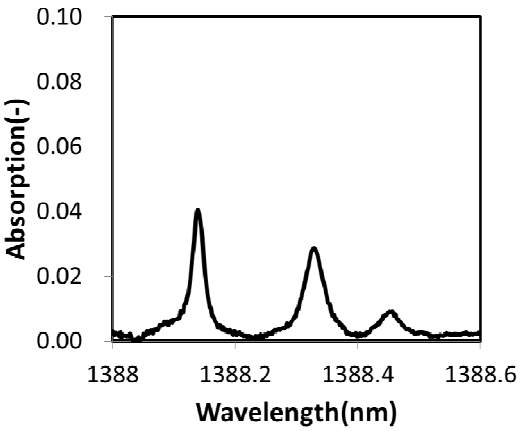

(k) Laser path 11

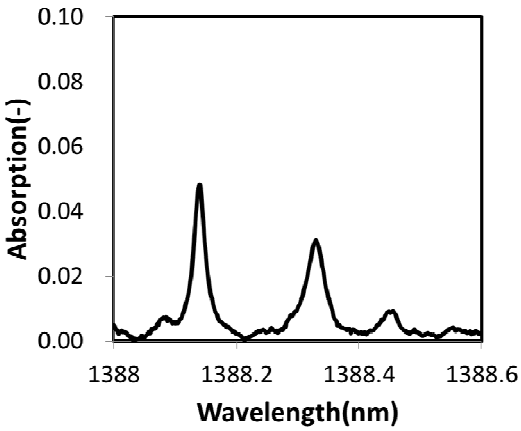

(l) Laser path 12

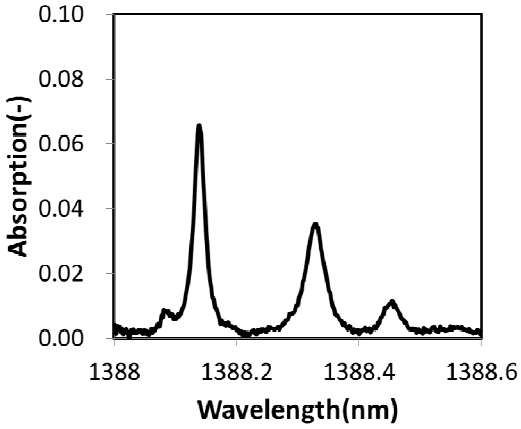

(m) Laser path 13

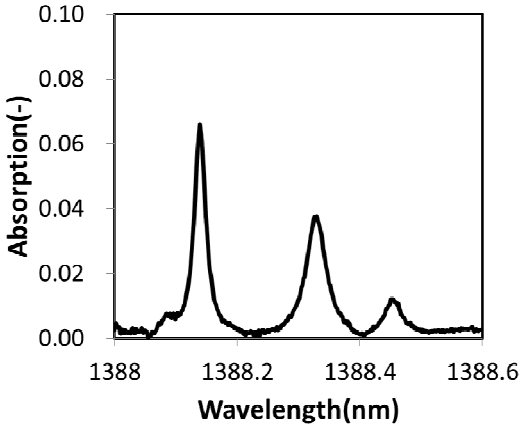

(n) Laser path 14

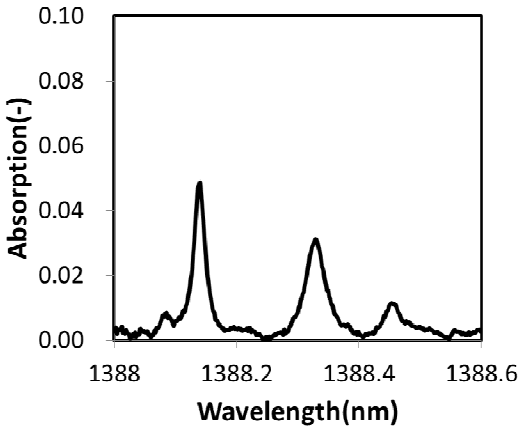

(o) Laser path 15

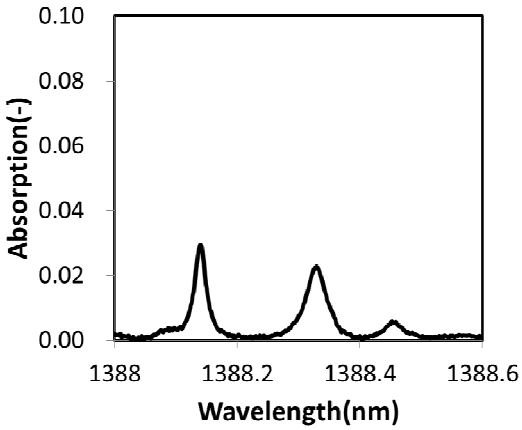

(p) Laser path 16

Fig. 4.24 Absorption graphs of H_2O spectra with 16 path lasers

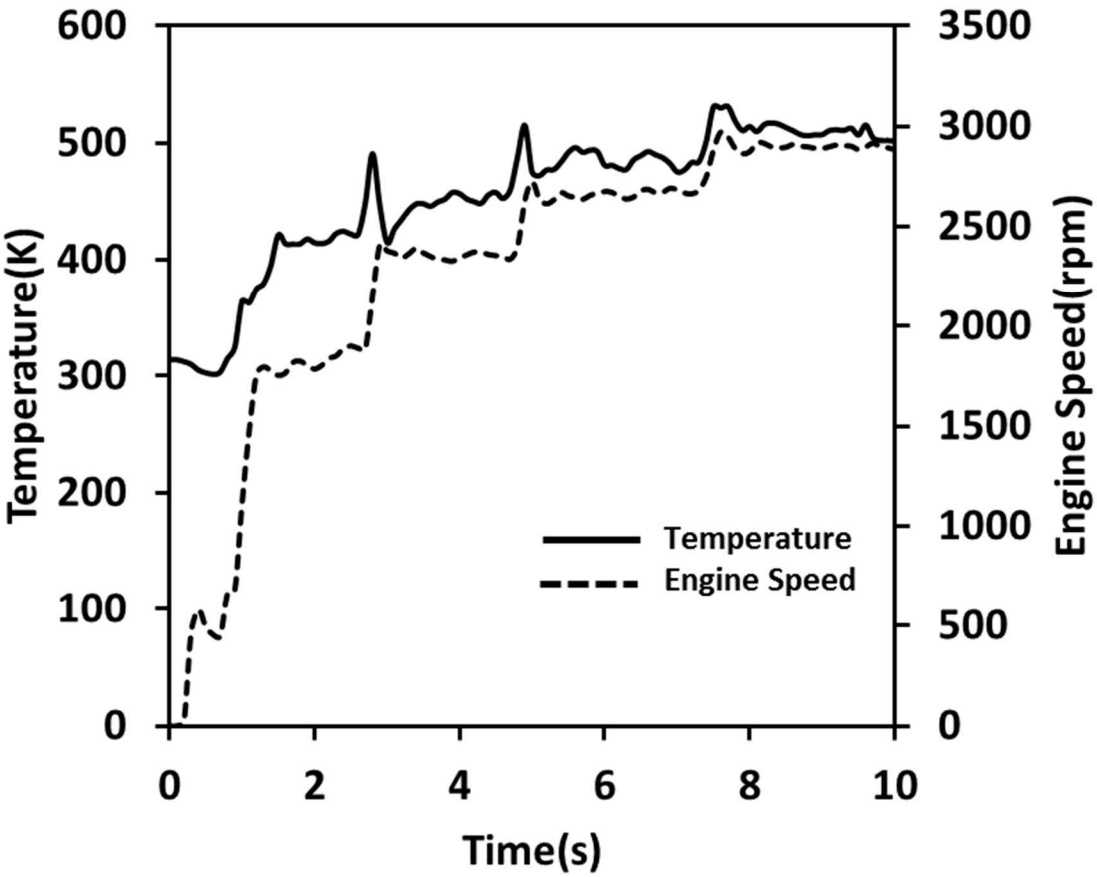

Fig. 4.25 Temperature history measured by thermocouple at the center (X=0 mm, Y=0 mm)

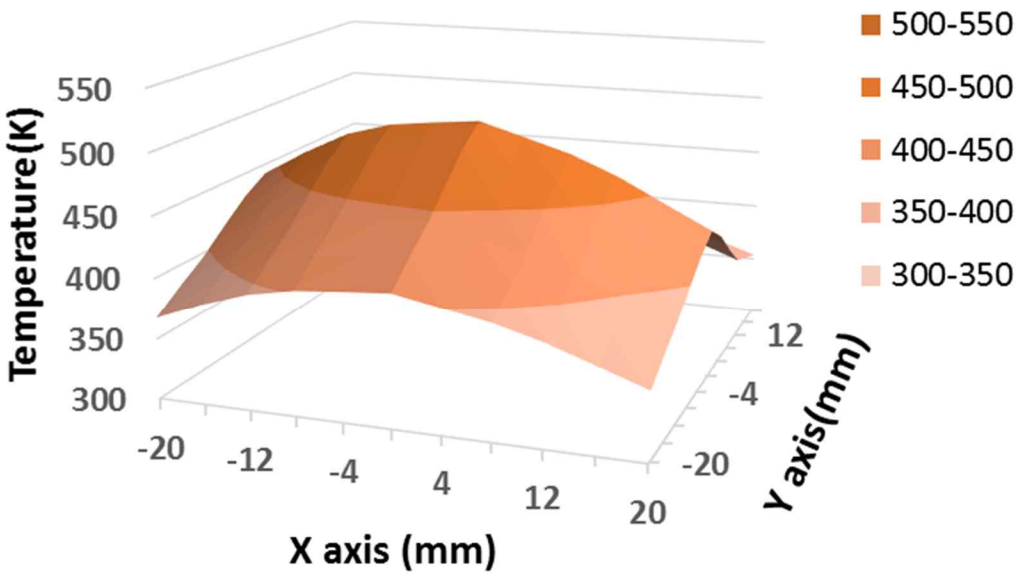

(a) The reconstructed 2D temperature distribution

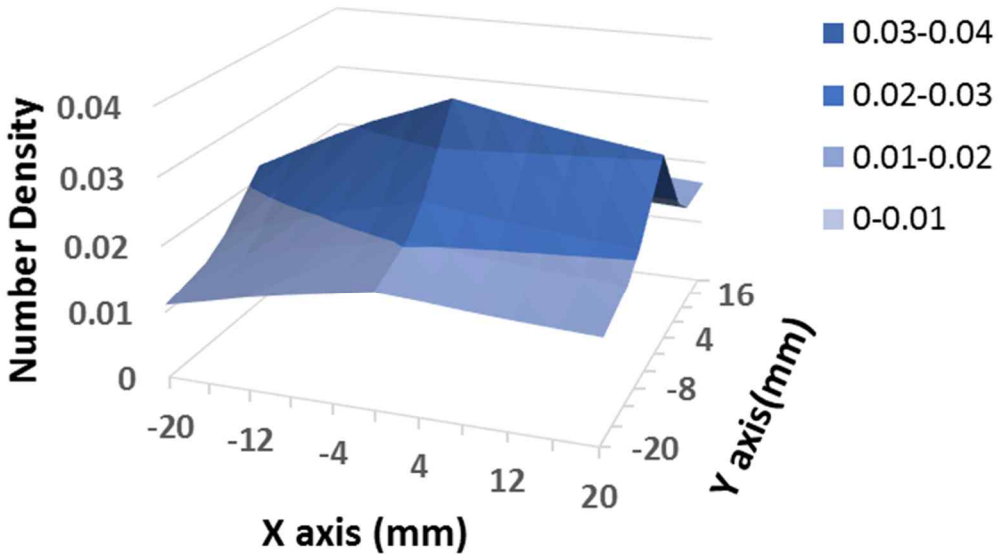

(b) The reconstructed 2D number density

Fig. 4.26 The result of 2D temperature and number density measurement in engine exhausts

5. Conclusion

To enhance a performance of CT-TDLAS system, MART algorithm has been adopted to iteration calculation, and an optimal parameter for the best relaxation coefficient of MART algorithm was 0.1. It was found that MART algorithm showed shorter calculation time than ART algorithm. It was chosen that MLOS (multiple line of sight) method was the most useful approach for finding initial values at the iterative calculation of CT-TDLAS.

Further, these three type algorithms for the enhancement of the result obtained by CT-TDLAS were developed and evaluated as follows.

Two-Ratios of Three-Wavelength Fitting (#1/#2, #1/#3) Algorithm showed better performance than Ratio of Two-Wavelength Fitting (#1/#2) Algorithm, revealing that additional information of the ratios of temperature improved calculation stability.

Full-Profile Cross-Correlation Algorithm was able to reduce the calculation time for convergence, usually unstable due to signal noises, bias error, and signal mismatches.

It was shown that Full-Profile Cross-Correlation Algorithm sometimes produced a longer calculation time if the calculated absorption curves were mismatched on data sets.

Finally, 6-Line-Profiles Fitting Algorithm was a very stable calculation and showed good agreement with the numerical data and experimental ones. Also, number density and temperature were possible to reconstruct simultaneously. This technique can be applied to the real time measurements of temperature and concentration. Further work need to develop an analysis by using a diagonal path and to apply to the gas of various species.

References

[1] C.B. Lim, W. Wang, S.S. Yang, K.K. Lee, Development of SAW-based Multi-gas Sensor for Simultaneous Detection of CO_2 and NO_2, Sensors and Actuators B: Chemical, Vol.154, No.1, pp.9-16, 2009.

[2] G.F. Fine, L.M. Cavanagh, A. Afonja, R. Binions, Metal Oxide Semi-Conductor Gas Sensors in Environmental Monitoring, Sensors, Vol.10, pp.5469-5502, 2010.

[3] S. Chen, Surface Micromachined Thermal Conductivity Gas Sensors for Hydrogen Detection, PhD. Dissertation, TU Delft, 2010.

[4] N. Dossi, R. Toniolo, A. Pizzariello, E. Carrilho, E. Piccin, S. Battiston, G. Bontempelli, An Electrochemical Gas Sensor based on Paper Supported Room Temperature Ionic Liquids, Lab on Chip, Vol.12, No.1, pp.153-158, 2012.

[5] Y. Yuki, A. Murata, Optimum Combustion Control by TDLS200 Tunable Diode Laser Gas Analyzer, Yokogawa Technical Report English Edition, Vol.53, No.1, pp.19-22, 2010.

[6] Y. Deguchi, Y. Daisuke, A. Akira, Development of 2D temperature and concentration measurement method using tunable diode laser absorption spectroscopy, Journal of Mechanics Engineering and Automation, Vol. 2, 2012, pp.543-549, 2012.

[7] T. Kamimoto, Y. Deguchi and Y. Kiyota, High temperature field application of two dimensional temperature measurement technology using CT tunable diode laser absorption spectroscopy, Journal of Flow Measurement and Instrumentation, , Vol. 46, pp.51-57, 2015.

[8] X. Liu, J.B. Jeffries, R.K. Hanson, K.M. Hinckley, M.A. Woodmansee, Development of a tunable diode laser sensor for measurement of gas turbine exhaust temperature,

Applied Physics B 82, pp. 469-478, 2006.

[9] Y. Deguchi, M. Noda, M. Abe, M. Abe, Improvement of combustion control through real-time measurement of O2 and CO concentrations in incinerators using diode laser absorption spectroscopy, in: Proceedings of the Combustion Institute, Vol. 29, pp. 147-153, 2002.

[10] M. Yamakage, K. Muta, Y. Deguchi, S. Fukada, T. Iwase, T. Yoshida, Development of direct and fast response exhaust gas measurement, SAE Paper 20081298, 2008

[11] Y. Zaatar, J. Bechara, A. Khoury, D. Zaouk, and J.-P. Charles, Diode laser sensor for process control and environmental monitoring, Applied Energy 65, pp.107-113 2000.

[12] X. Zhou, X. Liu, J. B. Jeffries, R. K. Hanson, "Development of a sensor for temperature and water concentration in combustion gases using a single tunable diode laser", Measurement Science and Technology, Vol. 14 No. 8, pp.1459-1468, 2003.

[13] P. Wright, N. Terzijaa, J. L. Davidsona, S. Garcia-Castillo, C. Garcia-Stewart, S. Pegrumb, S. Colbourneb, P. Turnerb, S. D. Crossleyc, T. Litt, S. Murrayc, K. B. Ozanyana, and H. McCanna, High-speed chemical species tomography in a multi-cylinder automotive engine, Journal of Chemical Engineering, 158(1), pp. 2-10, 2010.

[14] F. Wang, K. F. Cen, N. Li, J. B. Jeffries, Q. X. Huang, J. H. Yan, and Y. Chi, Two-dimensional tomography for gas concentration and temperature distributions based on tunable diode laser absorption spectroscopy, Meas. Sci. Technol. 21, 045301(10pp), 2010.

[15] J. Song, Y. Hong, G. Wang and H. Pan, Algebraic tomographic reconstruction of two dimensional gas temperature based on tunable diode laser absorption spectroscopy. Applied Physics B: Lasers and Optics, Vol.112, No.4, pp.529-537, 2013.

[16] F. Wang, Q. Wu, Q. Huang, J. Yan, and K. F. Cen, Simultaneous measurement of 2

dimensional H_2O concentration and temperature distribution in premixed methane/air flame using TDLAS-based tomography technology, Optics Communications, Vol.346, No.1, pp. 53-63, 2015.

[17] L. Ma and W. Cai, Numerical investigation of hyperspectral tomography for simultaneous temperature and concentration imaging, APPLIED OPTICS, Vol. 47 No 21, pp. 3751-3759, 2008.

[18] L. Ma, W. Cai, Determination of the optimal regularization parameters in hyperspectral tomography, Applied Optics, Vol. 47, No. 23, pp.4186-4192, 2008.

[19] L. Ma, X. Li, S.T. Sanders, A.W. Caswell, S. Roy, D.H. Plemmons and J.R. Gord, 50-kHz-rate 2D imaging of temperature and H2O concentration at the exhaust plane of a J85 engine using hyperspectral tomography. Optics Express, Vol.21, No.1, pp.1152-1162, 2013.

[20] W. Cai and C.F. Kaminski, Multiplexed absorption tomography with calibration-free wavelength modulation spectroscopy. Applied Physics Letters, Vol.104, No.15, pp. 154106, 2014.

[21] W. Cai and C.F. Kaminski, A tomographic technique for the simultaneous imaging of temperature, chemical species, and pressure in reactive flows using absorption spectroscopy with frequency-agile lasers. Applied Physics Letters, Vol.104, No.3, pp.034101, 2015.

[22] W. Cai and C.F. Kaminski, A numerical investigation of high resolution multispectral absorption tomography for flow thermometry, Applied Physics B, Vol.119, No.1, pp. 29-35, 2015.

[23] H. McCann, P. Wright and K. Daun, Chemical species tomography, Industrial Tomography: Systems and Applications, Inc. Elsevier, pp. 135-174, 2015.

[24] A. Seidel, S. Wagner, A. Dreizler and V. Ebert, Robust, spatially scanning, open-path TDLAS hygrometer using retro-reflective foils for fast tomographic 2D water vapor concentration field measurements. Atmospheric Measurement Techniques, Vol. 8, No.5, pp. 2061-2068, 2015.

[25] V.L. Kasyutich and P.A. Martin, Towards a two-dimensional concentration and temperature laser absorption tomography sensor system. Applied Physics B: Lasers and Optics, Vol.102, No.1, pp.149-162, 2011.

[26] Y. Deguchi, T. Kamimoto and Y. Kiyota, Time Resolved 2D Concentration and Temperature Measurement using CT Tunable Laser Absorption Spectroscopy. Flow Measurement and Instrumentation, In press. 2015.

[27] J. Shao, L. Wang and C. Ying, Numerical investigation of the two-dimensional gas temperature distribution based on tunable diode laser absorption spectroscopy. Optica Applicata, Vol.45, No.2, pp. 183-198, 2015.

[28] Y. Hong, J. Song, G. Wang and H. Pan, Optimal beam arrangement design for two dimensional temperature and concentration reconstruction using ASA and SQP algorithms. Optik, Vol.126, No.2, pp. 292-296, 2015.

[29] S. A. Tsekenis, N. Tait and H. McCann Spatially resolved and observer-free experimental quantification of spatial resolution in tomographic images. Review of Scientific Instruments, Vol.86, No.3, pp. 035104, 2015.

[30] T. Kamimoto, Y. Deguchi, D.W Choi, D. Yasui, J.H Shim, Accuracy Verification on 2D Temperature Measurement Method Using CT-tunable Diode Laser Absorption Spectroscopy, Transactions of Society of Automotive Engineers of Japan Vol.45, No.1, 2014.

[31] C. Liu, L. Xu, Z. Cao and H. McCann, Reconstruction of Axisymmetric Temperature

and Gas Concentration Distributions by Combining Fan-Beam TDLAS With Onion-Peeling Deconvolution. Transactions on Instrumentation and Measurement, Vol.63, No.12, pp. 3067-3075, 2014.

[32] X. An, T. Kraetschmer, K. Takami, S.T. Sanders, L. Ma, W. Cai, X. Li, S. Roy and J. R. Gord, Validation of temperature imaging by H2O absorption spectroscopy using hyperspectral tomography in controlled experiments. Applied Optics, Vol.50, No.40, pp. A29-A37, 2011.

[33] Y. Deguchi, Industrial applications of Laser Diagnostics, CRS Press, Taylor & Francis, 2011.

[34] L.S. Rothman, I.E. Gordon, A. Barbe, D. ChrisBenner, P.F. Bernath, M. Birk, V. Boudon, L.R. Brown, A. Campargue, J.-P. Champion, K. Chance, L.H.Coudert, V. Dana, V.M. Devi, S. Fally, J.-M. Flaud, R.R.Gamache, A. Goldman, D. Jacquemart, I. Kleiner, N. Lacome, W.J. Lafferty, J.-Y. Mandin, S.T. Massie, S.N. Mikhailenko, C.E. Miller, N. Moazzen-Ahmadi, O.V. Naumenko, A.V. Nikitin, J. Orphal, V.I. Perevalov, A. Perrin, A. Predoi-Cross, C.P. Rinsland, M. Rotger, M. Simeckova, M.A.H. Smith, K. Sung, S.A. Tashkun, J. Tennyson, R.A. Toth, A.C. Vandaele, and J. VanderAuwera, “The HITRAN2008 molecular spectroscopic database,” Journal of Quantitative Spectroscopy & Radiative Transfer - Elsevier, 110, pp. 533-572, 2009.

[35] R. R. Gamache, S. Kennedy, R. Hawkins, L. S. Rothman, Journal of Molecular Structure 517-518 pp. 407-425, 2000

[36] G.E. Elsinga, F. Scarano, B. Wieneke, and B. W. van Oudheusden. Tomographic particle image velocimetry, Experiments in Fluids, Vol. 41, pp. 933-947, 2006.

[37] D. H. Doh, G. R. Cho and Y. H. Kim, Development of a tomographic PTV, Journal of Mechanical Science and Technology, Vol. 26(12), pp.3811-3819, 2012.

[38] D. H. Doh, C. J. Lee, G. R. Cho, K. R. Moon, Performances of Volume-PTV and Tomo-PIV : Open Journal of Fluid Dynamics Vol.2 No.4A, pp. 368-374, 2012.

[39] E. E. Whiting, An Empirical Approximation to the Voigt Profile, Journal of Quantitative Spectroscopy and Radiative Transfer, Vol. 8, Issue 6, pp. 1379-1384, 1968